Università degli Studi di Padova

Centro Ricerche Fusione

Ghent University

JOINT RESEARCH DOCTORATE IN FUSION SCIENCE AND ENGINEERING

Cycle XXXV

Studies for improving the power supply system and the plasma performance in Reversed Field Pinch experiments

Coordinator: Prof. Gianmaria De Tommasi

Supervisor at Università degli Studi di Padova (Home University): Dr. Alberto Maistrello

Supervisor at Ghent University (Host University): Prof. Kristel Crombé

Ph.D. student: Francesco Lunardon

Padova, January 2023

Table of contents

Summary

The context of my Ph.D. thesis studies is related to electric power handling in existing and future large-sized magnetic fusion experiments, which is essential to obtain an efficient operation of these machines and fully exploit their potential.

Such studies for existing experiments are intended to satisfy the evolution of the requirements coming from physics, aimed at improving plasma performances. This is the case of RFX-mod experiment. RFX-mod is an experimental fusion device that contributes to plasma physics studies in Reversed Field Pinch (RFP) and tokamak configurations. Its high flexibility, due to an active magnetohydrodynamic (MHD) control system and the modular Coils Power Supply (CPS) system, allowed operating RFX-mod in a wide range of experimental conditions with a plasma current up to 2 MA. Experiments with such high plasma current allowed the study of new promising confinement regimes, dominated by a self-organization process with the generation of a helical structure in the plasma core. Presently RFX-mod is under a significant upgrade (RFX-mod2) to extend the operational scenarios increasing the proximity between the conductive shell and the plasma. This main modification of the magnetic front-end, together with other main improvements, is expected to increase the machine performance in both magnetic configurations.

A further step in perspective could be an increase of the plasma current; in fact, the study of RFP physics at higher plasma current could be crucial to confirm positive trends, like electron temperature and persistence of Quasi Single Helicity (QSH) states with the plasma current, to explore the new advanced confinement scenarios and to fully exploit and raise the new potential of the RFP configuration.

In this framework, my thesis includes the studies and the experimental activities aimed at improving the performance of the RFX-mod2 power supply system with the aim to increase the maximum achievable plasma current and the flat-top duration. A solution based on additional magnetic energy storage has been studied during the first year of my PhD course. With this new operational concept, during the charging phase, the magnetizing winding is charged along with an additional inductor, which acts as an energy storage reservoir. The stored energy, in the order of 100 MJ, is transferred to the magnetizing winding, and thus to the plasma, via transfer resistors in the last phase of the plasma current ramp-up, to increase the plasma current from the previous maximum value of 2 MA up to 2.6 MA. During the second year of my PhD, I studied an alternative reconfiguration of the poloidal power supply system based on a combined resistor-capacitor energy transfer system. This system allows to store energy in capacitor banks during the first phase of the plasma current ramp-up and releases it to the plasma when the magnetizing current changes polarity, driving the plasma current over 2.5 MA. Both solutions rely on a limited upgrade of the RFX power supply system, without overstressing the poloidal windings or overcoming the power limits of the main step-down transformers and maintaining the present set of thyristor converters units with a new configuration. The analyses regarding these two solutions are reported in section 2.

In future large-size fusion experiments, electrical power handling is expected to become a crucial issue. In fact, a large fraction of the electric power necessary for gas breakdown and plasma current rise requires active power peaks which increase with the machines size and plasma current value. Hence the need, for future large-sized experiments, to investigate innovative Power Supply (PS) systems, based on a combination of adequate energy storage and advanced converter topologies. These studies aim to mitigate the peaks of active power and to reduce the amount of reactive power exchanged with the grid, related to the use of thyristor converters, adopted in almost all fusion experiments.

Among the energy storage technologies, Superconducting Magnetic Energy Storage (SMES) is particularly suitable for large fusion devices, because of its large power density and adequate release time for these applications. Moreover, large fusion devices are provided with SuperConducting (SC) magnets, thus the plant is already equipped with the necessary auxiliaries. In this regard, I contributed to the development of a new concept, a new Magnetic Energy Storage and Transfer (MEST) system, based on SMES technology, as a very promising alternative to face both issues related to high active power peaks and huge reactive power demand. The application of the MEST system to supply the SC coils results in a partial or total degree of decoupling between the grid and the magnets coupled with the plasma, which means that the grid does not have to instantly provide the power delivered to the SC coil and the plasma, thus flattening the active power profile to be required from the grid and substantially nullifying the reactive power absorbed. As the MEST is a fully new scheme, R&D with industry involvement has to prove the feasibility first, and subsequently, the suitability and convenience of its application to a large reactor.

A great part of my PhD studies focuses on MEST development and application studies to PILOT, a neutron source based on RFP configuration for fusion-fission hybrid reactors, and to EU DEMO, a future tokamak which is being developed to study the commercial exploitation of fusion energy. During the third year of my PhD, I also contributed to the writing of technical specifications for a MEST small-scale prototype, to the follow-up of the procurement and I made dedicated analyses to confirm the design choices. A key part of my studies was the development of a dedicated control system to operate this system controlling efficiently all the different involved variables supplying the needed current on the load coil. The studies that I have conducted so far on the MEST system are reported in section 3.

During my PhD, I have also performed experimental activities aimed at revamping the Pulse Discharge Cleaning (PDC) system. In RFX-mod2 the PDC system will be utilized to obtain the First Wall (FW) conditioning, necessary to reach high-performance plasma discharges. The PDC was originally realized in the 80s, but never operated in RFX-mod because the FW conditioning was done thanks to a baking system that induces a current in the vessel heating up the FW at the desired temperature. In RFX-mod2 the highly resistive Inconel vessel will be removed, graphite tiles will be attached to the copper stabilizing shell and the support structure will be modified in order to be vacuum-tight. With the absence of the vacuum vessel, the baking system can’t be used and the PDC will be the only system that can do the FW conditioning.

Finally, during my four-month internship at ITER organization, I developed numerical models to be applied in Hardware In the Loop (HIL) real-time simulations. This type of simulation can be used to test the control system of complex power supply systems. The machine that runs the real-time models exchanges signals with the control system to be tested and this allows it to reproduce different normal and abnormal conditions that the control system has to deal with during its operation. This type of simulation can be used to test and develop the MEST small-scale prototype and future advanced converters control systems.

1 Introduction

1.1 World energy consumption

The main causes of the rising demand for energy are population growth and increases in income per person. The world's population is expected to grow by 1.6 billion people by 2035, bringing the total to 8.7 billion. Over the same period, Gross Domestic Product (GDP) is expected to more than double and power generation is expected to account for an ever-increasing share of primary energy consumption as the world continues on a long-term trend of electrification: the share rises from about 42% today to 47% by 2035 [1].

As can be seen in Figure 1, total Greenhouse Gases (GHG) were equal to 49.4 Gt CO_2e in 2016, with carbon emissions from energy use being the largest source of GHGs, accounting for around 65% of all GHGs [2].

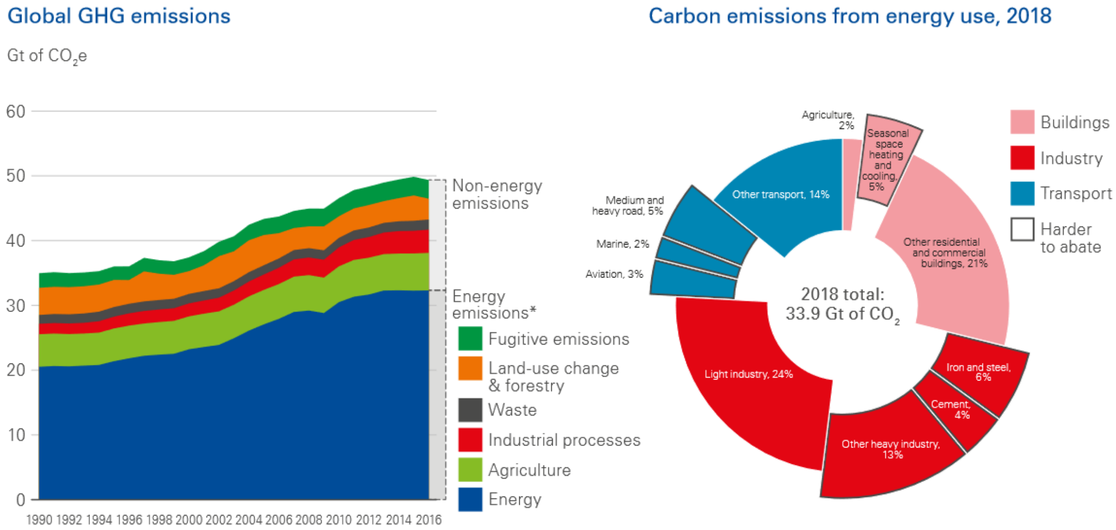

Global GHG emissions

Carbon emissions from energy use, 2018

Source: WRI estimates

**Energy Outlook* definition which includes CO_2 emissions from the combustion of fossil fuels.
Non-CO_2 emissions from energy as defined by WRI are allocated to Industrial processes and Fugitive emissions

Figure 1 – Global GHG emission and CO_2 emission from energy use [2]

Scientific evidence suggests that the dominant cause of climate change (Figure 2) is the release of GHGs and a transition to electricity generation from low-carbon sources is crucial in conjunction with efficiency improvements to reach an emissions peak quickly and then drastically reduce GHG emissions in the years to come.

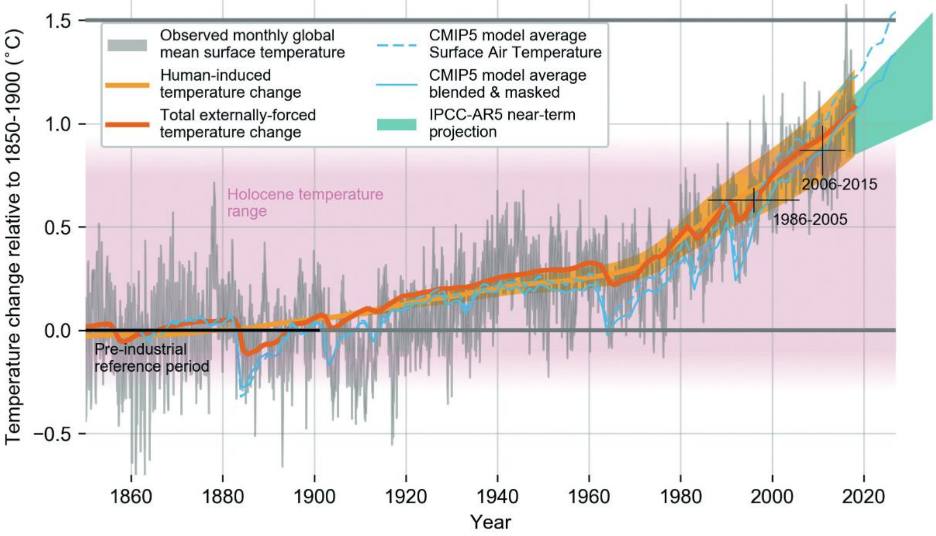

Figure 2 - Evolution of global mean surface temperature over the period of instrumental observations. [3]

The IPCC (Intergovernmental Panel on Climate Change) provided a Special Report in 2018 [3] on the impacts of global warming of 1.5°C above pre-industrial levels and related global greenhouse gas emission pathways that would achieve an increase of the global average temperature below 1.5-2°C. The Special Report confirms that climate change has already affected people and ecosystems worldwide and that limiting warming to 1.5 °C would require unprecedented transitions in all aspects of society. As can be seen in Figure 3, by adopting pathways compatible with no or limited overshoot of 1.5 °C, global anthropogenic CO_2 emissions decline by about 45% from 2010 levels by 2030 reaching net zero around 2050.

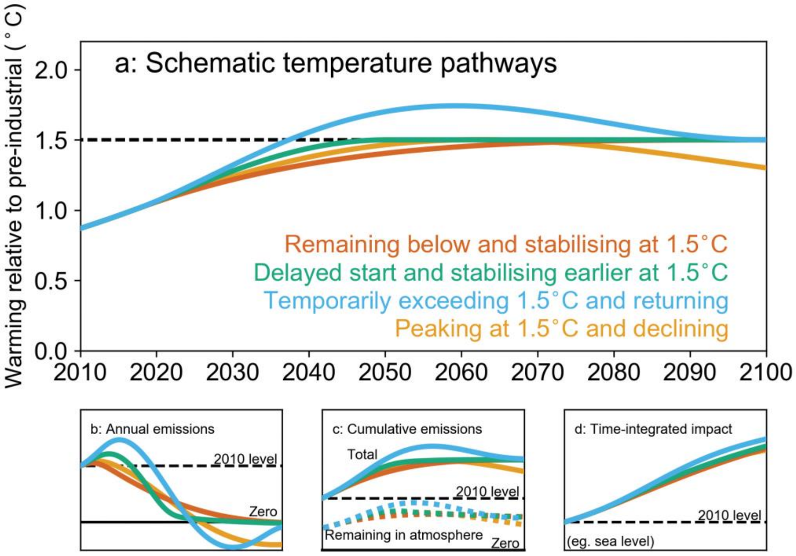

Figure 3 – Different 1.5 °C pathways: schematic illustration of the relationship between (a) global mean surface temperature (b) annual $C0_2$ emissions; (c) total cumulative CO_2 emissions (solid lines) and the fraction thereof remaining in the atmosphere (dashed lines); (d)a time-integrated impact, such as sea level rise, that continues to increase even after the global mean surface temperature has been stabilized. [3]

Such a great and fast reduction of CO_2 emissions involves an unprecedented rapid transition in energy, land, urban and infrastructure (including transport and buildings), and industrial systems. In pathways that limit global warming to 2°C, anthropogenic CO_2 emissions are projected to decline by about 20% by 2030 and reach zero around 2075 (Sustainable Development Scenario). Under business-as-usual assumptions, the average temperature increase is estimated at 4°C by the end of the century and 5.5°C in the long term. According to IPCC reports, with emissions in line with current pledges (i.e. Paris Agreement) global warming is expected to surpass 1.5 °C above the pre-industrial level, at least for a limited period of time even if these pledges increase in terms of mitigation of CO_2 emissions after 2030 [3].

Energy efficiency and technologies that support lower energy demand, for given energy services, usually are based on more mature technology and lower the trade-offs with respect to sustainable development. In addition, to meet the primary energy demand in the short-term renewables, conventional technology based on fossil fuels linked to Carbon Capture and Storage (CCS) technology and nuclear fission will be the leading technologies. In the next years, it will be crucial to assess their inherent limitations, namely temporal intermittency of the renewables, intermediate and high-level nuclear waste, meltdown and proliferation from fission and the lack of a viable market for CCS.

Even if the aforementioned technologies will lead to total decarbonization of electricity generation, nuclear fusion will still be a highly desirable low-carbon energy source. In this context, nuclear fusion could very well become a major player, having as its final aim an electricity-producing reactor: it could serve as a carbon-free baseload system to cover dark and wind still periods in a system dominated by intermittent energy from wind and the Sun. It has a clear advantage over fission in terms of nuclear waste production and no risk of proliferation. Nuclear fusion might be a direct competitor to natural gas power plants with CCS in a decarbonized energy market, having the advantage of much larger fuel availability, supporting the argument of energy security.

1.2 Nuclear fusion

Nuclear fusion is a nuclear process in which two or more atomic nuclei merge to form a heavier element. Energy is released as a result of the mass difference (mass defect) between the reactants and the products. The difference in the nuclei's binding energies before and after the reaction is what causes this mass defect. Two positively charged nuclei must overcome their mutual Coulomb repulsion in order to initiate a fusion process. In the sun, the proton-proton fusion chain process is possible due to the high core density, sustained by the gravitational force. This is not feasible on earth, since densities in this range cannot be attained. The most feasible reaction for using fusion processes on Earth involves the interaction between the hydrogen isotopes deuterium and tritium. They are used because of their bigger fusion cross-section compared to other possible reactions. The reactions that have a sufficiently high rate to compensate for the limited fuel density typical of magnetic confinement devices are:

$$^{2}D + \ ^{3}T \rightarrow He + \ ^{1}n + 17.6\ MeV \qquad \text{Eq. 1}$$

$$^{2}D + \ ^{2}D \rightarrow \ ^{3}He + \ ^{1}n + 3.27\ MeV \qquad \text{Eq. 2}$$

$$^{2}D + \ ^{2}D \rightarrow \ ^{3}T + \ ^{1}H + 4.03\ MeV \qquad \text{Eq. 3}$$

$$^{2}D + \ ^{3}He \rightarrow \ ^{4}He + \ ^{1}H + 18.3\ MeV \qquad \text{Eq. 4}$$

In accordance with the momentum conservation principle, the energy is released as kinetic energy from the reaction's products and distributed among these particles according to the inverse of their masses.

The probability of a fusion reaction to occur, given an area of interaction between the reactants, is defined as nuclear cross-section. Figure 4 reports the cross-sections of the previously reported reactions as a function of the relative velocity of the two reactant nuclei.

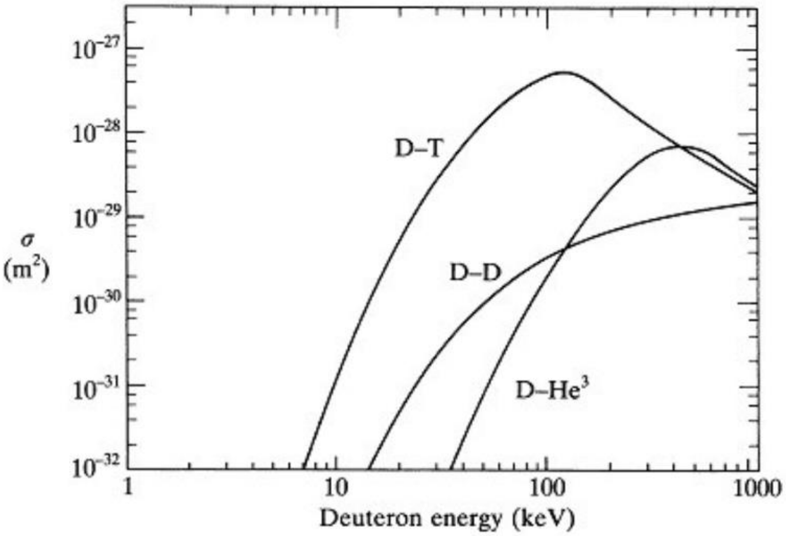

Figure 4 – Cross-sections for reactions D-T, D-D and D-^{3}He. The D-D curve represents the sum of the cross-sections of the two D-D reactions [5]

Due to technological limits, confinement of a large volume of plasma for a sufficiently long time is only possible at temperatures below 100 keV. In such conditions, the deuterium-tritium mixture is the most reactive fuel, with the highest cross-section at the lowest temperature. The mean temperature required to have a relevant number of reactions in a fusion reactor is 10 keV, despite the D-T curve having a maximum around particle energy of 100 keV. At this temperature, there are enough energetic ions populating the high-energy tail of the particle velocity distribution which can reach fusion. Current research is thus focusing on the D-T reaction.

A positive energy balance is possible if fuel particles can be made to react before they lose their energy. To achieve this the particles must retain their energy and remain in the reacting region for a sufficient time. More precisely the product of this time and the density of reacting particles must be sufficiently large. The most promising method of supplying the energy is to heat the deuterium-tritium fuel to a sufficiently high temperature that the thermal velocity of the nuclei is high enough to produce the required reactions. Fusion brought about in this way is called thermonuclear fusion.

Ignition means a self-sustaining burning plasma heated without any external system, but just with the energy coming from fusion reactions. The Lawson criteria express the condition needed to achieve ignition: temperature (T), density (n) and energy confinement time (τ_E) have to satisfy the relation expressed in Eq. 5.

$$nT\tau_E > 3 \cdot 10^{21} \frac{keVs}{m^3} \qquad \text{Eq. 5}$$

Figure 5 shows the ignition curve, as a function of the triple product parameters.

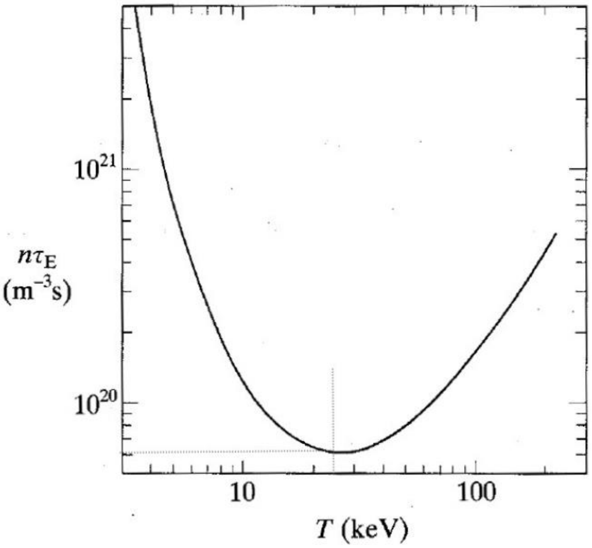

Figure 5 – The value of $n\tau_E$ require to obtain ignition as a function of the temperature T

The primary challenge of nuclear fusion is to confine the heated plasma (an ionized gas of Deuterium and Tritium) to sustain fusion reactions. There are two ways to confine the plasma, considering that no materials are able to withstand these temperatures:

- Inertial confinement: the plasma is produced by the implosion of a small amount of fuel (frozen Deuterium and Tritium), triggered by a powerful and well-focused set of laser beams. The fuel remains compressed thanks to their inertia for a short period of time (in the order of ns) before exploding, sufficient to produce a certain number of fusion reactions.

- Magnetic confinement: the plasma is confined by magnetic fields which kept the plasma away from the walls of the reactor vacuum vessel. This confinement is possible due to the fact that the plasma is an ionized gas (i.e. made by charged particles) and then it interacts with externally generated magnetic fields.

This PhD work focuses on technological aspects of magnetic confinement fusion devices, in particular related to the Reversed Field Pinch (RFP) and Tokamak configuration.

1.3 Tokamak and RFP working principle and magnet system

To reach the extremely high temperatures needed to have a significant cross-section for the fusion reactions the plasma has to be confined at a certain distance from the walls, to avoid both the wall being damaged and the plasma being cooled down. Being the plasma a fully ionized gas, its charged particles in a strong magnetic field are bound to the magnetic field lines as a result of the Lorenz force. The principle of magnetic confinement nuclear fusion is to use strong magnetic fields to confine the hot plasma in a certain region of space with a desired position and shape to generate thermonuclear reactions.

The straight cylinder magnetic field geometry is the most basic magnetic field geometry for plasma confinement. The issue with this shape is that plasma particles can escape from both ends. This escape may be significantly decreased by creating two "magnetic mirrors," which essentially entails boosting the field intensity at both ends with extra magnetic coils. However, because of the end loss-induced instabilities, proper confinement was never possible in such devices [4]. The obvious solution to prevent end losses is to have a configuration with a toroidal shape. The necessary toroidal magnetic field is generated by coils wound around the toroidal vacuum chamber, called toroidal field coils. However, having a toroidal geometry would make the problem of confinement hard to deal with, because such a system of coils generates a magnetic field that is stronger near the machine’s vertical symmetry axis. Such asymmetry would cause the charged particles to drift across the field lines, eventually leading to plasma losses. A possible solution would be not only to bend the magnetic field line into a torus but also to twist them around in a helical shape thanks to the contribution of a poloidal magnetic field which combines with the toroidal one [5].

From the beginning of fusion research, three alternative schemes have been studied: the tokamak, the Reversed Field Pinch (RFP) and the stellarator configurations.

In the tokamak configuration (Figure 6), the principal magnetic field is the toroidal field. To reach the plasma confinement also a poloidal field is necessary, as said before. In a tokamak, these fields are produced by toroidal field coils and plasma current that flows in the toroidal direction. The plasma current is induced inductively, like in a transformer, by the magnetic flux variation in the Central Solenoid (CS), also called inner poloidal field coils. This induces a voltage in the toroidal direction inside the vacuum vessel, called loop voltage, which drives the current in the plasma. Since the plasma has electrical resistance, the plasma current dissipates the ohmic power that heats the plasma itself. The average loop voltages are of the order of one volt for a large device with electron temperatures of several keV, with plasma currents up to several megaamperes and ohmic powers in the megawatt range [4].

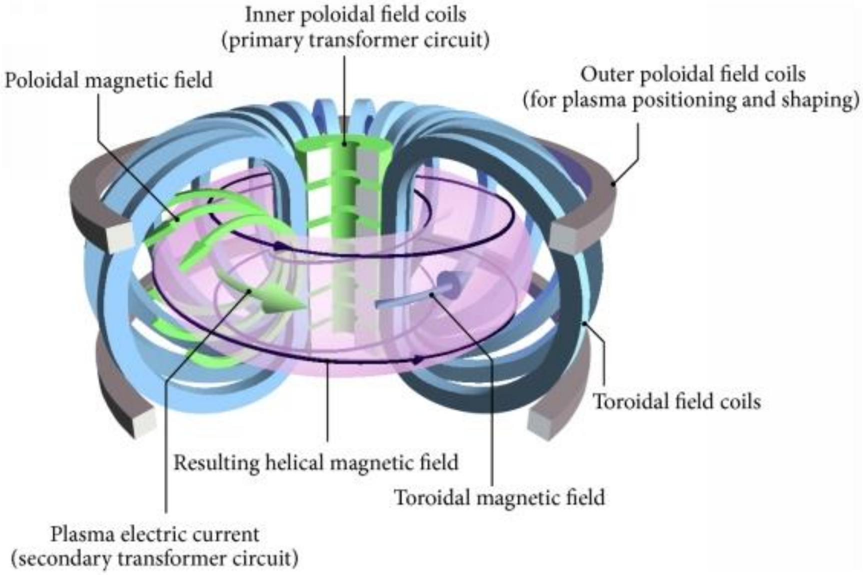

Figure 6 – Schematic representation of a tokamak

Outer poloidal field coils are also necessary for the vertical magnetic field to counteract the radial expansion forces and control the plasma shape. These coils are usually called Poloidal Field (PF) coils.

The operation of a tokamak is intrinsically pulsed because the loop voltage must maintain the same sign to have a constant plasma current, so the CS current must constantly vary in the same direction from the maximum CS current to the same value of the opposite sign; then the discharge must be terminated, and the primary circuit of the transformer recharged for the next pulse. Furthermore, the pure tokamak scheme of operation alone cannot reach high temperatures to generate a sufficient amount of fusion power. The more the plasma is heated using the intrinsic ohmic heating by the plasma current, the lower plasma electrical resistance and hence the ohmic-heating power. It decreases proportionally with $T^{-3/2}$, where T is the plasma temperature. Therefore, the nuclear fusion in a tokamak relies on auxiliary heating such as Neutral Beam Injection (NBI) or radio frequency heating systems.

Several tokamaks have been built. The biggest tokamaks presently in operation are the Joint European Torus (JET) in the UK, EAST in China, KSTAR in the Republic of Korea and, in the next few years, the upgraded Japanese tokamak JT-60SA. The next main step in controlled thermonuclear fusion research will be ITER experiment, which is under construction in France and will be the largest tokamak when it will start its operation in the second half of the 2020s. ITER aims to demonstrate some crucial aspects of the technological feasibility of fusion energy. The industrial and commercial exploitation of fusion energy will be investigated through a few DEMO experiments, which are now under conceptual design within some of the ITER members (including Europe, China and the Republic of Korea) and should be operating by the second half of this century. All of the large fusion devices built since the late 1980s are equipped with superconducting magnets. This includes also all that projects under construction that will also rely on superconducting magnets to carry higher currents and produce stronger magnetic fields than conventional resistive counterparts, while consuming less power.

The RFP configuration is an axisymmetric equilibrium that belongs to the toroidal pinch class, like the tokamak one. Also in the RFP, the plasma is confined by a combination of a poloidal magnetic field due to a toroidal current flowing in the plasma and a toroidal magnetic field generated by external coils. The main difference between these two toroidal pinches lies in the magnetic topology. In the RFP the toroidal and poloidal magnetic fields are both of the same magnitudes, in contrast with the tokamak where a stabilizing toroidal magnetic field larger than the poloidal one is needed, and the toroidal field reverses on the outside of the plasma (Figure 7) [6]. The poloidal current that generates the toroidal magnetic field is mostly in the plasma, and not in the toroidal field winding. The ability to produce an ohmically ignited and inductively maintained toroidal fusion plasma is the RFP's distinctive advantage, thus a future RFP reactor would not rely on additional heating systems to reach relevant plasma temperatures [7].

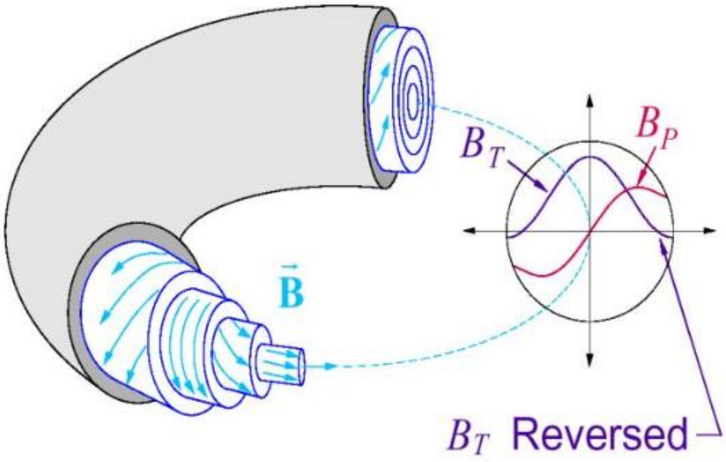

Figure 7 – Radial distribution of magnetic field components of RFP across the minor radius (B_T is the toroidal magnetic field and B_P is the poloidal magnetic field)

Since the 1990s, several RFP devices have been in operation. The largest one is RFX-mod, designed to reach 2 MA maximum current, with a major radius of 2 m and a minor radius of 0.459 m [8] and it will be taken as a reference for following RFP machine magnet system explanation.

As in tokamaks, the toroidal magnetic field is provided by toroidal field coils and the poloidal magnetic flux variation to drive the plasma current by the magnetizing winding, that acts as the CS. Also in a RFP additional poloidal field coils, called field shaping windings in RFX-mod, are necessary for the plasma equilibrium. Since the two components of the magnetic field have a similar amplitude, the toroidal component required in a RFP is about one order of magnitude lower than in a tokamak with equal plasma current and aspect ratio. With much less stringent requirements for the toroidal field coils, their design presents much fewer technological issues than toroidal field coils of a tokamak of the same size. The RFP requires a high toroidal loop voltage during fast plasma current rise and a relatively high toroidal loop voltage during the flat-top. Under these conditions, the magnetizing winding has to store a large flux before the plasma pulse and faces very high voltage across its terminals.

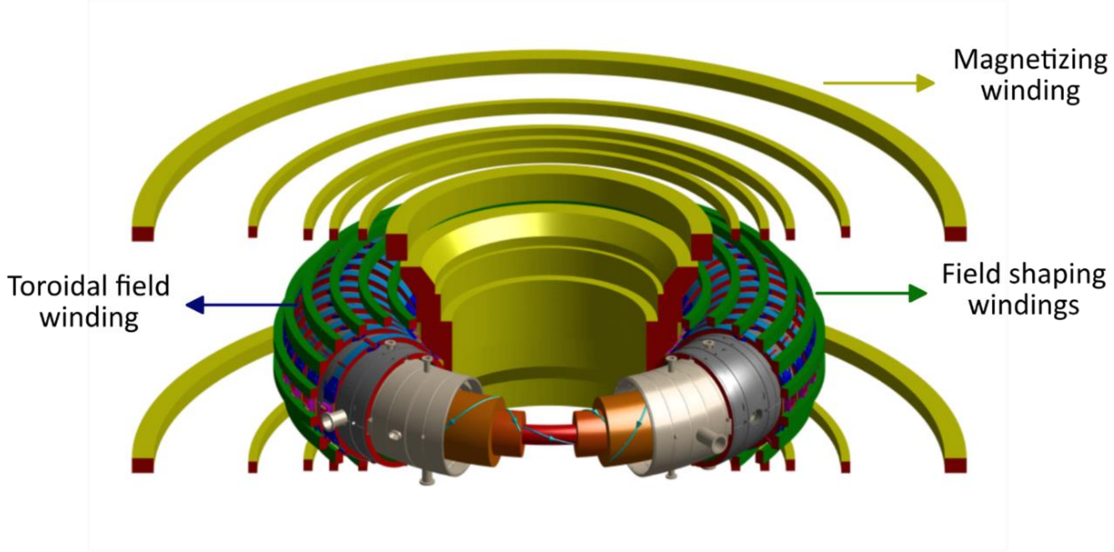

Figure 8 – RFX-mod magnet system

1.4 Coil power supply system for tokamak and RFP experiments

The magnets subsystems are supplied by Coil Power Supply (CPS) systems that differ in terms of adopted technology, voltage and current ratings according to the requirements of the supplied magnets.

The main requirements for the poloidal power supply system are:

- To generate the toroidal loop voltage to ionize the gas and ramp up the plasma current;
- To sustain the plasma current during the flat-top phase;
- To control the plasma position;
- To control plasma instabilities.

The voltage needed for breakdown and plasma initiation (several kV) usually is much higher than the rated voltage of the main power supplies that feed the coils (about 2-3 kV in ITER). The high voltage needed for breakdown and plasma initiation can be generated either using dedicated booster converters or using the energy stored in the magnet system prior to the plasma pulse start. In the latter case, the high voltage is usually obtained by transferring the current circulating in the magnetizing windings into resistances; these energy transfer systems are usually called Switching Network Units (SNUs).

Figure 9 shows a simplified scheme of a poloidal field coil circuit with the main converter that supplies the coil which is series connected with the SNU and the Fast Discharge Unit (FDU) while the Protective Make Switch (PMS) is close in case of fault.

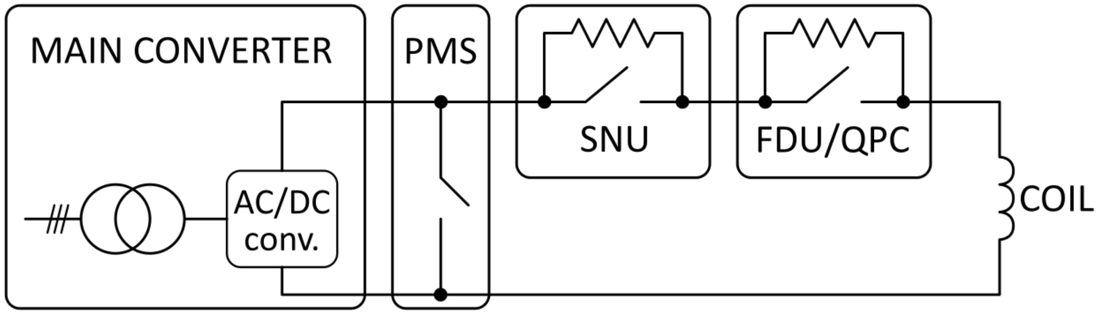

Figure 9 - Simplified scheme of a poloidal field coil circuit

The SNUs are the devices connected in series to thyristor converters in the poloidal circuits to provide additional voltage to the main poloidal coils during plasma breakdown and ramp-up, without any energy exchange with the grid network. This is realized essentially by inserting proper resistors in series to the main base converters, which realize the necessary voltage drop as required by the plasma scenario, as a function of the current following the Ohm's law.

All CS and PF coils shall be quickly discharged (tens of s) in case of quench or other fault conditions, satisfying the coil operative limits in terms of maximum applied voltage and Joule integral. Similarly to ITER and the other superconducting tokamaks, this function is provided by Fast Discharge Units (FDUs), which insert a proper discharge resistor in series with the coil when required.

The poloidal field coils usually are divided into CS sectors and PF coils. To have independent control of each poloidal field coils current, reaching a precise control on the magnetic configuration, usually, each CS and PF coil has a dedicated circuit, as happens in ITER (Figure 10).

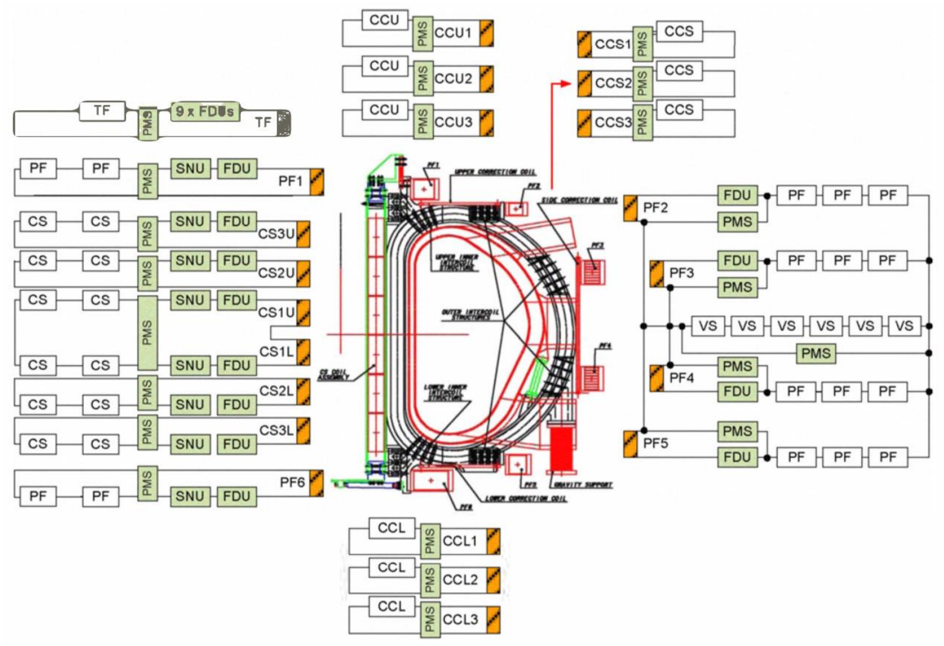

Figure 10 - ITER magnets and CPS subsystems [9]

The typical CS sectors scenario consists of the pre-charge of the coils up to the foreseen initial current, then a phase with a high current derivative to ionize the gas and ramp up the plasma current and then the flat-top phase during which the plasma current is maintained constant, against the resistive dissipation, thanks to a constant derivative of the current in the CS sectors. In the PF coils, there is a different behaviour of the currents that have mainly to control the vertical position of the plasma and therefore they usually have an almost constant current during the flat-top phase with a sign depending on their position with respect to the plasma. Figure 11 and Figure 12 report the current and main converters' voltage waveforms of an EU DEMO scenario for the CS and PF coils.

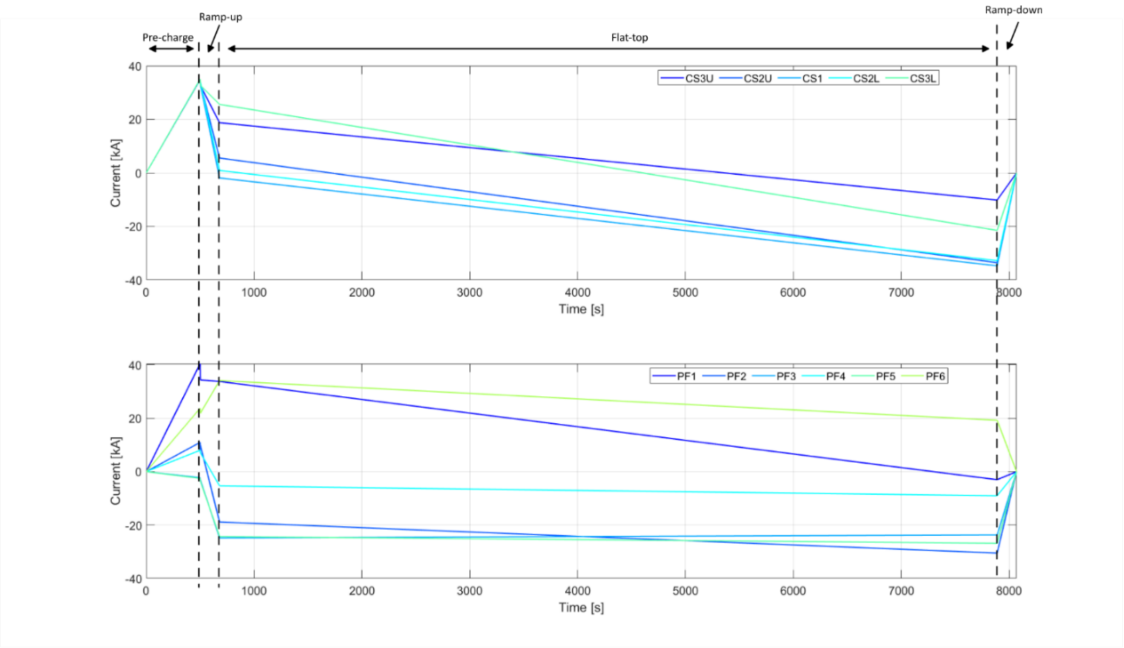

Figure 11 – EU DEMO estimated coils currents in the whole plasma pulse

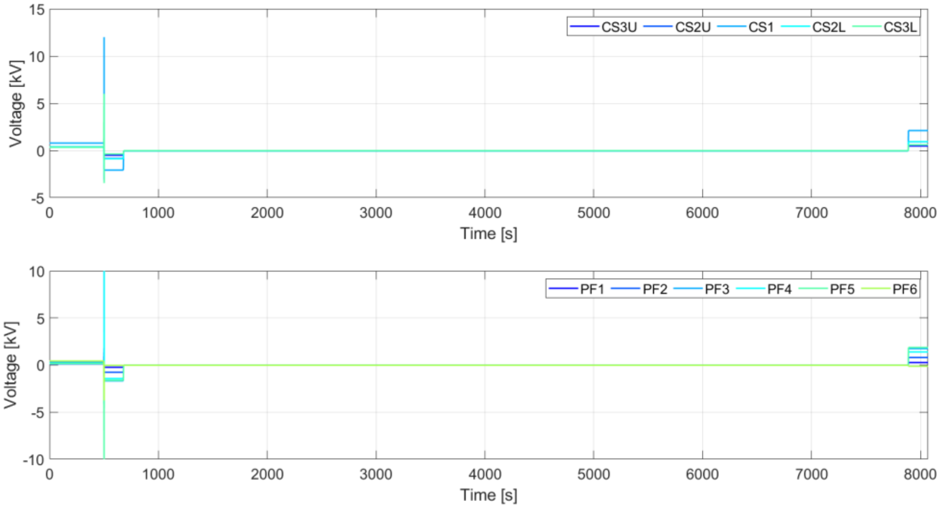

Figure 12 - EU DEMO estimated coils voltages in the whole plasma pulse

Since scenarios for the whole plasma pulse are still not available, the current waveforms on the coils have been estimated on the basis of the limited inputs available, but the scope of this thesis is just to give a qualitative trend of the waveforms in a tokamak.

The main requirement of the toroidal field circuit is to supply the current value in order to produce the desired toroidal field. The voltage rating is related to the required time to complete the charge phase since the converter has to supply a higher voltage during the ramp of the toroidal current to the value needed to produce the desired toroidal field. When this value is reached it has only to supply a lower voltage to maintain this current at a constant value. Line commutated converters are typically used, characterized by high currents (tens of kA) and voltage in the order of hundreds of volts. Usually, the toroidal field coils are divided into sectors made of several coils and a single toroidal converter can supply one or more sectors up to the whole toroidal winding. In JT60SA and also in ITER only one converter supplies the whole toroidal winding. As can be seen in Figure 13, in ITER there is one thyristor converter which supplies the 18 toroidal field coils, grouped in 9 coil pairs interleaved with nine FDUs that dissipate the energy stored in the coils as fast as possible during a fault in order to avoid major damages on the coils. The bypass, Make Switch (MA), Protective Make Switch (PMS) and FDU are operated in coordination according to protection strategies depending on the level of the fault [10].

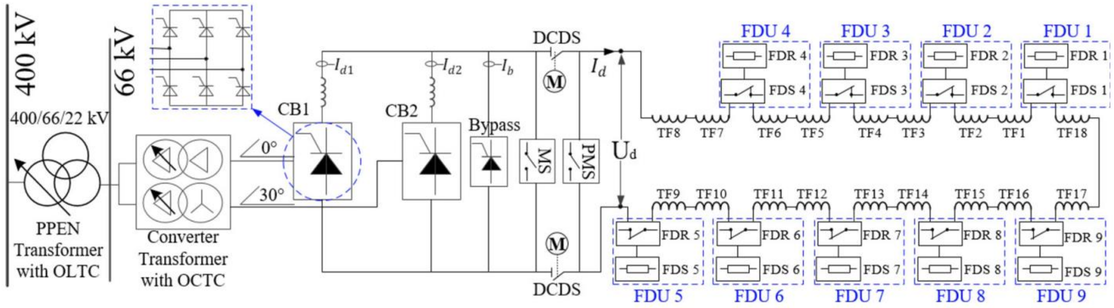

Figure 13 - Circuit topology of ITER TF coils power supply system [10]

1.5 Electrical power management in large fusion experiments

As we get closer to the development of a demonstration fusion reactor for electrical energy production, electrical power management is becoming a crucial aspect in the Coil Power Supply (CPS) system design and in general, in the plant electrical system design.

In magnetic fusion experiments two main issues have been identified regarding the power management related to the CPS system:

- The gas breakdown and plasma current ramp-up and control require high peaks of active power, which increase with the size of the machine and the plasma current value and this problem is relevant for any pulsed large-size reactor.

- The use of thyristor-based converters only, robust and cost-effective technology largely used in all fusion experiments, also in ITER, seems not suitable for supplying SC coils when scaled to large-size experiments, in particular, due to the too huge reactive power demand. The exchange of reactive power between the CPS system and the grid is strictly related to the converter technology and control.

In ITER, the active power peak is expected to reach up to 600 MW, while the reactive power will overcome 900 Mvar [11] during almost all the plasma pulse. Figure 14 shows simulated ITER active and reactive power demand at 400 kV busbar and RPC contribution. As can be seen, the Reactive Power Compensation system (rated 750 Mvar) limits the requested reactive power from the grid under 200 Mvar.

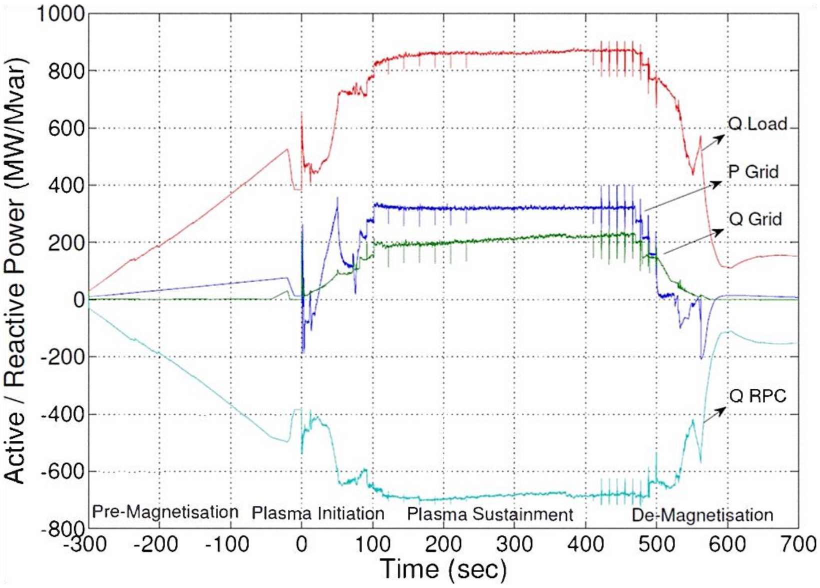

Figure 14 - Active and reactive power profiles at 400 kV [11]

In the EU DEMO, the studies conducted so far [12] give higher estimated values, especially for the reactive power using the ITER-like solution (i.e. thyristor-based converter with sequential control strategy [11]) to supply the main SC coils. As already said, one of the main drawbacks of this technology is the large reactive power absorbed when high currents and low voltage are required by the loads, as occurs during a great part of the plasma pulse, as can be seen in Figure 12.

Recently, the active and reactive power profiles of the CPS system of CS and PF coils are estimated for the complete plasma pulse starting from the scenario reported in Figure 11 and Figure 12 and using the same analytical model presented in [12].

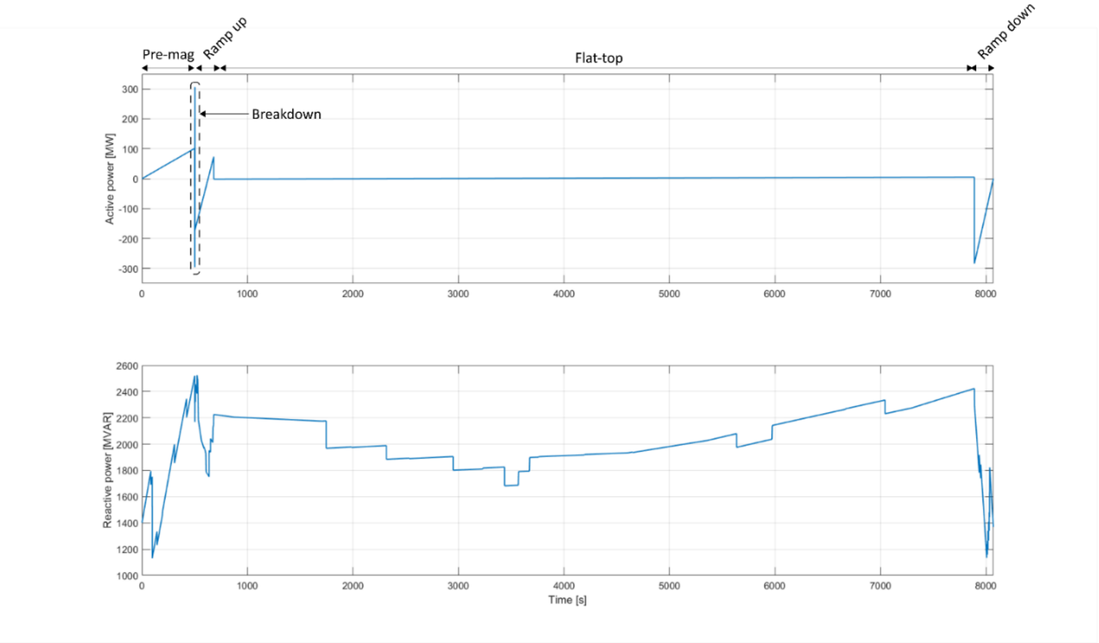

Figure 15 – EU DEMO estimated CS and PF coil power supply system active and reactive power profiles in the whole plasma pulse

The power required during the plasma breakdown by the main coils, mostly by the Central Solenoid (CS), derives from the need for a large magnetizing flux variation to ionize the gas inside the vacuum vessel. In most of past and present experiments, the voltage on the coils during the plasma breakdown is applied by means of transfer resistors (i.e. SNUs) flattening the active power peak seen by the grid but leading to power dissipation and, consequently, efficiency reduction. In future large fusion reactors the utilization of SNUs could not be sufficient, in addition the efficiency reduction could be not viable in reactors with relatively short pulses, like RFP ones, and the adoption of this solution has to be evaluated also considering the cost and reliability of the CPS system. Figure 16 shows the voltage applied to the CS3U (the upper sector of the CS) coil terminal (sum of SNU voltage and converter voltage) and the converter voltage in the EU DEMO scenario reported in Figure 11 and Figure 12. As can be seen with SNU contribution a voltage of – 10 kV is applied to the coil terminal while the converter voltage ranges between -2 kV and 5 kV. In this way the transfer resistor applies a great part of the voltage required during the breakdown while the converter finely regulates the overall voltage. This solution leads to a lower rating of the converter in terms of voltage considering the breakdown phase, but the need to have fast plasma disturbances control could nullify the voltage rating reduction brought by the SNU.

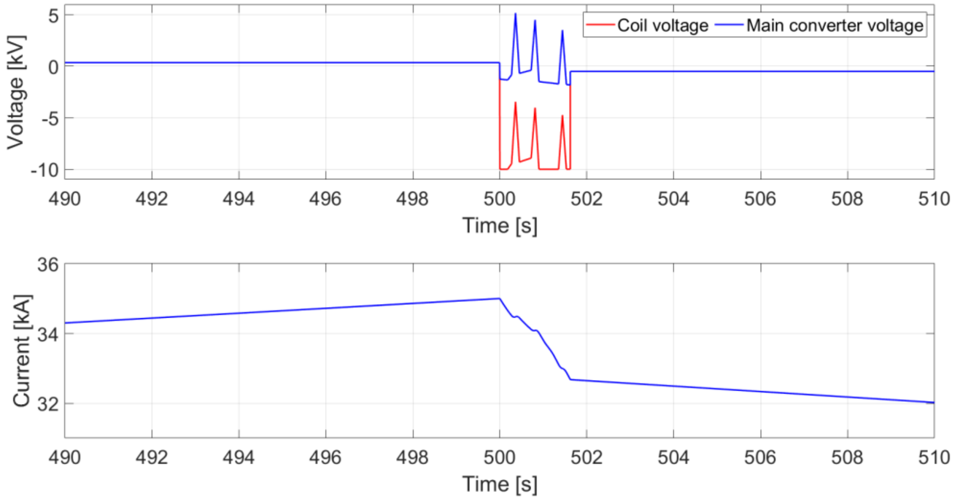

Figure 16 – EU DEMO coil and converter voltage and current of CS3U

Figure 17 shows the power supplied to the CS3U coil and the active power that the main converter required to the grid. This is an example of what has been explained before, the use of the SNU in the CS3U circuit helps to reduce the active power peak during the plasma breakdown.

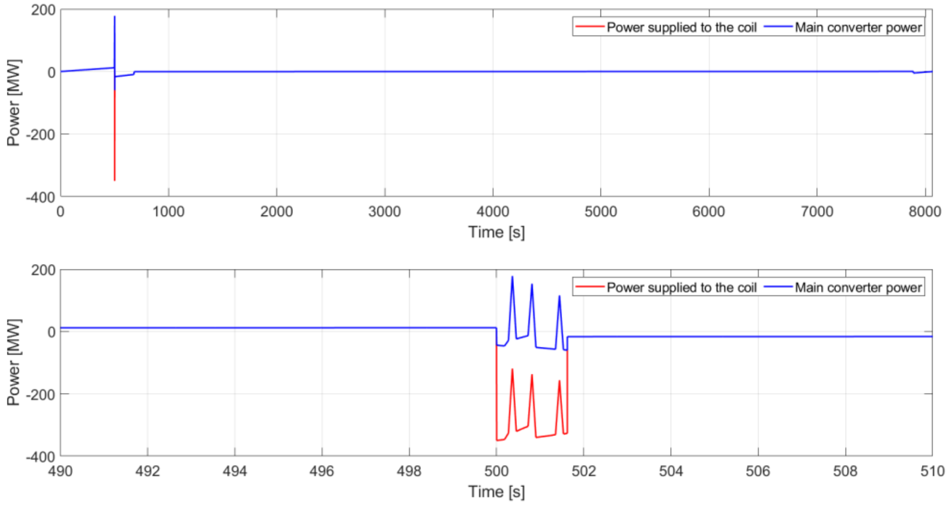

Figure 17 – EU DEMO estimated CS3U coil power and CS3U converter active power, the upper figure reports the complete scenario while the lower one reports a shorter time frame that includes the breakdown phase

The foreseen peaks of active power in the considered plasma scenario for the EU DEMO slightly overcome the limitations usually imposed by the grid operators, both in terms of absolute value and variation in time. As regards the high values of reactive power, the use of RPC systems for reactors much larger than ITER seems a non-viable solution due to the risk of instabilities if too large reactive power compensation systems are installed, and also for the complexity, large area occupancy, and cost of these systems. The site location of EU DEMO is not decided yet, so there are no details about its interface with the Power Transmission Grid (PTG). Preliminary assumptions on the limits imposed by the Transmission System Operator (TSO) for the interface with PTG can be found in [13] and are reported in Table 1.

Table 1 – Preliminary assumptions for interface with the PTG [13]

Reactive power	250 Mvar
Active power peak	600 MW
Active power steps	150 MW
Active power derivative	500 MW/s
Fault power level	>15 GVA

A more detailed overview of the main issues identified so far regarding electrical power management in the EU DEMO can be found in [13].

All the identified problem areas for EU DEMO are still relevant for any pulsed large-size reactor. In the case of a steady-state reactor some issues could be mitigated or absent but high-power transients will be anyway necessary for plasma control.

Under these assumptions, the use of electric energy storage systems in medium-sized and large fusion reactors is expected to become mandatory to supply the high active power peaks without impacting the PTG. On the other hand, the reactive power exchanged between the SC coils power supply and the grid has to be limited and controlled by using advanced converter technologies.

Among the available energy storage technologies, Superconducting Magnetic Energy Storage (SMES) is particularly suitable for large fusion devices, because of its large power density and adequate release time for these applications. Moreover, large fusion devices are provided with superconducting magnets, thus the plant is already equipped with the necessary auxiliaries for superconducting coils.

A new Magnetic Energy Storage and Transfer (MEST) system [14] [15], based on SMES technology, was conceived as a very promising alternative to face both the issues related to high active power peaks and huge reactive power demand. The application of the MEST system to supply the SC coils results in a partial or total degree of decoupling between the grid and the magnets coupled with the plasma, which means that the grid does not have to instantly provide the power delivered to the SC coil and the plasma. Being the MEST a fully new scheme, R&D with industry involvement has to be done to prove the feasibility first, and subsequently, the suitability and convenience of the application to the DEMO case.

A great part of my PhD studies focuses on MEST development and application studies. The studies that I have conducted so far on the MEST system are reported in section 2.

Another alternative solution under investigation is Voltage Source Converter (VSC) with Active Front End (AFE) technology. This solution could be integrated with electric storage, like electrostatic energy storage systems, in principle, to avoid all the SNU, recovering either completely or partially the energy on the storage systems. This type of converter is already largely utilized in industrial applications but at power levels much lower than those required in large fusion reactors like EU DEMO. Thus, also in this case, R&D is necessary, again with industrial involvement; I contributed to the first analyses in 2018 [12] but they are not included in this thesis.

2 RFX-mod2

The RFX-mod experiment is a fusion device designed to operate and explore the plasma physics in Reversed Field Pinch (RFP) configuration at 2 MA of plasma current, with a major radius of 2 m and a minor radius of 0.459 m. The high flexibility of the device discloses the possibility to access and study different magnetic configurations: axisymmetric and helical-shaped RFP equilibria together with tokamak plasmas.

The new version of the machine, named RFX-mod2, foresees the removal of the highly resistive vacuum vessel, transferring the vacuum barrier function to the toroidal support structure. This will optimize the magnetic front-end by the increase of the proximity between the plasma and the highly conductive copper shell [16].

In RFX-mod there are four different groups of magnets [17]:

- Magnetizing winding that generates the flux swing to set up and sustain the plasma current.
- Field shaping windings (F-coils) that control the equilibrium field and compensate the magnetomotive force of the plasma to reduce the equivalent plasma inductance seen by the magnetizing winding.
- Toroidal winding that generates the toroidal magnetic field.
- 192 saddle coils, which cover the plasma boundary, for the feedback control of MHD instabilities.

The poloidal (magnetizing winding and F-coils) and toroidal windings, shown in Figure 18, are supplied by an ac/dc modular conversion system composed of 20 one-quadrant thyristor converter units [18].

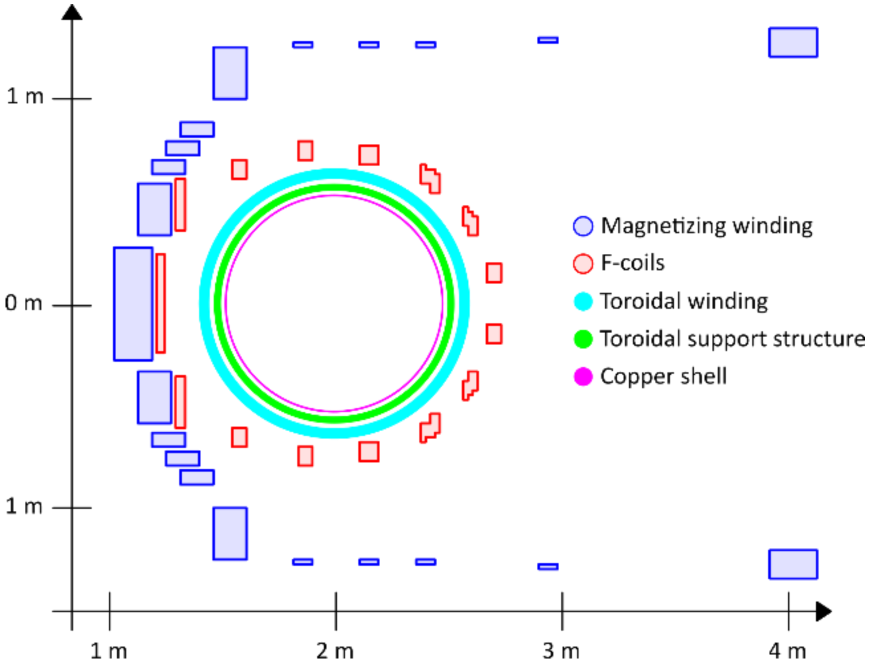

Figure 18 – Simplified scheme of RFX-mod section

The TF winding consists of 48 coils (with a diameter of 1.24 m) evenly distributed and divided in 12 sectors reaching high operational flexibility. These sectors can be arranged in six different arrangements of series-parallel connections resulting in different numbers of turns series-connected and thus different values of the winding self-inductance [17]. In the following sections an upgrade that only affects the poloidal PS system is proposed, therefore the toroidal PS system will not be discussed.

2.1 RFX-mod poloidal circuit and power supply system

The poloidal scheme of RFX-mod is reported in Figure 19. It is usually represented in this octagonal shape and it is divided in four equal sections connected in series.

The magnetizing winding has the main aim to provide a poloidal flux swing of 15 Wb that also represents the magnetic flux to be stored before the plasma pulse. The 200 turns of the magnetizing winding are distributed among 40 M-coils, connected in series to form four sectors interleaved by protection crowbars (PPs) and energy transfer systems. This arrangement of the M-coils in magnetizing winding sectors in the poloidal circuit has the aim to equalize the voltage between the sectors during the plasma pulse. The central solenoid, the part of the magnetizing winding which generates the largest fraction of the magnetizing flux, is composed of 24 out of 40 M-coils and it is placed in the innermost part of the machine. The other M-coils have a greater major radius and vertical distance with respect the equatorial plane. Their placement derives from the need to limit the stray field in the plasma region by a proper shaping of the poloidal field lines.

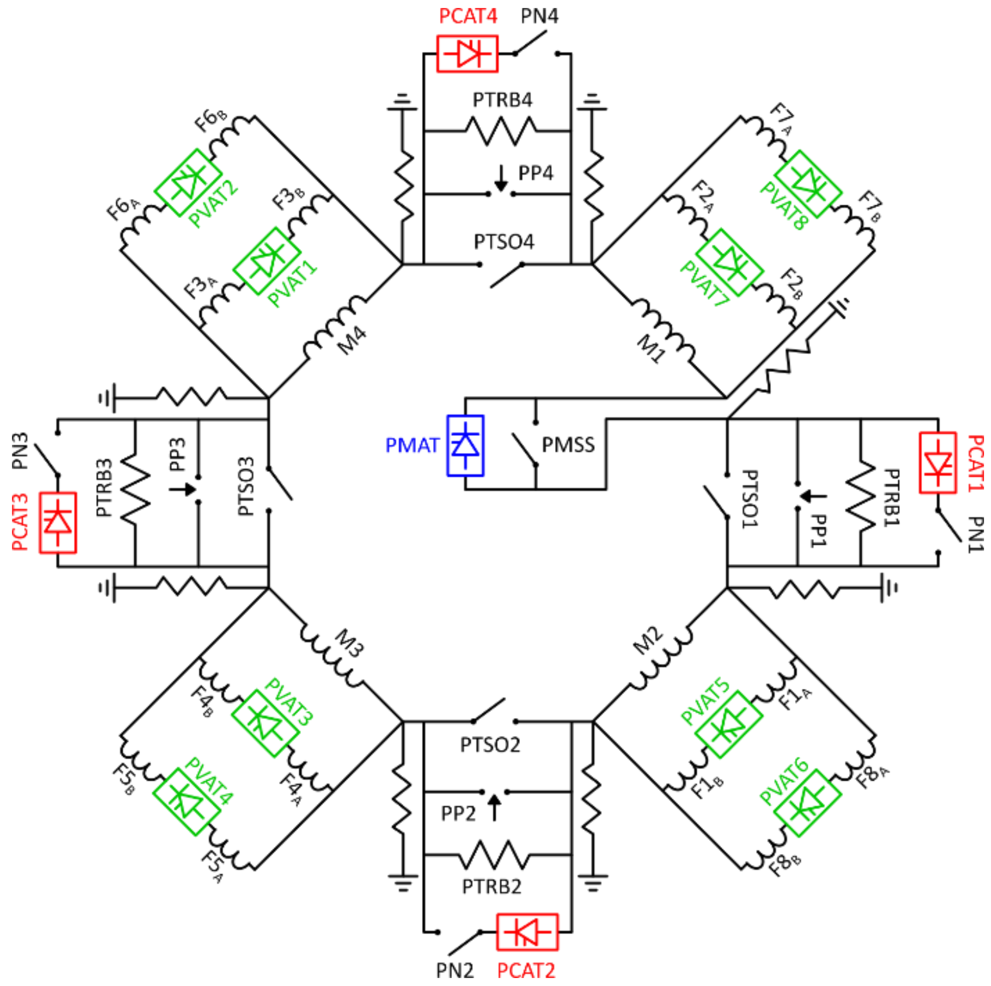

Figure 19 – Scheme of RFX-mod poloidal circuit

Each of the eight couples of F-coils ($F1_A$-$F1_B$…$F8_A$-$F8_B$, where A indicates above and B indicates below the machine equatorial plane) has the current independently controlled by means of a converter (PVAT) achieving a wide range of equilibrium field configurations while the total magnetomotive force of the F-coils is kept equal to the plasma current.

The F-coils and the magnetizing winding sectors are parallel connected, and they are designed to match the value of the self-inductance of each magnetizing winding sector to the mutual inductance with the F-coils in parallel. This distinctive electromagnetic design provides an intrinsic balance of the voltage induced in the F-coils and magnetizing winding sectors, leading the currents in the F-coils to naturally be induced by only the plasma current with a distribution approaching the required values, so minimizing the voltage ratings of the PVAT converters [17].

The PVATs converters independently control the current in each F-coils couple and have two main tasks:

- to generate the equilibrium field to control the plasma position;

- to compensate the plasma MMF leading the 16 F-coils to carry the image of the plasma current thus reducing the poloidal flux swing requirements.

The two main components of the four energy transfer system units are the vacuum circuit breaker (PTSO1…4) and the four transfer resistors (PTRB1…4). They have to divert the current from the PTSOs, which short circuit the four magnetizing winding sectors before the plasma breakdown, to the transfer resistor PTRBs. The magnetizing flux swing, deriving from the abrupt decrease of the magnetizing current, allows to set-up the plasma and the energy transfer from the magnetizing winding to the plasma inside the vessel.

The poloidal crowbars PP1...PP4, able to withstand the magnetizing current, were designed to reduce the fault overvoltage on the coils by short circuiting the transfer resistors [18]. Figure 20 is a photo of the poloidal power supply hall in which PMSS, PNs, PPs, PTRBs and PTSOs are highlighted.

Figure 20 – RFX-mod power supply hall

The power supplies of the poloidal and toroidal circuit of RFX-mod, described in detail in [21] and [22], include two different types of one-quadrant thyristor converters that can be combined gaining a high level of flexibility of the PS system.

The converter units are:

- 12 type A converter units: each composed of two independent sub-units that can be series or parallel-connected reaching different ratings of the converter unit reported in Table 2.

- 8 type B converter units: rated 2 kV (no-load) and 6.25 kA with a duty cycle of 5 s/600 s or 8.12 kA reducing the duty cycle to 0.5 s/600 s.

Each type A converter unit, reported in Figure 21, is composed of two independent sub-units rated for a no-load voltage of 2 kV and a current of 6.25 kA with a duty cycle of 5 s/600 s or 8.12 kA reducing the duty cycle to 0.5 s/600 s. The subunit comprises two parallel-connected basic bridges, each provided with a Free-Wheeling (FW) diode and a fast thyristor crowbar to protect the subunit against over-voltages that can arise across the converters in case of fast plasma current termination or fault conditions. Each subunit is fed by a step-down transformer, connected at the primary side to the 22 kV Medium Voltage (MV) distribution system. The proper current/voltage sharing between the two basic bridges of the same subunit is guaranteed by the almost equal impedance of the upstream cables, while the current/voltage sharing between the series or parallel connected subunits is achieved by the internal subunits feedback control.

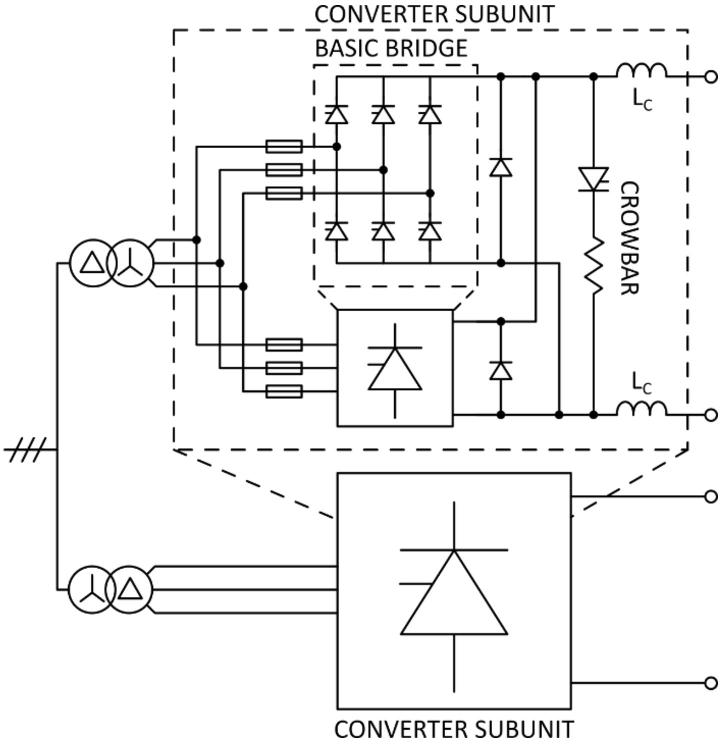

Figure 21 – Scheme of a type A converter unit

The two independent subunits of each converter unit can be series or parallel-connected reaching two ratings for the converter units reported in Table 2.

Table 2 – Converter type A unit possible ratings

	Series-connected subunits	Parallel-connected subunits
Rated current	6.25 kA (5/600) 8.12 kA (0.5/600)	12.5 kA (5/600) 16.25 kA (0.5/600)
Rated voltage	3 kV (on load) 4 kV (no-load)	1.5 kV (on load) 2 kV (no-load)

As described in the next section, in a standard pulse the pre-magnetization and plasma sustainment functions are accomplished by 4 type A units in parallel (PMAT) and 4 (PCAT) type A converters respectively (Figure 19). This solution allows reducing the cost and size of the PS system with respect to adopt only one converter to perform the two functions. However, being different the ratings of PMAT (4 parallel A units) and PCATs (one A unit each) in terms of current, the magnetizing winding cannot be exploited in its full current range (+50 kA to -50 kA).

This design choice, in accordance with the 15 Wb of poloidal flux swing specified by the design requirements of the experiment [17], prevents an increase of the maximum achievable plasma current and flat-top duration.

The ac/dc conversion system of the toroidal field windings, in the initial reference configuration, comprises four A type converter units while the F-coils are supplied by type B units. Type B units have a similar scheme (Figure 21) but with only one basic bridge for each subunit so that the B unit rating has half current limit of the A unit.

2.1.1 RFX-mod standard pulse and EPFC scenario

A typical RFX-mod plasma pulse is shown in Figure 22 and Figure 23 and it is divided into four phases: pre-magnetization, plasma current ramp-up, plasma current sustainment (also called flat-top) and plasma current ramp-down which will not be addressed in the following sections. In Figure 22 and Figure 23, i_M is the magnetizing current, i_P is the plasma current and i_{RT} is the transfer resistors current.

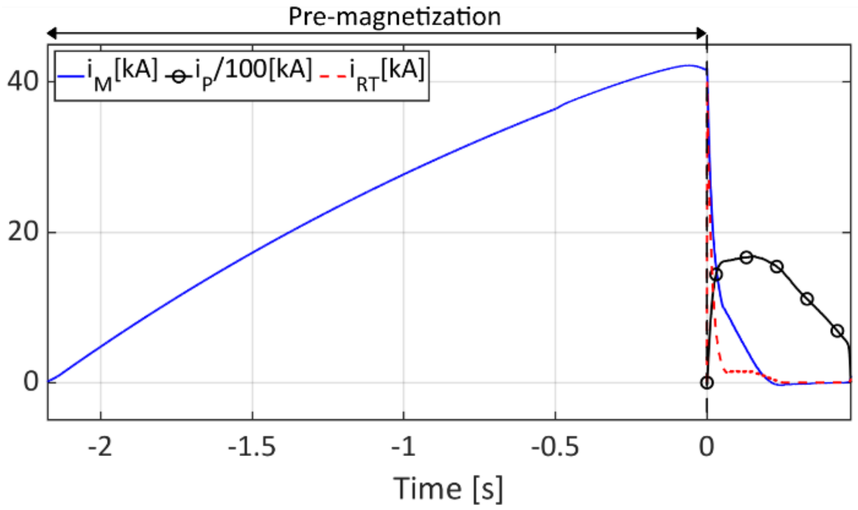

Figure 22 – Current waveforms during a standard RFX-mod pulse (pulse number 36175)

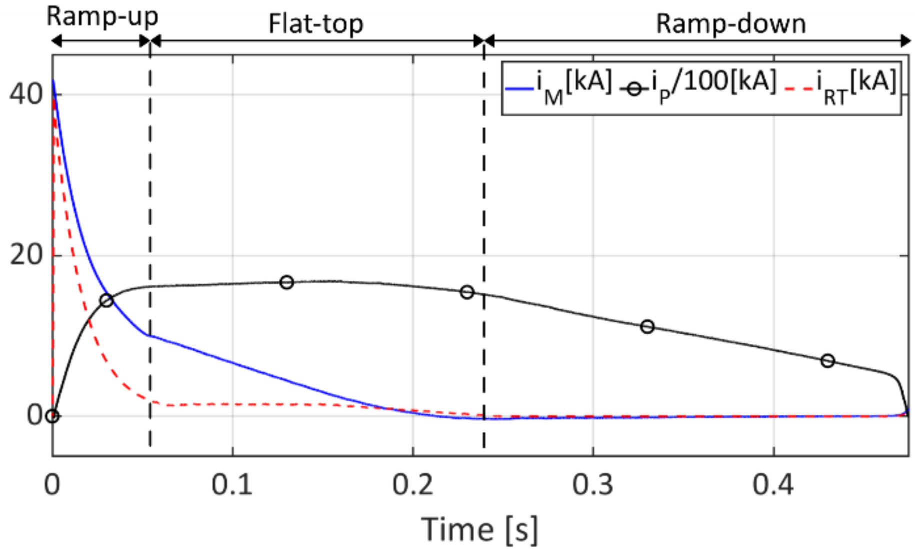

Figure 23 – Ramp-up, flat-top and ramp-down current waveforms during a standard RFX-mod pulse (pulse number 36175)

The operation of the circuit in Figure 19 can be summarized as follow:

- **Pre-magnetization**: initially the making switches PN1…4 and the PNSS are opened while the circuit breakers PTSO1…4 are closed. The PMAT converter pre-magnetizes the magnetizing winding sectors (M1…4) with a current up to 50 kA. Figure 24 shows the RFX-mod poloidal circuit during pre-magnetization phase with the magnetizing current path highlighted in blue.

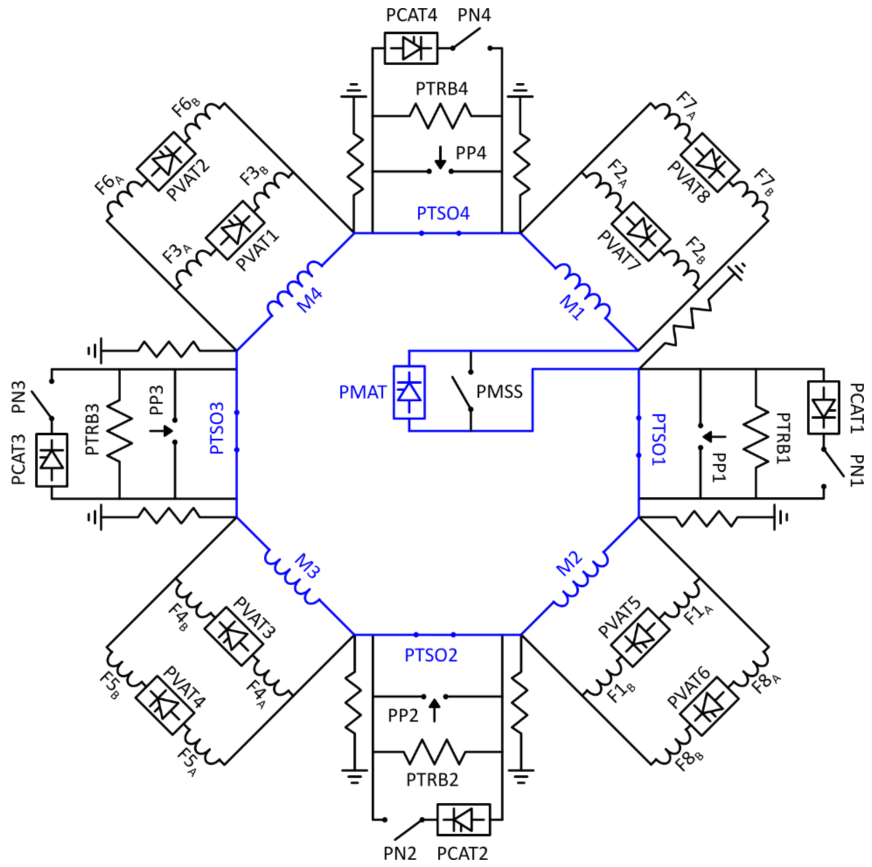

Figure 24 - Scheme of RFX-mod poloidal circuit during pre-magnetization phase

- **Plasma breakdown and plasma current ramp-up**: some tens of ms before the plasma initiation the PMAT is switched off and the PMSS is closed. The pulse starts when the four PTSOs opens inserting in the circuit the four transfer resistors PTRBs. The fast magnetizing current decreases and the resulting poloidal flux swing induces a toroidal loop voltage inside the vacuum vessel sufficient for the gas ionization and the plasma current ramp-up. During this ramp-up phase part of the previously energy and volt-seconds stored in the magnetizing winding is transferred to the plasma. Figure 25 shows the RFX-mod poloidal circuit during the plasma breakdown and plasma current ramp-up with the magnetizing current path highlighted in blue and the PTSOs and PMSS operations with red arrows. During this phase, the flat-top and the ramp-down current flows also in F-coils and PVATs to control the plasma position and compensate for the magnetomotive force of the plasma.

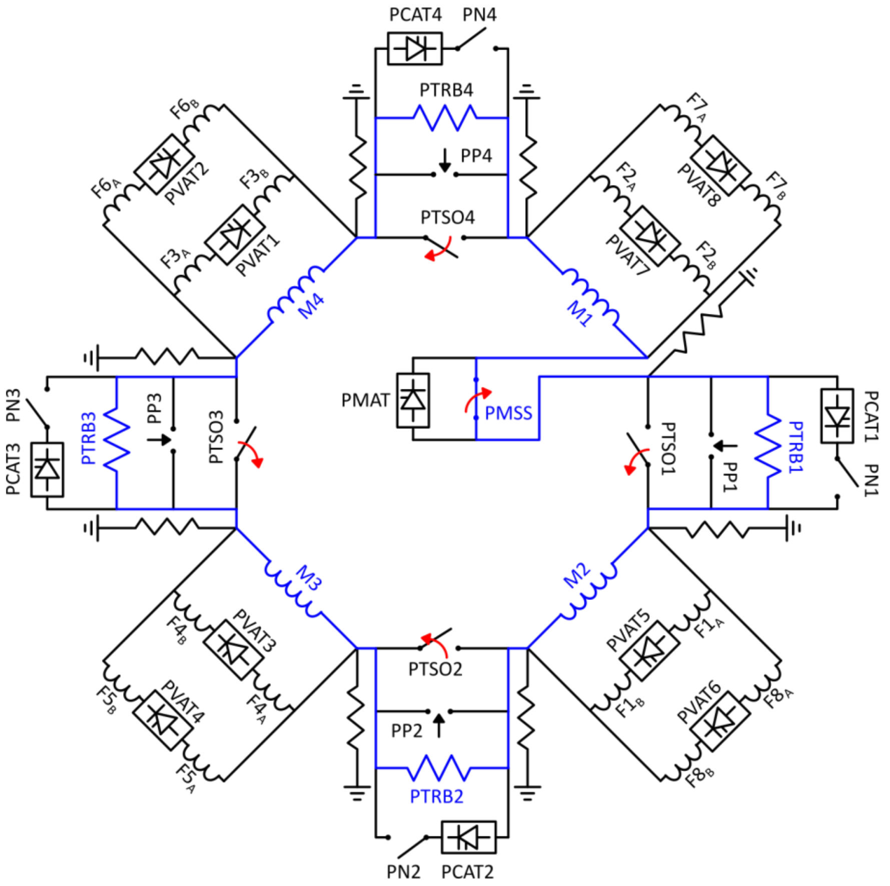

Figure 25 - Scheme of RFX-mod poloidal circuit during plasma breakdown and plasma current ramp-up, the magnetizing current path is highlighted in blue.

- **Plasma current flat-top**: when the voltage on the transfer resistors is insufficient to sustain the plasma current the PCAT units are inserted by closing the making switches PN1…4. The PCAT voltage is directly applied to the magnetizing winding maintaining a flux variation that can be actively controlled in order to obtain the desired plasma current waveform. Figure 26 shows the RFX-mod poloidal circuit during the flat-top phase with the magnetizing current path highlighted in blue and the PMs operation with red arrows.

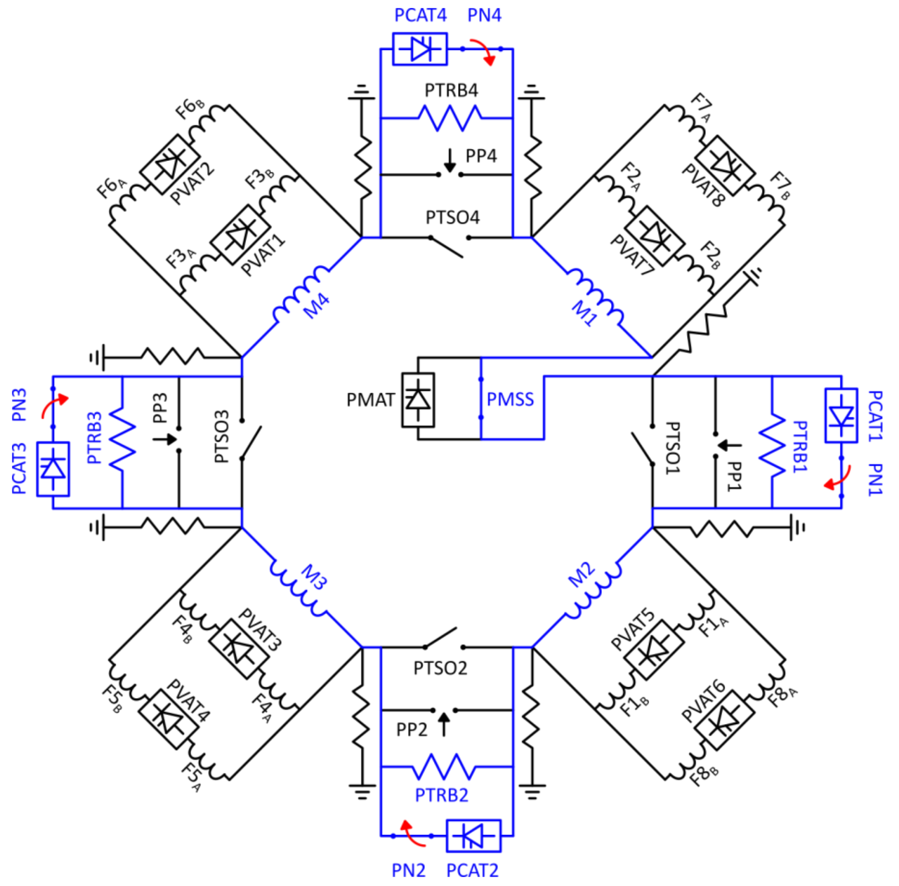

Figure 26 - Scheme of RFX-mod poloidal circuit during flat-top phase, the magnetizing current path is highlighted in blue.

- **Plasma current ramp down**: When the PCATs reach their maximum current the plasma current cannot be sustained anymore and decreases to zero, leading to the end of the pulse.

To better understand the F-coils current behaviour during the pulse, Figure 27 reports the current of each couple of field shaping coils.

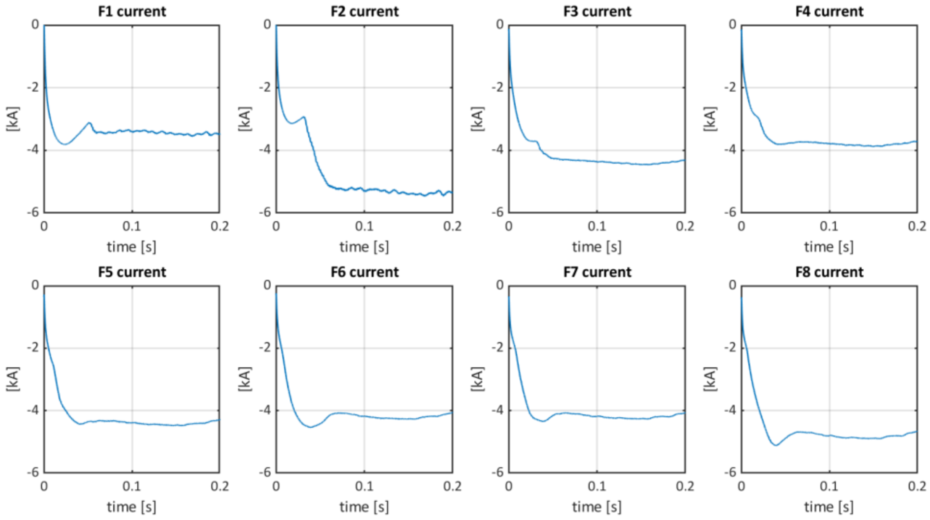

Figure 27 – F-coils currents during a standard RFX-mod pulse (pulse number 36175)

In the figure can be seen that the currents in coils follows the plasma current to compensate the plasma magnetomotive force and in the meantime they have a distribution of the currents that allows to control the plasma position generating a vertical magnetic field. Figure 28 reports the F-coils and plasma ampere turns during the pulse, and it is clear the plasma magnetomotive force compensation done by the F-coils. The total ampere turns of the F-coils have an opposite sign but is reported with the same sign of the plasma ones to better compare them.

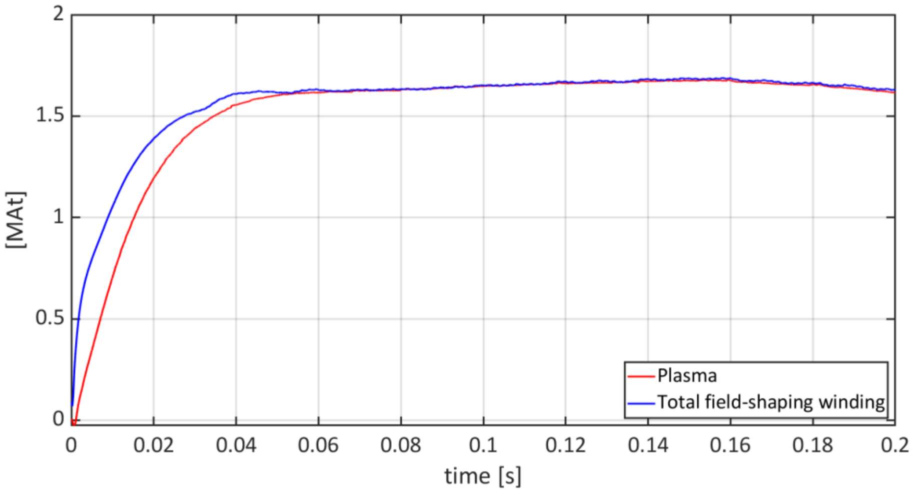

Figure 28 - F-coils and plasma ampere turns during a standard RFX-mod pulse (pulse number 36175)

The converter units configuration originally adopted for a standard pulse is shown in Figure 29 for the PMAT, PCATs and TFAT. As can be seen the PMAT comprises four parallel-connected converter units achieving the maximum current of 50 kA. Each PCAT consists of one converter unit rated 2 kV no-load and 16.25 kA (0.5 s/600 s).

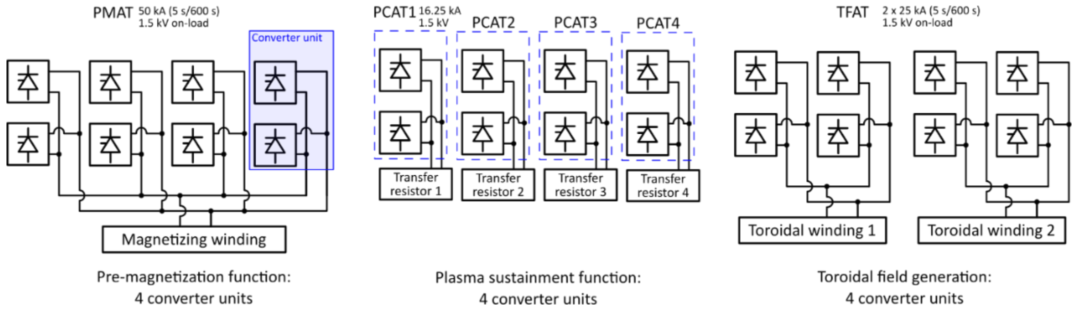

Figure 29 – Reference configuration

Thanks to the flexibility of the PS system, other configurations of the converters have been adopted, according to the needs of the RFX-mod experimental campaigns [23], [24]. A relevant rearrangement of the system, described in [23], allowed to reliably reach a plasma current of about 2 MA with the so-called Enhanced Poloidal Flux Capability (EPFC) scenario. The need for a higher poloidal flux variation together with the overabundant available toroidal flux has led to shift part of the available converter units from the toroidal winding PS system to the poloidal PS system. This allowed for the increase of the poloidal flux variation. The PMAT, PCATs and TFAT configurations to reach the EPFC scenario are reported in Figure 30.

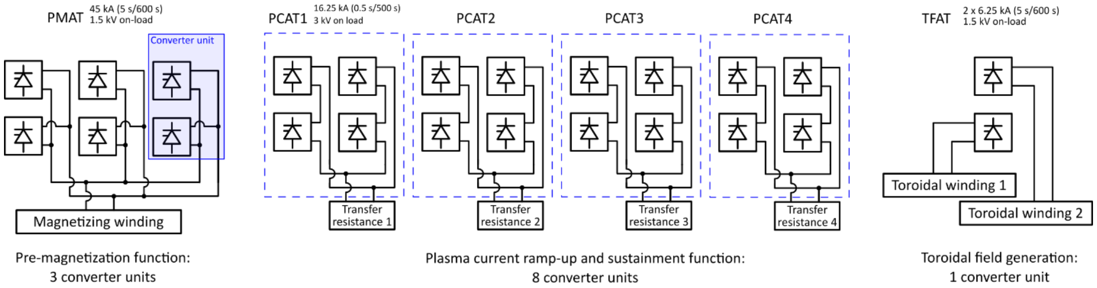

Figure 30 –EPFC configuration

In the EPFC scenario the PMAT comprises three parallel connected converter units achieving the maximum current of 45 kA. This maximum current, higher than 37.5 kA, has been achieved by the full exploitation of the power capability of the converter units which compose the PMAT [23].

Each PCAT, with the EPFC scenario, consists of one converter unit rated 4 kV no-load and 16.25 kA (0.5 s/600 s). With this configuration, when PCATs are inserted, they can provide a toroidal loop voltage exceeding the plasma voltage drop. Therefore, the PCATs can drive the last part of the plasma current ramp-up in order to reliably reach high values of plasma current. In Figure 31 a plasma discharge operating the EPFC scenario can be seen. The magnetizing winding has an initial current of 45 kA, in the first 40 ms the plasma current reaches 1.7 MA thanks to the magnetizing winding current decrease operated by the transfer resistors. Then the PCATs apply 2.8 kV for 35 ms increasing the plasma current up to 1.9 MA and then they apply 1.2 kV to maintain the plasma current for 100 ms.

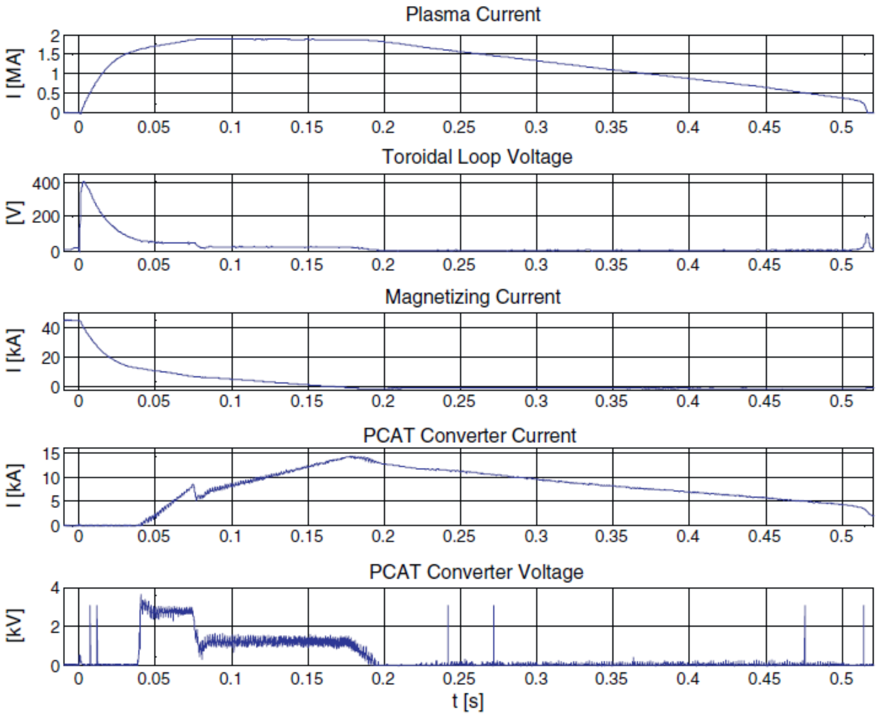

Figure 31 – Main measures of shot #28676 [23]

2.1.2 RFX-mod poloidal circuit model

To simplify the first studies on achievable plasma current and flat-top duration, a simplified RFX-mod poloidal circuit magnetically coupled with the plasma is adopted. Figure 32 shows the simplified poloidal circuit of RFX-mod magnetically coupled with the plasma, represented by the plasma inductance L_P' and resistance R_P'. The simplified circuit collapses the four poloidal circuit sectors in one, thanks to the symmetry, and provides an easy evaluation of the poloidal circuit behaviour for a preliminary evaluation of the achievable plasma current and flat-top duration. The four PCATs and transfer resistors are series-connected forming the PCAT converter and R_T resistor of the simplified circuit. PVAT converters are not considered in the equivalent circuit because their function to guarantee the plasma magnetomotive force compensation can be simulated by a proper reduction of the plasma inductance. The whole magnetizing winding is represented by the inductance L_M. S1, S2 and S3 represent the functions of PMSS, PTSO1…4 and PN1…4 respectively. The magnetizing flux can be considered fully linked with the plasma, therefore the mutual inductance M between L_M and L_P' is equal to L_M. L_P' takes into account both the leakage inductance to consider the volume between the F-coils and the plasma and the actual plasma inductance.

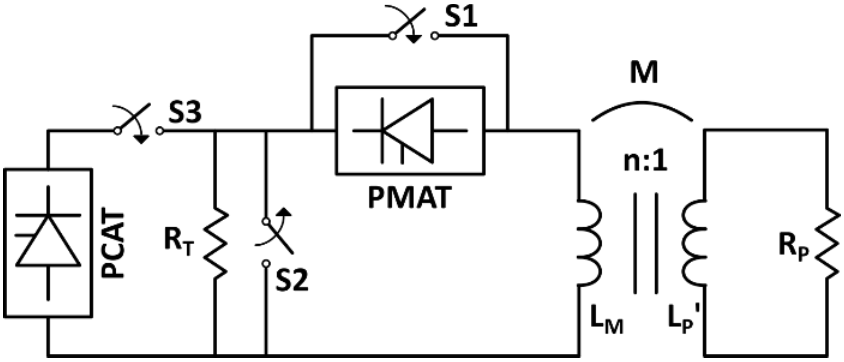

Figure 32 – Simplified scheme of RFX-mod poloidal circuit.

From the simplified scheme of Figure 32 the equivalent T-circuit, reported in Figure 33, has been derived so that the plasma is referred to the magnetizing winding side with a turn ratio of 200 (n), the number of the magnetizing winding turns, R_M is the magnetizing winding resistance, L_{SM} is the leakage inductance to consider the volume between the F-coils and the plasma.

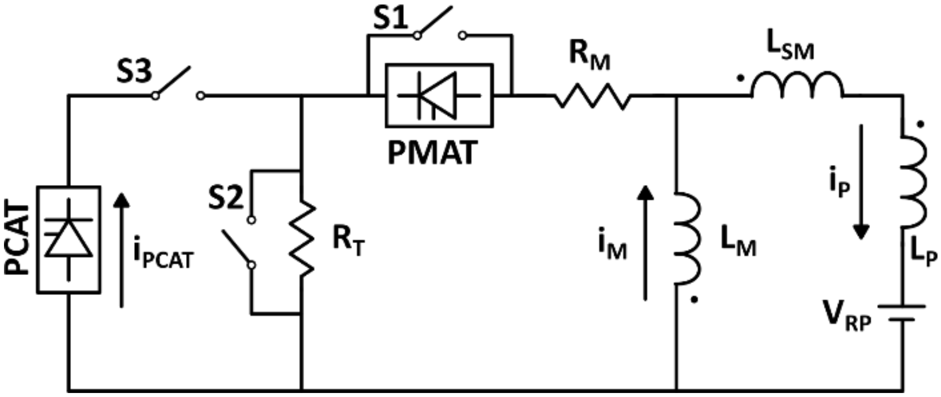

Figure 33 – Simplified equivalent circuit of the RFX-mod poloidal circuit.

To explain the parameters derivation from the simplified scheme to the equivalent T-circuit, in Figure 34 is reported the circuit representing the magnetic coupling, with the following parameters:

- L_M: Inductance of the magnetizing winding.
- R_M: resistance of the magnetizing winding.
- i_M: Magnetizing winding current.
- L_P’: Plasma inductance that is the sum of L_M, the plasma inductance L_P and the leakage inductance L_{SM} inductance to consider the volume between the F-coils and the plasma.
- R_P: Plasma resistance.
- i_P: Plasma current.

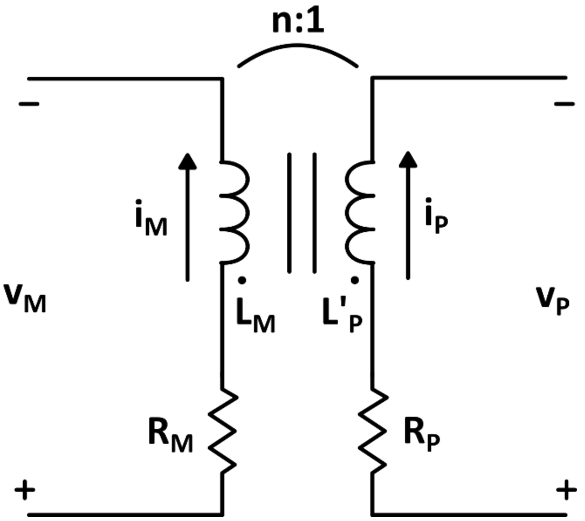

Figure 34 – Schemtatic representation of the mutual coupling between the magnetizing winding and the plasma

Considering the equivalent t-circuit of the coupled inductors L$_M$ and L$_P$ reported in Figure 35, on the magnetizing winding side there are the following inductances:

$$L_A = M = L_M = 58\,mH \qquad \text{Eq. 6}$$

$$L_C = L_M - M = 0\,H \qquad \text{Eq. 7}$$

$$L_B = L'_P - M = (L_{P,st}n^2 + L_{SM} + L_M) - M = L_P + L_{SM} \qquad \text{Eq. 8}$$

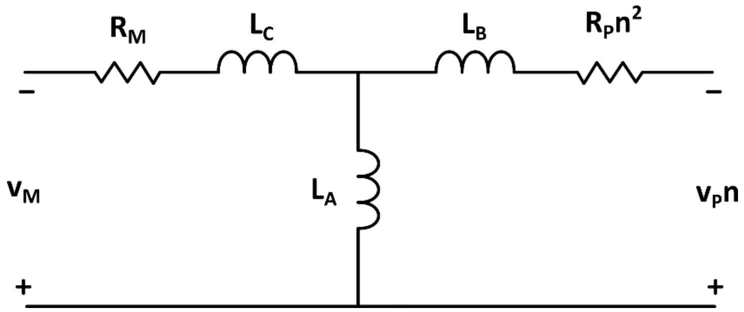

Figure 35 – Equivalent t-circuit of the mutual coupling between the magnetizing winding and the plasma at the magnetizing winding side

To have an initial reference value, the plasma inductance at the plasma side (L$_{P,st}$) can be estimated considering two components: the plasma internal inductance (L$_{P\text{-int}}$) and the plasma external inductance (L$_{P\text{-ext}}$). The internal inductance is related with the total magnetic flux inside the plasma, since the external toroidal magnetic flux is negligible with respect the one generated by the plasma itself:

$$L_{P-int} = 1\ \mu H \qquad \text{Eq. 9}$$

This value come from RFX-mod experience. The plasma external inductance can be calculated as the inductance of a thin wall cylindrical conductor with a superficial distribution of current, without considering the internal magnetic flux:

$$L_{P-ext} = \mu_0 r_i \left(\ln\left(\frac{8R}{a}\right) - 2\right) = 1.25 \cdot 10^{-6} \cdot 1.995 \cdot \left(\ln\left(8 \cdot \frac{1.995}{0.4995}\right) - 2\right) = 3.65\ \mu H \qquad \text{Eq. 10}$$

With R and a the major and minor radii respectively. The total plasma inductance is:

$$L_{P,st} = L_{P-int} + L_{P-ext} = 1\ \mu H + 3.65\ \mu H = 4.65\ \mu H \qquad \text{Eq. 11}$$

Therefore:

$$L_B = L_P + L_{SM} = L_{P,st} \cdot n^2 + L_{SM} = 186\ \mu H + 30\ \mu H \qquad \text{Eq. 12}$$

The value of L_{SM} derives from measurements done on RFX of the inductance between the F-coils and the vessel, therefore it represents the magnetic energy stored in the volume between the F-coils and the plasma. The value of plasma inductance has been adjusted by comparing the numerical results with RFX-mod data and the value used in the numerical simulation is reported in Table 3.

The plasma resistance V_{RP} is implemented through a controlled voltage source with a value of 20 V. Figure 36 reports the plasma loop voltage of the RFX-mod pulse 36175 with a plasma current of 1.6 MA.

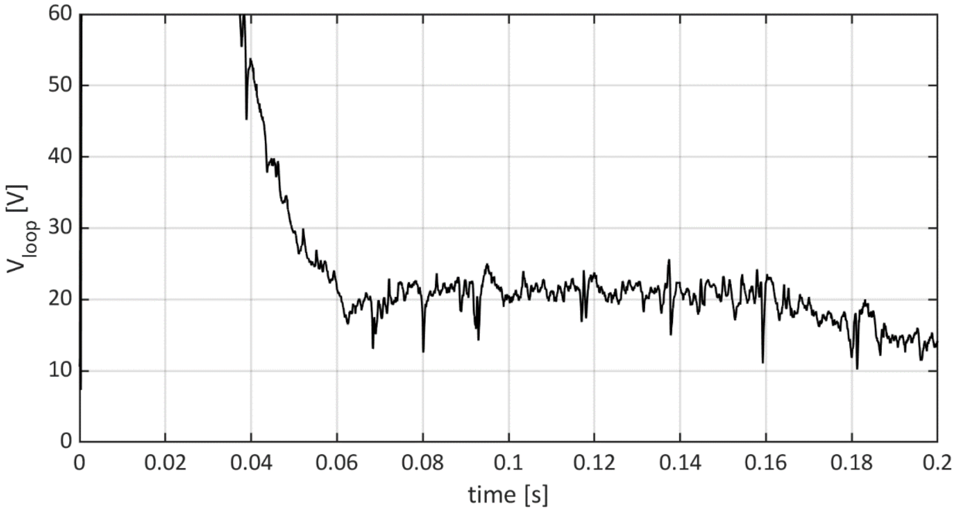

Figure 36 – Plasma loop voltage during a standard RFX-mod pulse (pulse number 36175)

The plasma loop voltage in a RFP device decrease with increasing plasma current, for given dimensions of the machine following the relation [25]:

$$V\ \alpha\ Ra^{-0.35}I_P^{-0.65} \qquad \text{Eq. 13}$$

Where R and a are the major and minor radii respectively and I_P the plasma current.

Table 3 reports the converter ratings and the details of the elements used in the numerical model.

Table 3 – Circuit ratings of RFX-mod numerical model

PMAT	50 kA/1.5 kV	L_{SM}	30 mH
PCAT	16.25 kA/6 kV	L_P	170 mH
L_M	58 mH	V_{RP} (n=200)	20·n V
R_M	20 mΩ	R_T	2.4 Ω

The results of the numerical model implementing RFX-mod simplified circuit have been compared and assessed with different RFX-mod experimental pulses (like the one shown in Figure 22 and Figure 23).

The obtained waveforms, compared with the experimental results, are coherent in terms of plasma current (which reaches similar values with equal pre-magnetization current), converters currents, transfer resistor voltage and duration of the pulse phases. Figure 37 shows a comparison between the plasma and magnetizing current of the pulse number 36175 of RFX-mod (i_{Ps} and i_{Ms}) and the numerical model (i_P and i_M) during ramp-up and flat-top phases. As can be seen the agreement between the simulated and the experimental data is satisfactory for the purposes of these studies.

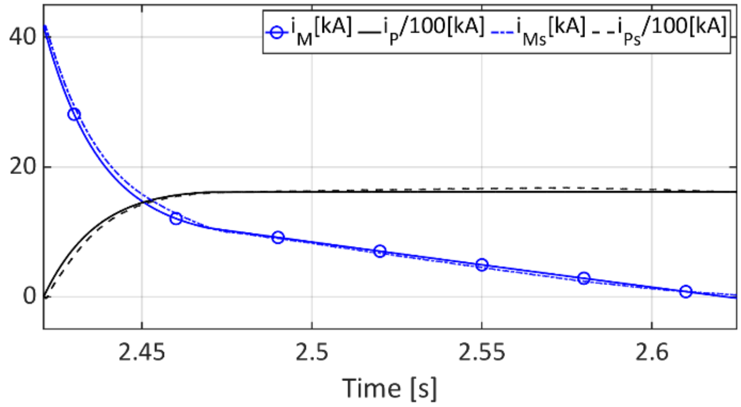

Figure 37 – Plasma current and magnetizing current evolutions. i_{Ms} and i_{Ps}: experimental data of RFX-mod pulse 36175; i_M and i_P: simulation results of the numerical model.

In Figure 38 the main current waveforms of the numerical simulation of RFX-mod plasma pulse with a plasma current up to 1.96 MA are shown. At t=0 s the pre-magnetization phase starts and at t=3.32 s the switch S2 is opened.

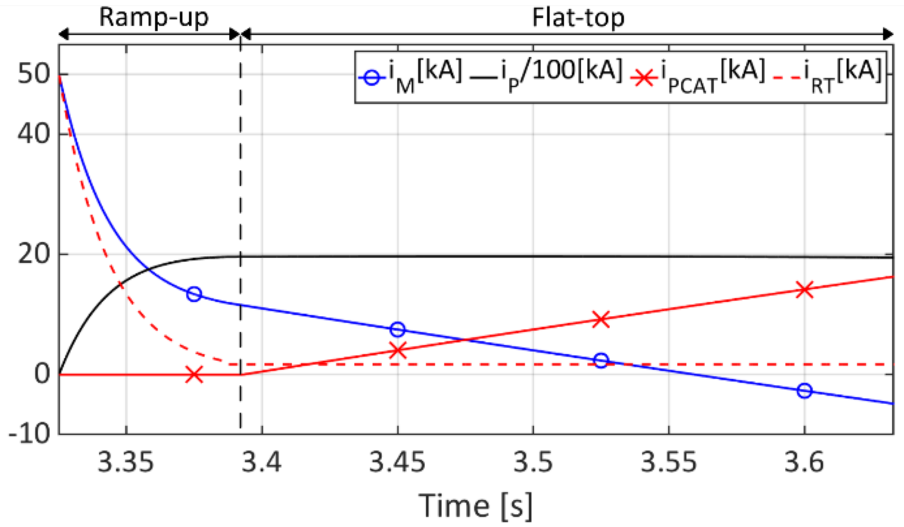

Figure 38 – Main current waveforms of the numerical simulation of RFX-mod plasma pulse.

3 Proposed upgrades of the poloidal PS system to increase the plasma current and flat-top duration

In sections 3.1 and 3.2 two possible reconfigurations of RFX-mod2 poloidal Power Supply (PS) system are proposed with the objective to increase the maximum achievable plasma current and flat-top duration, over the initial target performance, essential to explore the new advanced confinement scenarios and to fully exploit and raise the new potential of the RFP configuration.

With the proposed solutions the magnetizing winding can operate in the so called “double swing mode” because the magnetizing current reverses towards high negative values. Exploiting a wider range of the magnetizing current, the available poloidal magnetic flux variation can increase as shown in Figure 39.

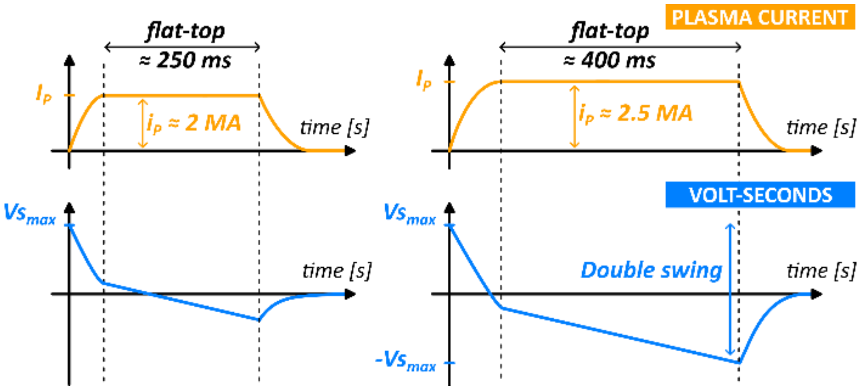

Figure 39 - Simplified representation of the plasma current and magnetizing flux of a RFX-mod pulse (on the left side) and the expected ones with the double swing of the magnetizing flux (on the right side)

In the field of RFP plasma studies, the RFP physics at higher plasma current could be crucial to confirm positive trends like the electron temperature increase (Figure 40) and also the persistence and duration of Quasi-Single Helicity (QSH) states (Figure 41) [26] [7] [27]. The achievement of improved confinement scenarios and increasing the confidence in such extrapolations could lay the foundation to conceive future reactors based on RFP magnetic configuration, as PILOT.

In the frame of the studies to exploit the new potential of RFX-mod2 achieving a higher plasma current and longer flat-top duration, a solution based on additional magnetic energy storage is proposed in section 3.1 and one based on an electrostatic energy storage is presented in section 3.2. The key driver of these two solutions is a limited upgrade of the RFX power supply system, without overstressing the poloidal windings or overcoming the power limits of the main step-down transformers (300 MVA) and maintaining the present set of thyristor converters units.

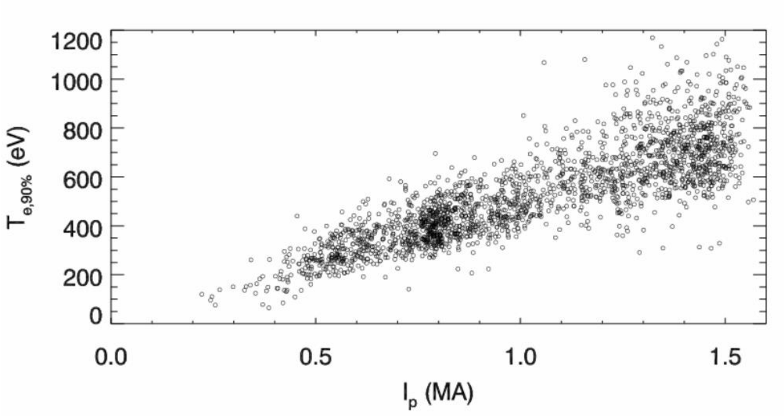

Figure 40 - RFXmod electron temperature vs plasma current [26]

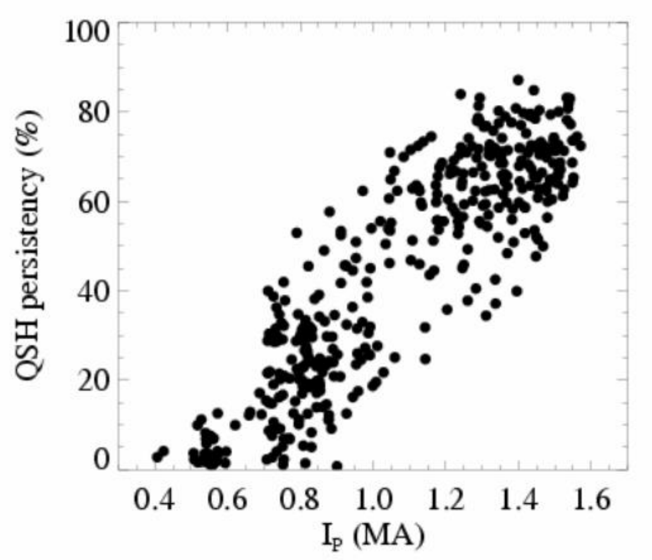

Figure 41 - Persistency of the QSH phase as a function of plasma current in RFXmod [26] [27]

3.1 Magnetic energy storage solution

The increase of the maximum plasma current and flat-top duration, under the current and mechanical limits of the coils, can be reached using additional magnetic energy storage and a complete revision of the configuration and operating principle of the power supply system of the poloidal field coils. With this new operational concept, during the charging phase, the magnetizing winding is charged along with an additional inductor, which acts as an energy storage reservoir. The stored energy, in the order of 100 MJ, is transferred to the magnetizing winding, and thus to the plasma, via transfer resistors in the last phase of the plasma current ramp-up, to reach values of plasma current up to 2.6 MA. This solution avoids the overcoming of the power limits of the main transformers (300 MVA) and allows maintaining the present thyristor converters number and ratings.

In Figure 42 a first scheme of the complete poloidal circuit of proposed configuration for RFX-mod2 is depicted. In the scheme the additional switches and the modified transfer resistors are reported with generic names since, at the moment, there is not a correspondence with real components. Future studies will be addressed to investigate the complete integration of the proposed solution in the RFX-mod2 poloidal circuit.

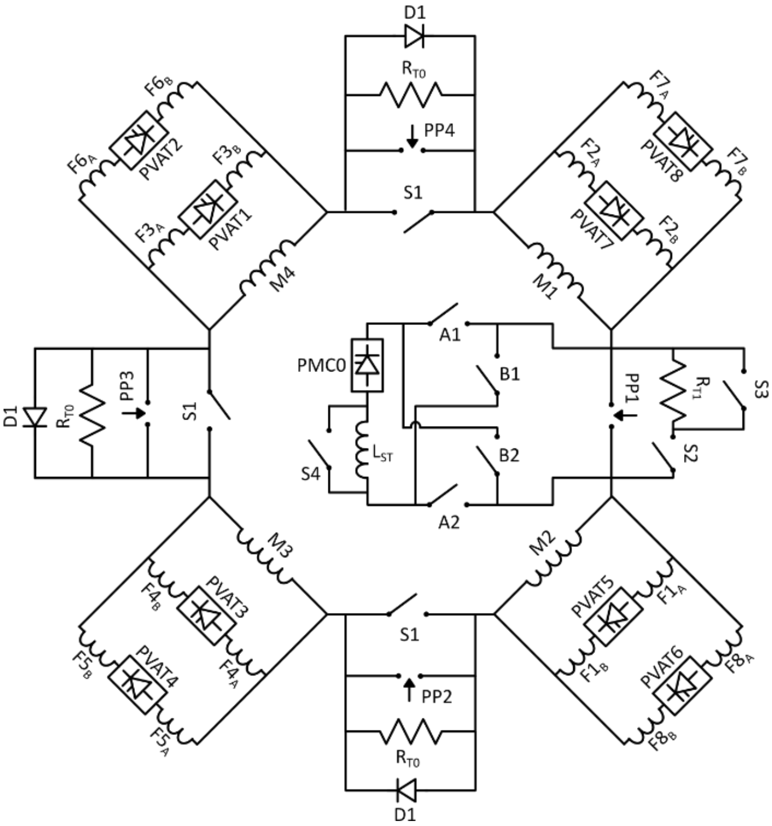

Figure 42 – Scheme of the proposed improved poloidal circuit for RFX-mod2

The equivalent T-circuit of the poloidal circuit of RFX-mod2 in the proposed configuration is reported in Figure 43. It is derived from the equivalent simplified poloidal circuit of RFX-mod reported in the previous section (Figure 33) and on the complete scheme of Figure 42.

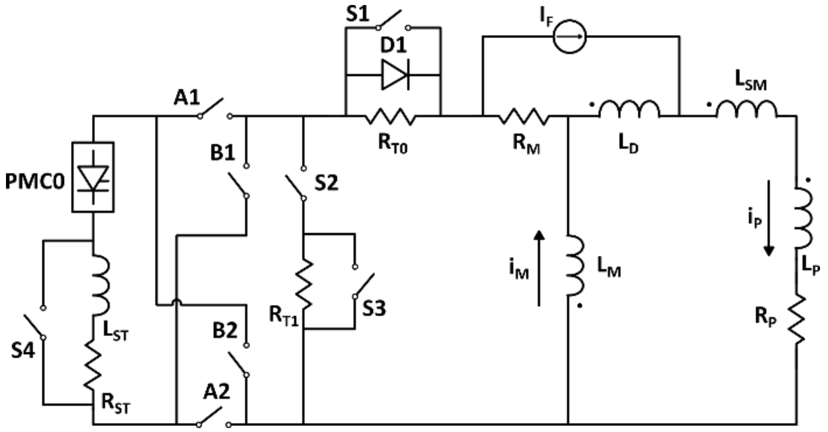

Figure 43 – Simplified equivalent circuit of proposed RFX-mod2 poloidal circuit.

L_{ST} and R_{ST} are the inductance and the resistance of the inductor used as additional magnetic energy reservoir and are assumed of 100 mH and 15 mΩ respectively, obtaining a time constant long enough for the scope. The inductance value is of the order of that of the magnetizing winding, while the resistance value is 50% lower; this could be reached in principle providing cooling with nitrogen gas at a temperature around 90 K to the inductor, thus decreasing the copper resistivity to around 15% of its room temperature value.

Ten converter units (type A) compose the converter PMC0, reported in Figure 44, that performs the two functions: the pre-magnetization and the plasma current sustainment. This solution allows to overcome the limits coming from the splitting of the two functions between PMAT and PCATs. The inversion of the current polarity shall be managed with additional switches indicated with A1, A2, B1, B2 in the circuit. Only two type A units are used in the toroidal winding PS system.

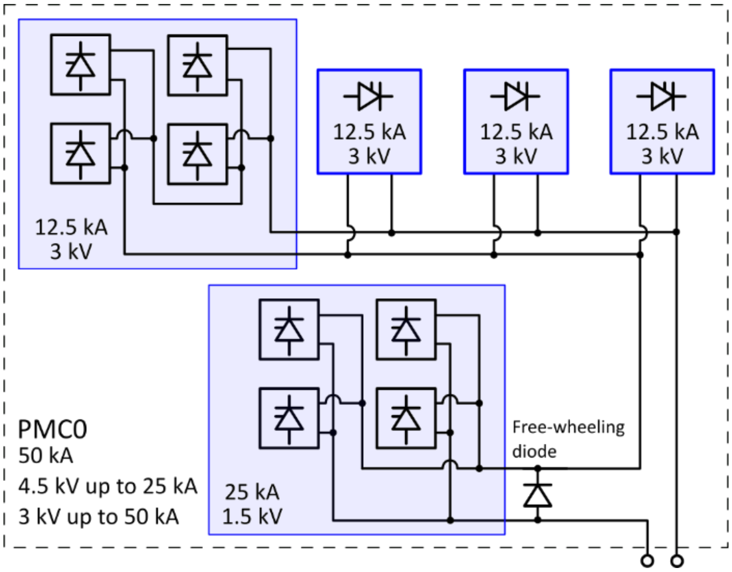

Figure 44 – PMC0 converter configuration

The electrodynamic forces that arise on the F-coils during a plasma pulse are proportional to the product between the value of the current circulating in the F-coils and the plasma current. The F-coils has been designed considering a plasma current of 2 MA, according to the original design requirements of the experiment. To keep the mechanical shear stress of the F-coils within the design limit, reaching a plasma current of about 2.5 MA, the total magnetomotive force in the F-coils is limited to 1.5 MAt, maintaining the current distribution on the eight F-coils to assure the plasma equilibrium.

A current generator I_F is added to the simplified circuit in order to take into account the partial non-compensation of the plasma magnetomotive force for plasma current above 1.5 MA. It is underlined that I_F is not a real component to be installed in the circuit, it is a modelling strategy to take into account the contribution of the additional leakage inductance (L_D), resulting from the non-compensation of the plasma ampere-turns, only when the plasma current rises above 1.5 MA. In fact, I_F accounts for a current equal to $i_P/200$ up to a value of 7.5 kA, equivalent to 1.5 MA on the plasma side, and then remains constant to 7.5 kA when i_P rises above 1.5 MA. With this modelling strategy, the leakage inductance has a current different from zero only when the plasma current goes over 1.5 MA. As happens in the RFX-mod model of Figure 33 the plasma resistance V_{RP} is implemented through a controlled voltage source that changes value as the plasma current increase.

3.1.1 Modelling and results of numerical simulations

To study the operation of the circuit of Figure 43, it has been implemented in a numerical model, and the circuit parameters of the model are reported in Table 4.

Table 4 – Circuit ratings of RFX-mod2 numerical model

L_M	58 mH	R_{T0}	1.8 Ω
R_M	20 mΩ	R_{T1}	0.6 Ω
L_{SM}	30 mH	L_{ST}	100 mH
L_P	170 mH	R_{ST}	15 mΩ
L_D	60 mH	V_{RP} (i_P<1.5 MA)	20·n V
n	200	V_{RP} (i_P>1.5 MA)	15·n V

The operational phases of the pulse in the proposed configuration and the numerical model results, with the ratings reported in Table 4, are listed below:

- Pre-magnetization: The PMC0 (Figure 44) is composed of four parallel connected strings each made by 2 type A units (50 kA/3 kV), plus another two parallel connected type A units in series (25 kA/1.5 kV) to the previous ones. This phase lasts 3.36 s and it is divided in a first phase in which the magnetizing winding is charged with a voltage of 4.5 kV up to a current of 25 kA. In the second pre-charging phase the two latter units are bypassed and the PMC0 supplies a voltage of 3 kV and the current reaches 50 kA. The switches A1, A2, S1 and S3 are kept close (the others remain open) and the PMC0 charge the magnetizing winding and the storage inductor up to 50 kA (Figure 45). This two-step pre-magnetization provides the shorter phase duration compared to use only a converter rated 50 kA/3 kV, thus reducing the losses in the magnetizing winding and storage inductor and the I^2t in the S1 vacuum switch. Figure 46 shows the RFX-mod2 upgraded poloidal circuit with additional inductor during pre-magnetization phase.

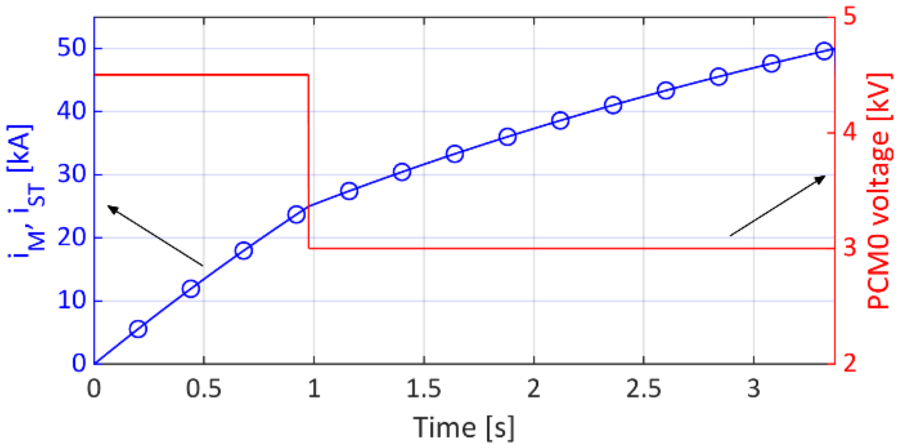

Figure 45 – i_M and i_{ST} and PMC0 voltage during the pre-charging phase

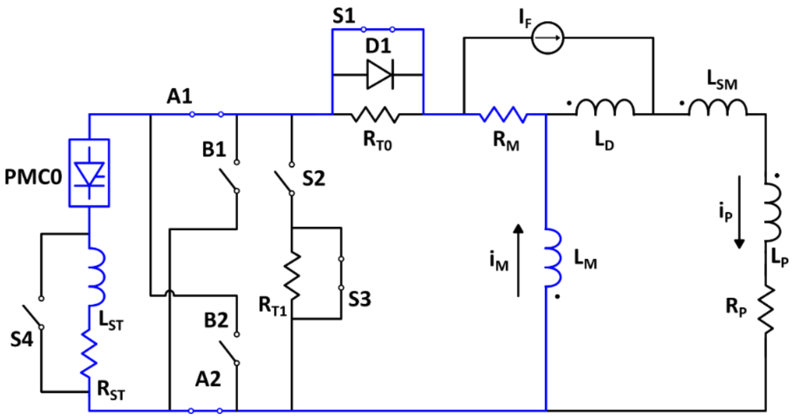

Figure 46 - Simplified equivalent circuit of the proposed RFX-mod2 poloidal circuit with additional inductor during pre-magnetization phase.

- Plasma current initiation and first ramp-up: At the beginning of this phase the S2 is closed and the transfer resistor R_{T0}=1.8 Ω is inserted in the circuit by opening the switch S1 (see Figure 47): the abrupt decrease of the magnetizing winding current and the consequent magnetizing flux swing provides the plasma current initiation and its ramp-up (Figure 48). In this phase, which lasts about 60 ms, the plasma current rises to about 1.8 MA and the magnetizing current decreases from 50 kA to about 14 kA. The voltage drop on the plasma resistance is considered 4 kV (20 V on the plasma side) with the plasma current under 1.5 MA and 3 kV (15 V on the plasma side) with i_P above 1.5 MA.

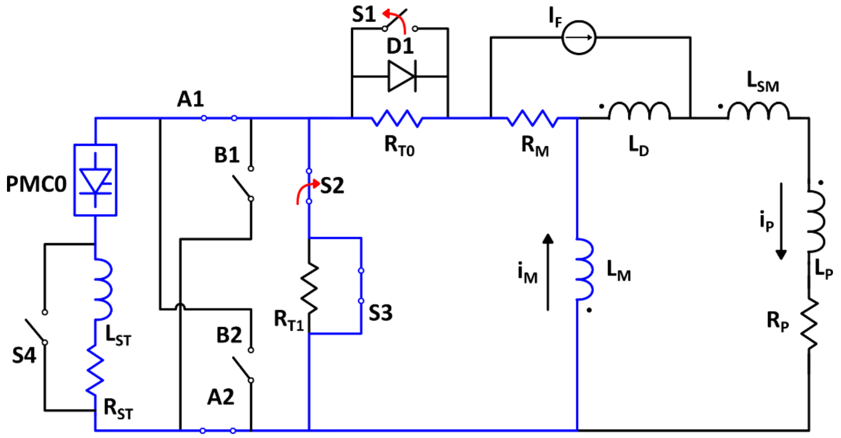

Figure 47 - Simplified equivalent circuit of the proposed RFX-mod2 poloidal circuit with additional inductor during plasma current initiation and first ramp-up.

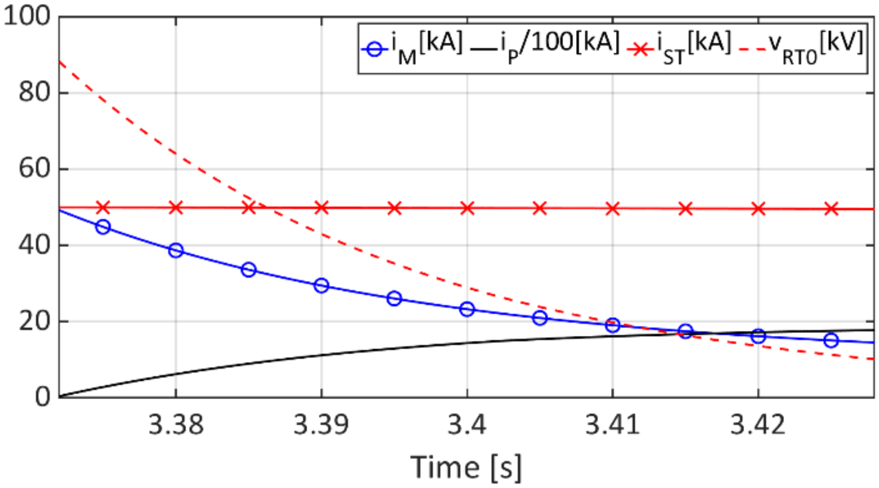

Figure 48 – Main current and voltage waveforms of the numerical simulation during the first ramp-up phase.

- Insertion of the additional storage inductor: as can be seen in Figure 47, in the last part of the previous phase the PCM0 is switched off leading the current to flow in the FW diodes, and thus the additional inductor is short-circuited via S2 and S3; immediately after B1 and B2 are closed followed by the opening of A1, A2 (Figure 49). With the opening of S3 and the insertion of the transfer resistor R_{T1}=0.6 Ω, also the additional storage inductor is inserted in the circuit and a fraction of the energy stored during the pre-magnetization phase is transferred from L_{ST} to the magnetizing winding and thus to the plasma. From the numerical simulation the energy stored in L_{ST} decays from about 125 MJ to 57 MJ and on the transfer resistor R_{T1} is applied a voltage between 22 kV and 4.3 kV (loop voltage from 110 V to 21.5 V on the plasma side). At the end of the phase, which lasts 140 ms, the plasma current reaches 2.6 MA and the current in the magnetizing winding falls to about -10 kA. When i_M changes polarity R_{T0} is short-circuited by the diode D1 since it no longer contributes to the decrease of i_M. Figure 50 shows the results of the numerical simulation during this phase.

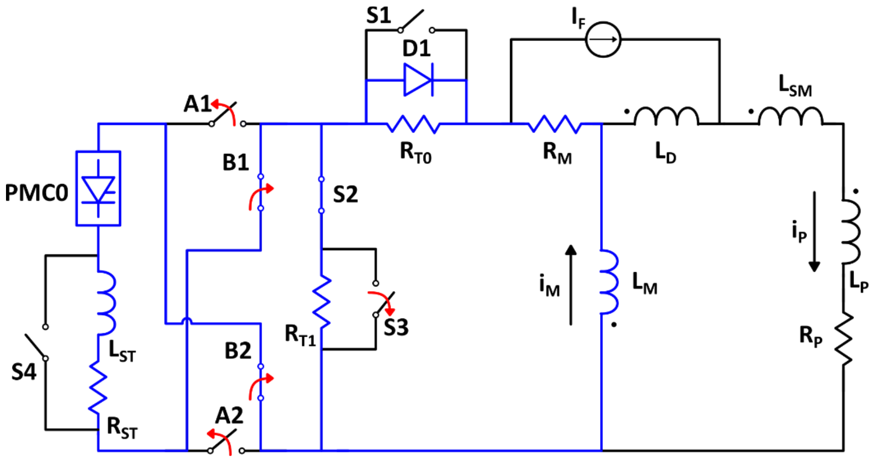

Figure 49 - Simplified equivalent circuit of proposed RFX-mod2 poloidal circuit with additional inductor during the insertion of additional storage inductor.

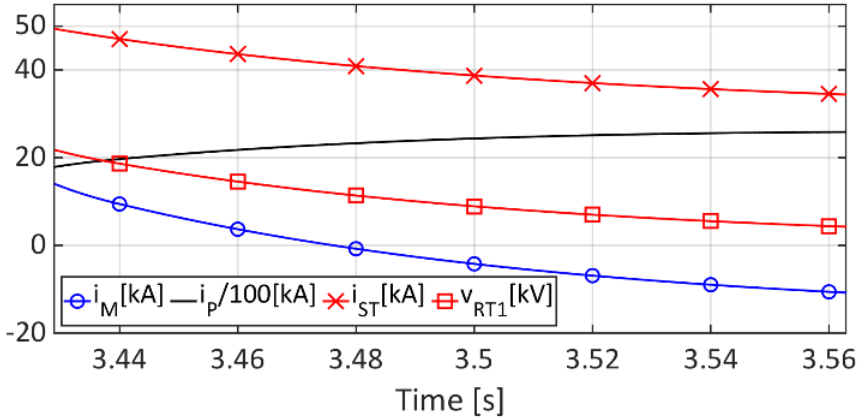

Figure 50 – Main current waveforms of the numerical simulation during the insertion of the additional inductor.

- Plasma current flat-top: In this phase the plasma current is sustained by the converter PMC0 which can apply up to 3 kV to the transfer resistor R_{T1}. L_{ST} is short-circuited by the closed switch S4. PMC0 can sustain the plasma current as long as its current reaches the value of 50 kA and in the simplified model the flat-top phase can last approximately 400 ms. The voltage drop on the plasma resistance is considered 2.7 kV (13.5 V on the plasma side) during this phase.

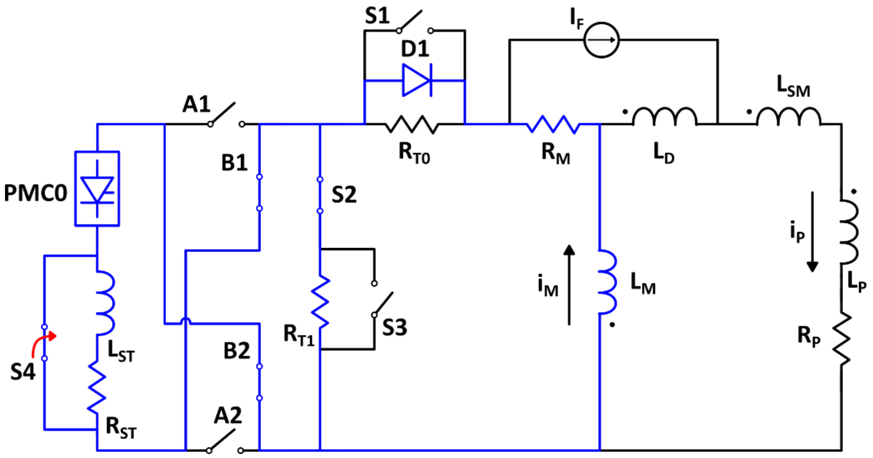

Figure 51 - Simplified equivalent circuit of proposed RFX-mod2 poloidal circuit with additional inductor during the flat-top phase.

The results of RFX-mod2 model are reported in Figure 52 for the plasma current ramp-up and flat-top.

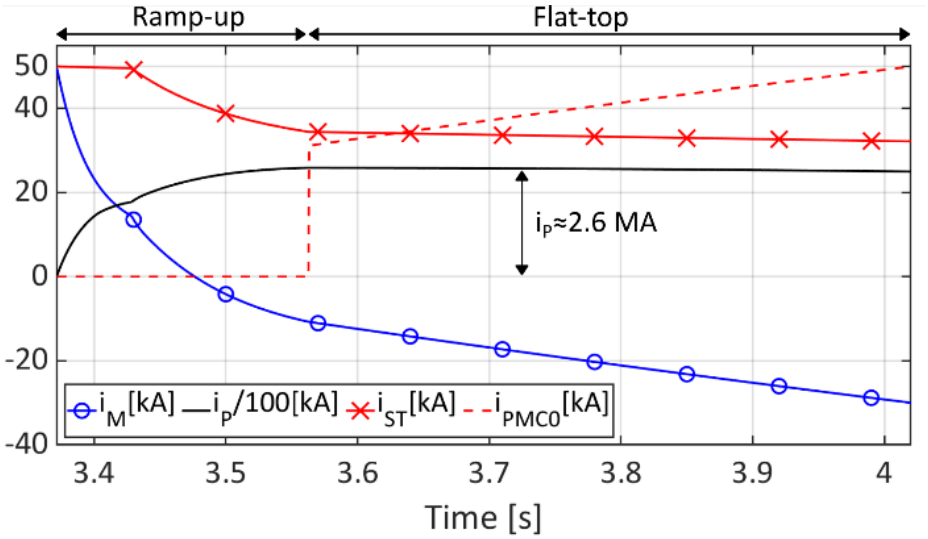

Figure 52 – Main current waveforms of RFX-mod2 numerical simulation during plasma current ramp-up and flat-top.

The first results suggest that with an additional inductor a plasma current over to 2.5 MA could be reached with a flat-top duration of several hundreds of milliseconds. The key driver of the design is remaining in the design limits of the present converters and main transformers, achieving a limited impact on the present PS system and the 400 kV grid.

The feasibility studies of the proposed modifications shall be accompanied by a full revision of the fault analysis, considering the new operational scenarios and circuit topology. The protection systems will need to be adapted to the new machine configuration and it will be fundamental also a revision of the F-coils control to manage the plasma position while the compensation of the magnetomotive force saturates at 1.5 MA.

3.2 Electrostatic energy storage solution

This section presents an alternative reconfiguration of the poloidal power supply system of RFX-mod2 based on a combined resistor-capacitor energy transfer system. This system allows to store energy in capacitor banks during the first phase of the plasma current ramp-up and release it to the plasma when the magnetizing current changes polarity, driving the plasma current over 2.5 MA. The proposed poloidal circuit modifications are again conceived with the aim to maintain the present thyristor converters number and rating and to remain within the power limits of the main transformers.

In Figure 53 is depicted a complete scheme of the proposed enhanced poloidal circuit configuration. In the figure can be seen the four capacitor banks (highlighted in red), with a capacitance of 200 mF and a rated voltage of 5.25 kV each, series-connected with the transfer resistors R_T. These values for the capacitor banks has been derived from numerical simulation results reported in section 3.2.1. With this configuration, the capacitor banks store energy during the first part of the plasma current ramp-up, increasing their voltage up to about 4.3 kV. In the second part of the plasma current ramp-up the energy previously stored is released sustaining the decrease of the magnetizing current, and therefore, inducing a loop voltage on the plasma sufficient to drive the plasma current over 2.5 MA.

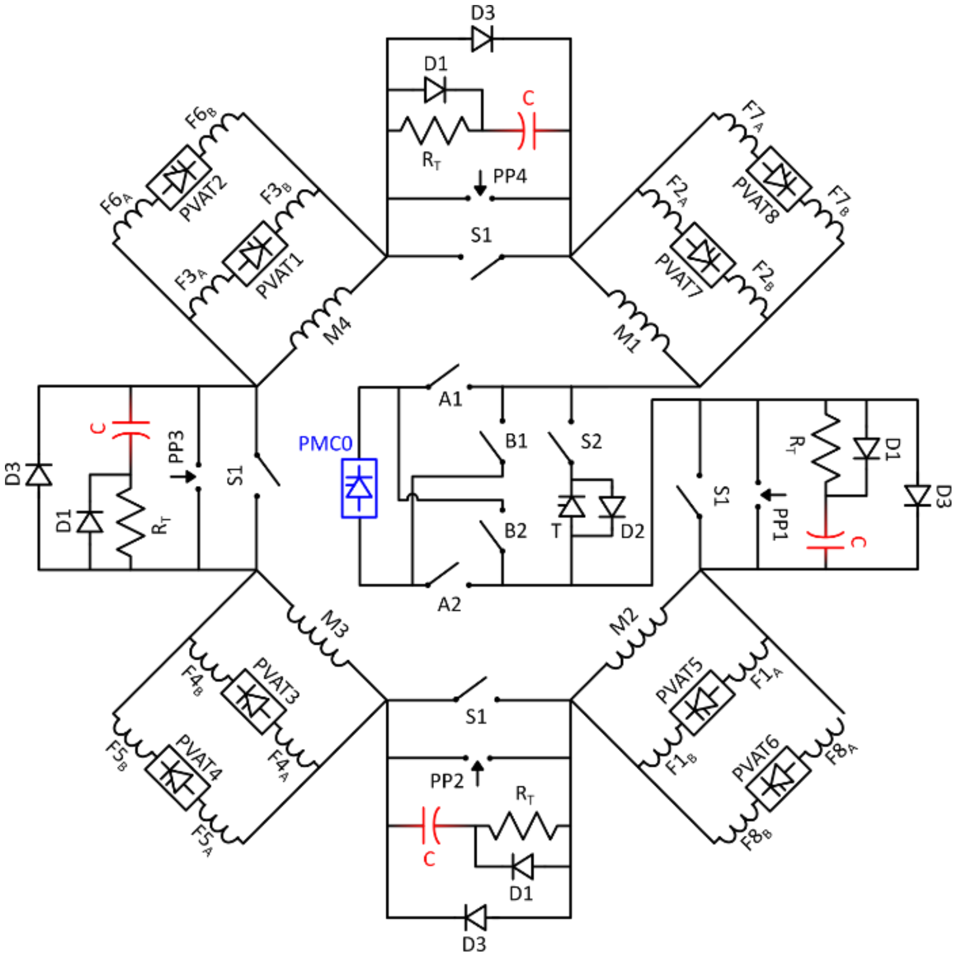

Figure 53 – Scheme of the improved configuration proposed for RFX-mod2

In Figure 54 the equivalent T-circuit of the poloidal circuit is reported. It is derived from the complete scheme in Figure 53, collapsing the four series connected sectors in one.

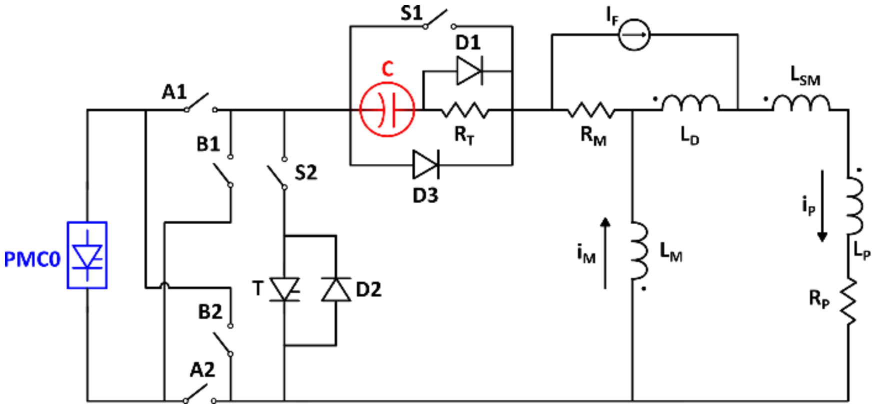

Figure 54 – Simplified equivalent circuit of the proposed upgrade of the RFX-mod2 poloidal circuit

Through a reconfiguration of the type-A converter units, the PMC0 converter is obtained. Ten converter units are connected as shown in Figure 55: four parallel connected strings, each made of 2 type-A units (50 kA/3 kV), are connected in series with two parallel-connected type A units (32.5 kA/1.5 kV). With this configuration, the PMC0 performs the pre-charging function of the magnetizing winding, the ramp-up and sustainment of the plasma current as reported in the next section.

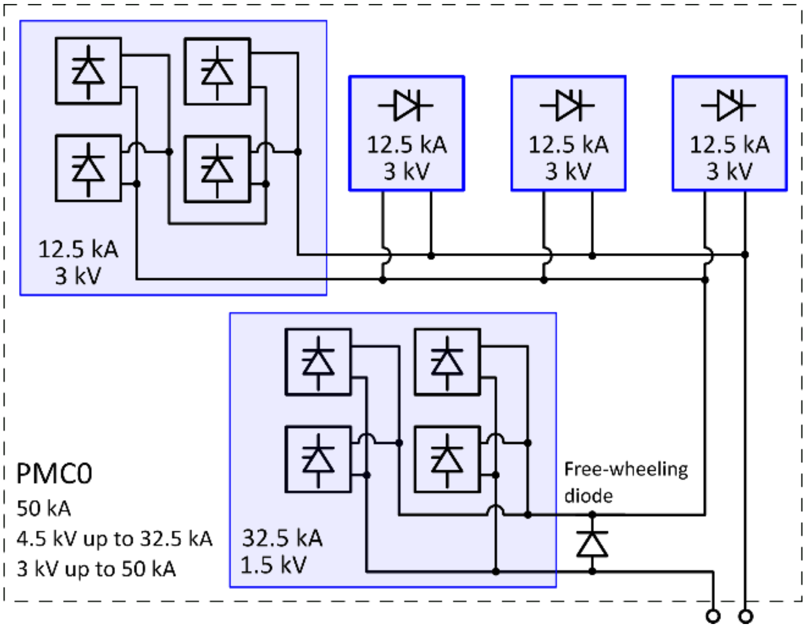

Figure 55 – Proposed configuration for the PMC0

Also in this model the non-compensation of the plasma magnetomotive force over 1.5 MA is considered, to keep the mechanical stress of the F-coils within the design limit. The current generator I_F is added in the plasma branch of the circuit and the additional equivalent inductance arising from the saturation of the magnetomotive force compensation is considered in the model with the leakage inductance L_D. I_F generates a current equal to $i_P/200$ up to a value of 7.5 kA (equivalent to 1.5 MA on the plasma side) and then supplies a current of 7.5 kA when the plasma current rises over 1.5 MA. With this modelling strategy, the leakage inductance has a current different from zero only when the plasma current goes over 1.5 MA.

3.2.1 Numerical results

The operation of the circuit presented in Figure 54 has been studied developing a numerical model with the parameters reported in Table 5.

Table 5 – Parameters of RFX-mod2 poloidal circuit numerical model

L_M	58 mH	**n**	200
R_M	20 mΩ	R_T	2 Ω
L_{SM}	30 mH	**C**	50 mF
L_P	170 mH	V_{RP} (i_P<1.5 MA)	20·n V
L_D	60 mH	V_{RP} (i_P>1.5 MA)	13·n V

- Pre-magnetization: During this first phase the switches A1, A2 and S1 are closed (the others remain open), as can be seen in Figure 56. PMC0 charge the magnetizing winding up to 50 kA applying a voltage of 3 kV (Figure 57). The two parallel-connected type A units (32.5 kA/ 1.5kV) are bypassed by the free-wheeling diode. The magnetizing winding takes about 1.19 s to be pre-charged, storing an energy of 72 MJ with a magnetizing flux of 15 Wb.

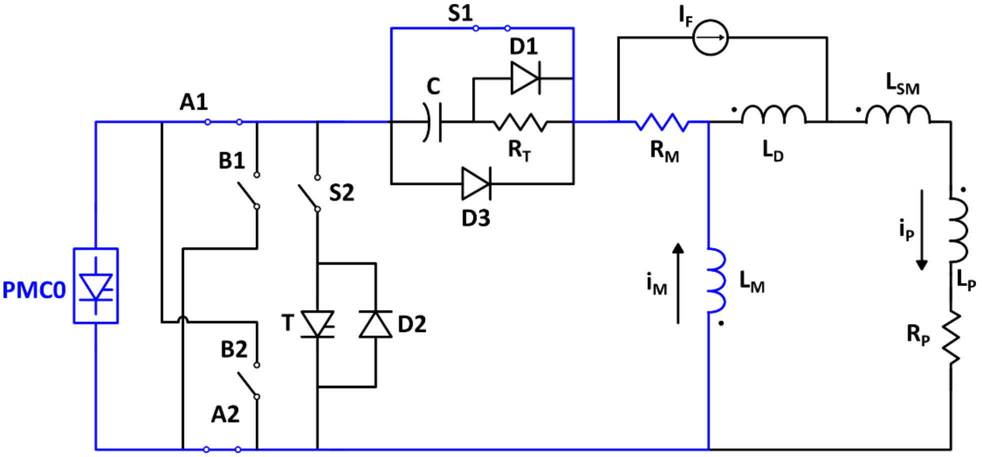

Figure 56 - Simplified equivalent circuit of proposed RFX-mod2 poloidal circuit with additional capacitor bank during the pre-magnetization phase

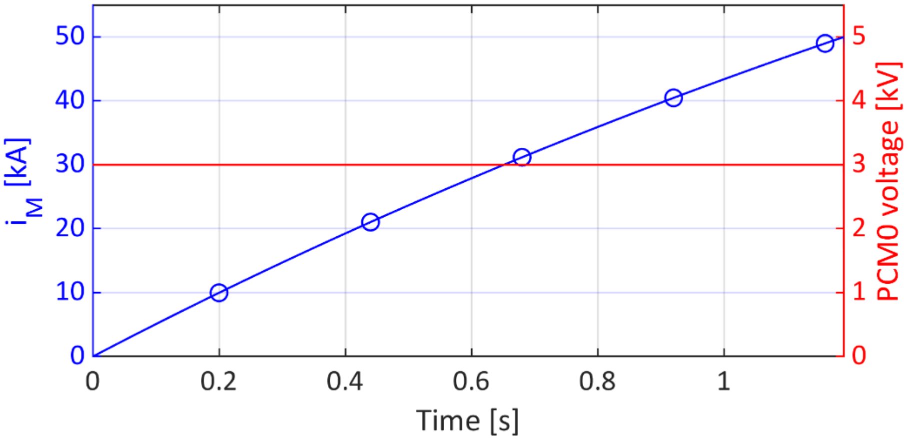

Figure 57 - Magnetizing current (i_M) and PCM0 voltage during the first ramp-up phase

- Plasma current initiation and first ramp-up: after the PMC0 switch-off, S2 is closed and T is switched on. The plasma pulse starts when the transfer resistor R_T is inserted in the circuit by opening S1. The voltage that rises across R_T, and therefore across the magnetizing winding, leads to an abrupt decrease of the magnetizing current. The consequent magnetizing flux swing provides a toroidal loop voltage in the gas inside the toroidal support structure sufficient for the plasma current initiation and ramp-up. During this phase, that lasts about 50 ms, the plasma current reaches 2 MA and the magnetizing current decreases from 50 kA to 10 kA (Figure 58).

The resistive voltage drop of the plasma is considered equal to 4 kV (20 V on the plasma side) up to a current of 1.5 MA and then 2.6 kV (13 V on the plasma side). Since the capacitor bank C is connected in series with the transfer resistor R_T, while the capacitor current i_C is positive, its voltage v_C increases up to 17.1 kV (Figure 59). The energy stored in the capacitor bank in this phase is about 7.3 MJ. Meanwhile, B1 and B2 are closed and then A1 and A2 are opened changing the polarity of the converter PCM0 with respect the poloidal circuit. Figure 60 shows the simplified equivalent circuit of proposed RFX-mod2 poloidal circuit with additional capacitor bank during the first ramp-up phase.

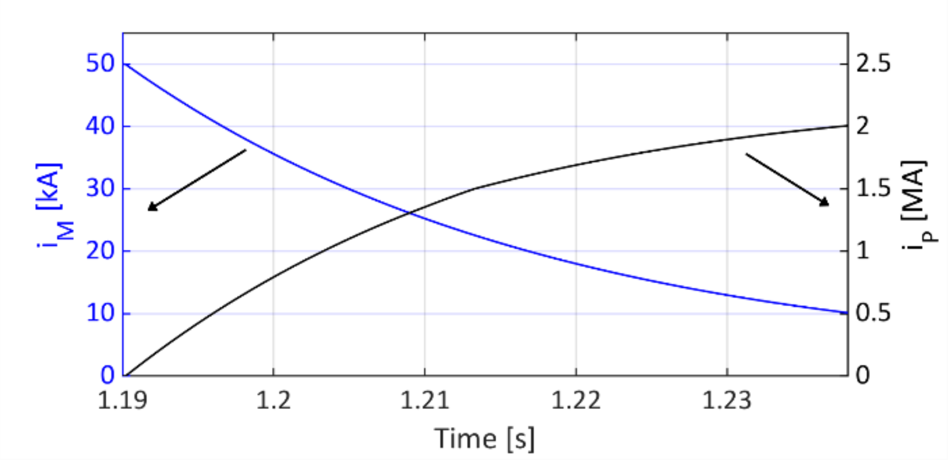

Figure 58 – Magnetizing current (i_M) and plasma current (i_P) during the first ramp-up phase

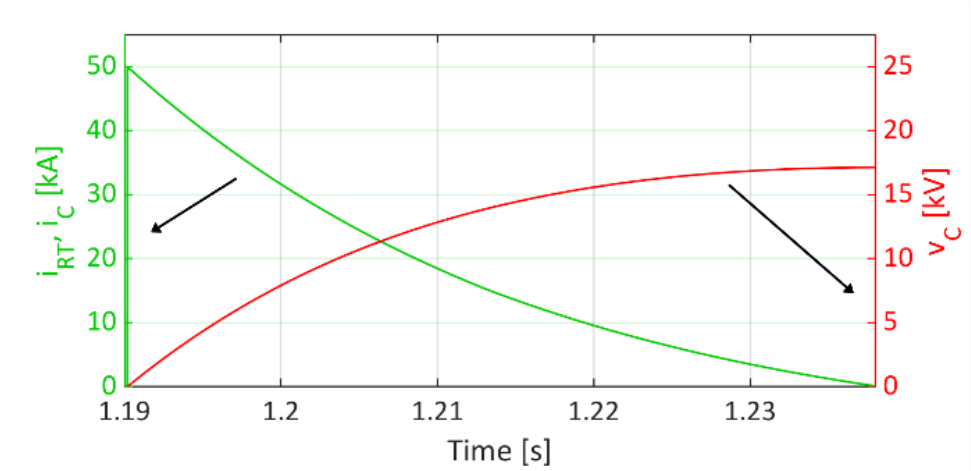

Figure 59 – Capacitor bank current (i_C) and voltage (v_C) during the first ramp-up phase of the plasma current

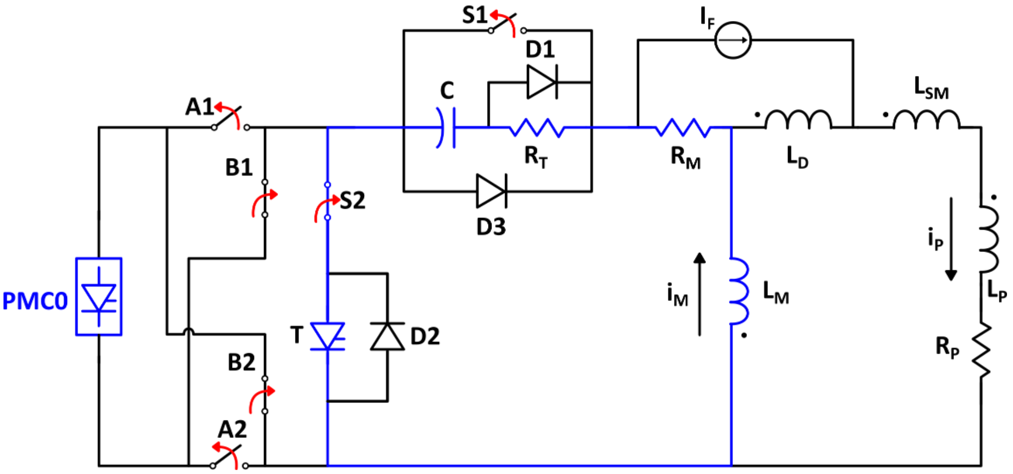

Figure 60 - Simplified equivalent circuit of proposed RFX-mod2 poloidal circuit with additional capacitor bank during the first ramp-up phase

- Transfer of energy stored in C: as can be seen in Figure 61, when the capacitor current change polarity, the diode D1 start conducting. In this way, the transfer resistor R_T is excluded from the circuit since it does not contribute anymore to the magnetizing current decrease. When the magnetizing current crosses the 0 A, the thyristor T is switched off and D2 start conducting. After some milliseconds the PMC0 starts to supply 4.5 kV and D2 stops conducting since it is reverse-biased. The decrease of the magnetizing current is sustained by the voltage applied by the converter PMC0 but also from the voltage of the capacitor bank C. Thus the previously stored energy in C it is transferred back to the magnetizing winding and to the plasma. In this second ramp-up phase the plasma current reaches 2.7 MA (Figure 62) in about 70 ms and the capacitor bank voltage returns to 0 V (Figure 63).

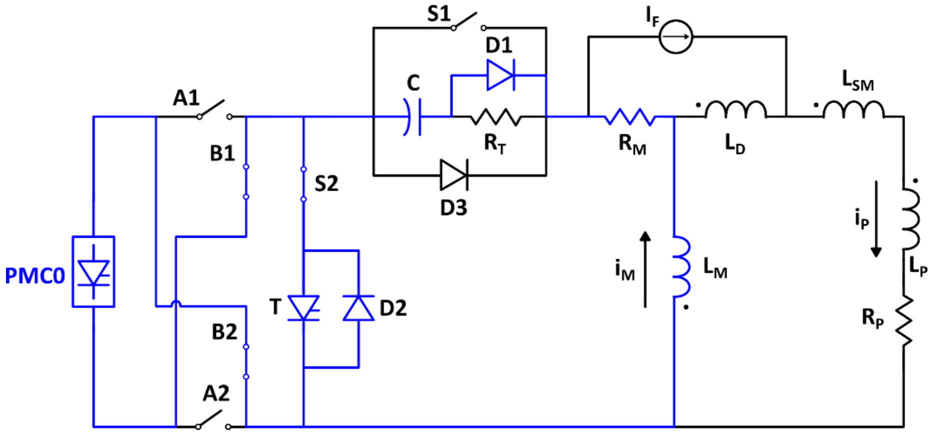

Figure 61 - Simplified equivalent circuit of proposed RFX-mod2 poloidal circuit with additional capacitor bank during the second ramp-up phase

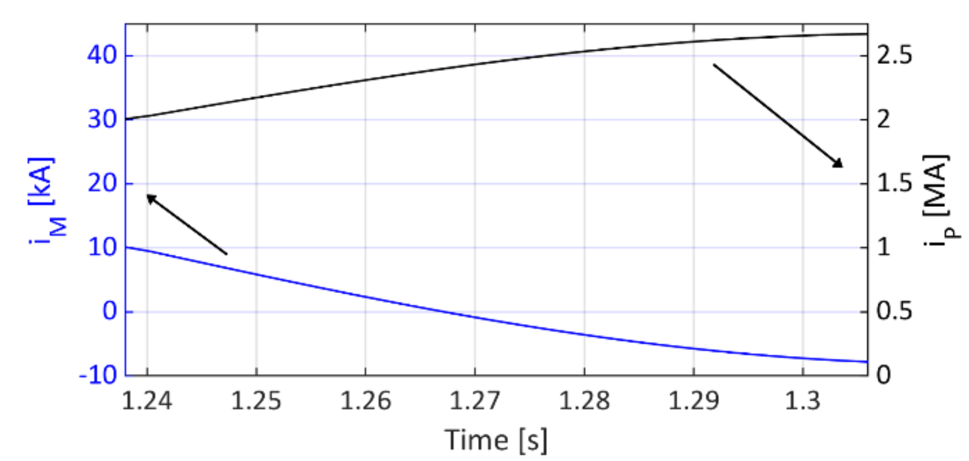

Figure 62 – Magnetizing current (i_M) and plasma current (i_P) during the second ramp-up phase

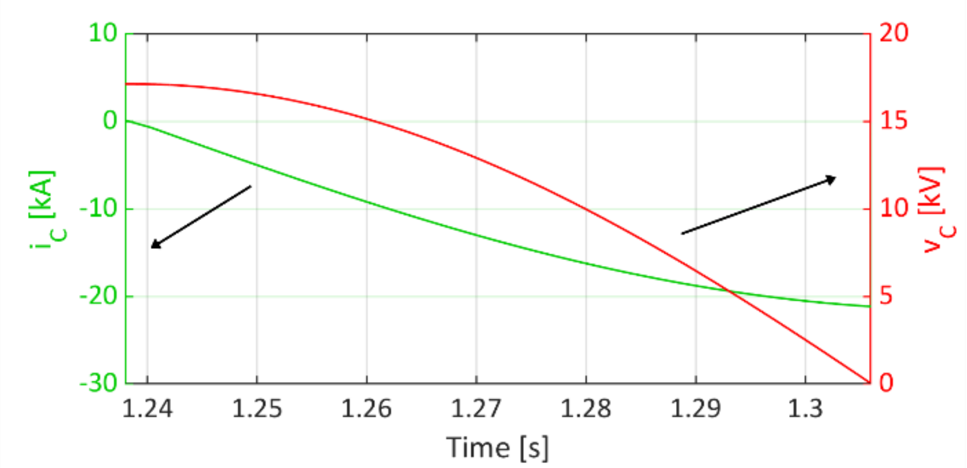

Figure 63 – Capacitor bank current (i_C) and capacitor bank voltage (v_C) during the second ramp-up phase

- Plasma current flat-top: the plasma current is sustained by PMC0 which can apply 4.5 kV up to 32.5 kA and 3 kV above. C is short-circuited by the diode D3 when capacitor voltage reaches 0 V (Figure 64). PMC0 sustains the plasma current as long as its current (i_{PMC0}) doesn't reach the value of 50 kA. The magnetizing current reaches -35 kA, thus achieving the double swing of the magnetizing flux. In the numerical simulations of the simplified model, the flat-top phase can last more than 500 ms. Figure 65 shows the simulated plasma pulse divided in the ramp-up phases and flat-top.

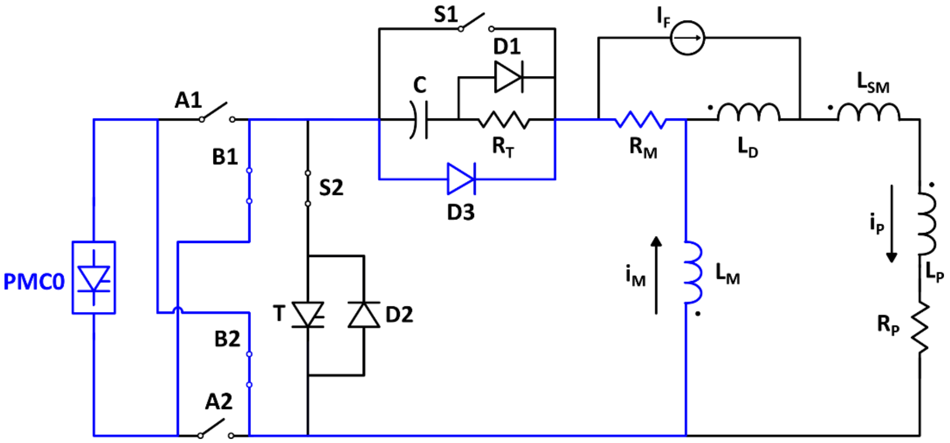

Figure 64 - Simplified equivalent circuit of proposed RFX-mod2 poloidal circuit with additional capacitor bank during the flat-top phase

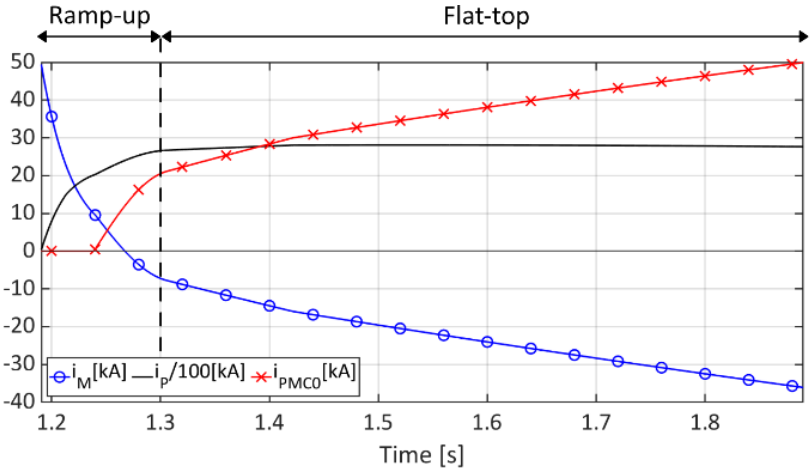

Figure 65 – Main current waveforms of the simplified model of the enhanced RFX-mod2 poloidal circuit.

In Figure 66 can be seen the voltage applied to the magnetizing winding (V_{TOT}) during the two ramp-up phases and the flat-top. The use of the combined resistor-capacitor energy transfer system leads to a voltage over 20 kV applied on the magnetizing winding also when the transfer resistor is excluded from the circuit.

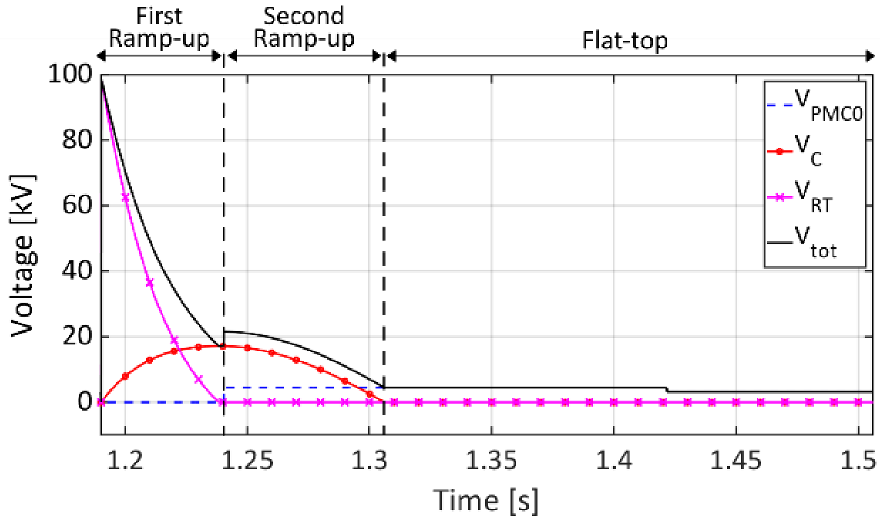

Figure 66 - Voltage applied to the 4 sectors of the magnetizing winding (V_{TOT}) during the plasma pulse and the separates contributes from C, R_T and PMC0

The first analyses show that using four capacitor banks to store about 7 MJ in the first part of the plasma ramp-up to be released when the current on the transfer resistors changes polarity, the plasma current can be increased over 2.5 MA with a flat-top duration of several hundred of ms.

3.2.2 Considerations about the capacitor banks requirements and comparison with magnetic storage solution

The capacitor banks requirements derive from the numerical simulations. In Figure 67 are reported the capacitor bank currents (i_C) and voltages (v_C) with and without plasma. A pulse without the plasma breakdown is a quite rare event but it has been taken into account since it leads to a higher voltage on the capacitor bank. From the numerical model of the simplified circuit in Figure 54 the maximum voltage on the capacitor bank is 20.7 kV. Since C in the simplified equivalent circuit comprises four series-connected capacitor banks in the real poloidal circuit, each capacitor bank has the following ratings:

- Capacitance: 200 mF
- Nominal voltage: 5.25 kV
- Maximum peak current: 50 kA
- Maximum repetition rate: once every 600 s
- Maximum energy: 2.7 MJ

In addition, in this application, there is no voltage reversal, and the derivative of the capacitor banks voltage is relatively slow (in the order of 80 kV/s). Considering to use metalized film capacitor, that has high energy density for its self-healing characteristic and is often used in pulsed power applications, a reasonable volumetric energy density for a similar application is 1 MJ/m^3. This volumetric energy density has to be lowered by a factor of 4 to take into account the space between the single capacitors, busbars and support structure. Under these assumptions, the volume of each capacitor banks should be around 10 m^3, which is compatible with the available space in RFX-mod2 power supply hall (Figure 20).

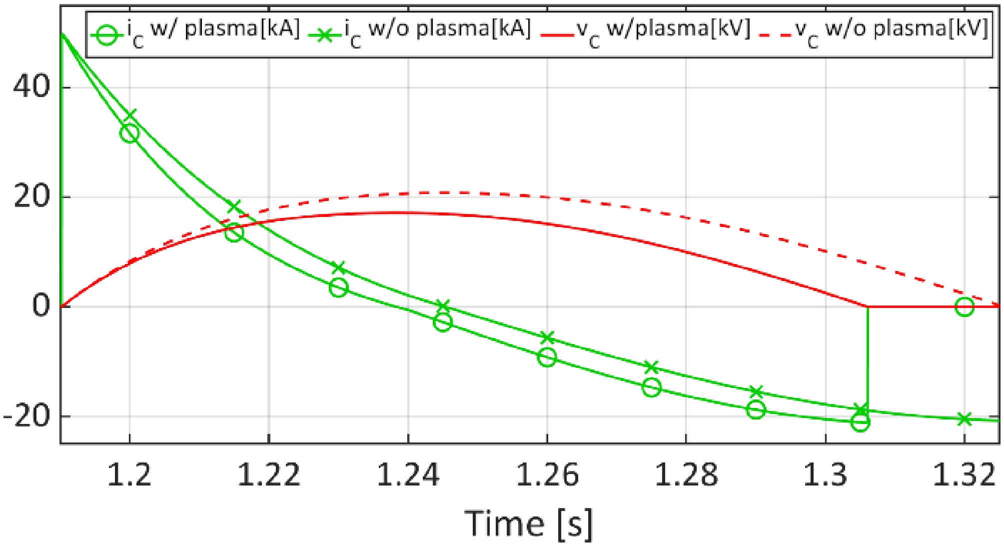

Figure 67 – Capacitor bank currents (i_C) and voltages (v_C) with and without plasma.

In 3.1 an alternative solution that relies on the use of an additional inductor has been presented. The inductor stores about 125 MJ of energy before the plasma pulse and releases part of this energy to the plasma during the ramp-up phase. The main drawback of this solution with respect electrostatic one is that the energy stored is at least one order of magnitude higher. In addition only a part of energy is transferred from the additional inductor to the magnetizing winding, using a transfer resistor and therefore with dissipation of energy. In the solution using the combined capacitor-resistor energy transfer system, all the energy is transferred from the capacitor banks to the magnetizing winding and without dissipate part of it on a transfer resistor.

Further studies will be addressed to assess the applicability of this application to RFX-mod2, considering all the operating conditions. The protection systems will need to be adapted to the new machine configuration and it will be fundamental also a revision of the F-coils control to manage the plasma position while the compensation of the magnetomotive force saturates at 1.5 MA.

4 MEST

The main SC coils of the majority of existing fusion experiments are supplied by thyristor-based converters. The MEST system is a newly developed scheme to supply the SC coils, resulting in a partial or total degree of decoupling between the grid and the magnets coupled with the plasma, which means that the grid does not have to instantly provide the power delivered to the SC coil and the plasma. The MEST would take place of thyristor-based converters and would be used as ESS, only requiring power from the grid to make up for losses and sustain the plasma against resistive dissipation, with a slower dynamic than the one required by a system without ESS.

Figure 68 depicts the MEST circuit, already studied in [14] and [15]. The Load Coil (LC) is the SC coil to be supplied and the sinK Coil (KC) is an additional SC coil that acts as an energy reservoir. The energy transfer system of the MEST is composed of four equivalent switches (S1÷S4), each comprising fully controllable semiconductor switches (like IGCTs or IGBTs) with all the appropriate devices for their operation (series connected diodes if the component is asymmetric, snubbers and clamp circuits) and a capacitor bank (C). Thanks to this energy transfer system the energy is transferred between LC and KC with a unitary efficiency, except for the circuit losses. The energy transfer system can control the LC voltage only if KC current (i_{KC}) is greater than the absolute value of LC current (i_{LC}), this condition will be explained and justified in section 4.1.1.1.

To meet this requirement, a power supply (PS) must deliver the initial energy to the KC, to make up for circuit losses and to provide the power to be transferred to the plasma, magnetically coupled to LC, for its ignition, sustainment and control.

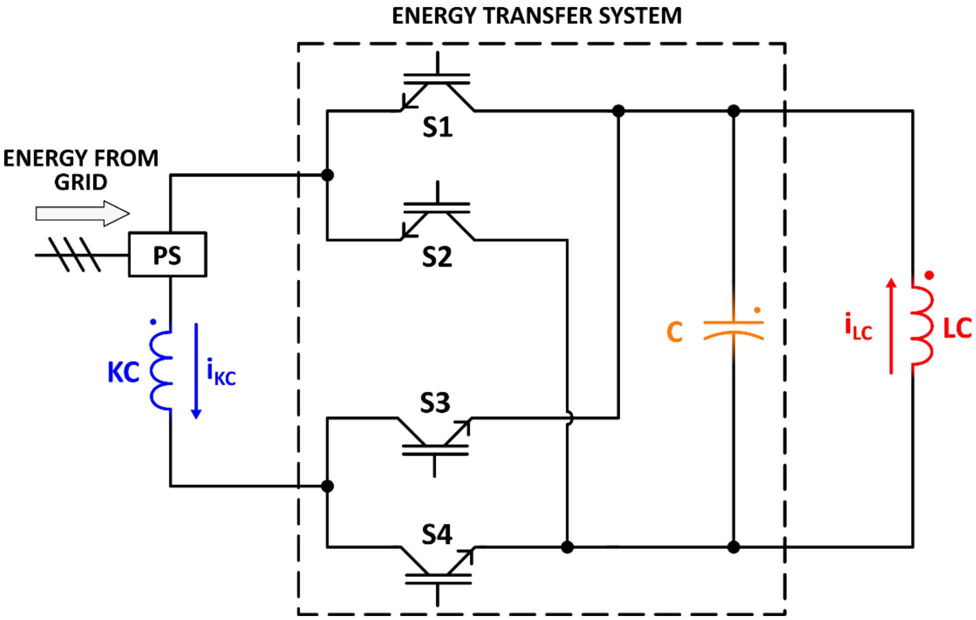

Figure 68 - MEST principle scheme

The energy transfer between the two SC coils is performed by controlling the voltage of C, thus the voltage across LC, applying a proper switching pattern of the four equivalent switches (S1÷S4), following a hysteresis logic, as explained in section 4.1.1.1 and section 4.1.1.2.

The capacitor bank is only needed to achieve the energy transfer between LC and KC and not to store energy in the system. With this approach, C is designed to be as small as possible in accordance with the switching frequency. As is explained in section 4.2, its capacitance value, along with the amplitude of the hysteresis band, is inversely proportional to the switching frequency of the four switches; in particular, the reduction of C capacitance implies a higher switching frequency, for a given switching pattern. A higher switching frequency implies higher commutation losses and therefore a higher number of components to be used for each equivalent switch.

In sections 4.1.1 and 4.1.2 the control strategy to control LC current (i_{LC}) and KC current (i_{KC}) with two decoupled control loops is proposed.

The complete decoupling between the grid and LC coupled to the plasma means that all the magnetic energy variations on LC and the plasma are invisible to the grid that has to supply only the dissipated energy. In large fusion experiments equipped with SC coils the dissipated power is much lower compared to the power required for the magnetic energy variation (i.e. magnetic flux variation) as can be seen from the application study in 4.4. If a complete decoupling between grid and LC coupled with the plasma is considered, KC has to be pre-charged with at least double the maximum energy stored by LC, the capacitor bank and the plasma during the pulse. With this approach, the PS can be rated only to compensate for the energy losses.

4.1 MEST control system

The logic underlying the control system proposed in this section is to use the PS to control i_{KC} while the energy transfer system (consisting of C and S1÷S4) controls i_{LC} through the modulation of the capacitor voltage (v_C). In this way, the decoupling between i_{LC} control and i_{KC} control is achieved. In Figure 69 the block diagram of the MEST control system is reported.

4.1.1 Load Coil current (i_{LC}) control strategy

The variable to be controlled is the load current (i_{LC}), thus the main reference signal is the desired load current ($i_{LC,ref}$). The LC current control is performed by two different blocks: the “LC current control” and “Voltage hysteresis control” blocks of Figure 69.

The “LC current control” is a Proportional Integral (PI) controller that uses the measurement of i_{LC} and the reference $i_{LC,ref}$ as input to generate a reference waveform for the load voltage ($v_{C,ref}$).

In order to keep the MEST output voltage (v_C) within the hysteresis band, the “Voltage hysteresis control” takes as input $v_{C,ref}$ and modifies the topology of the MEST circuit acting on the command of the four equivalent switches (closed or open).

The different circuit topologies called states and described in 4.1.1.1, follow each other in patterns generated by the hysteresis control as described in 4.1.1.2.

During the system operation, the two nested loops continue operating to assure the desired current waveform in the load. In Figure 69 the double control loop of i_{LC} is highlighted in red.

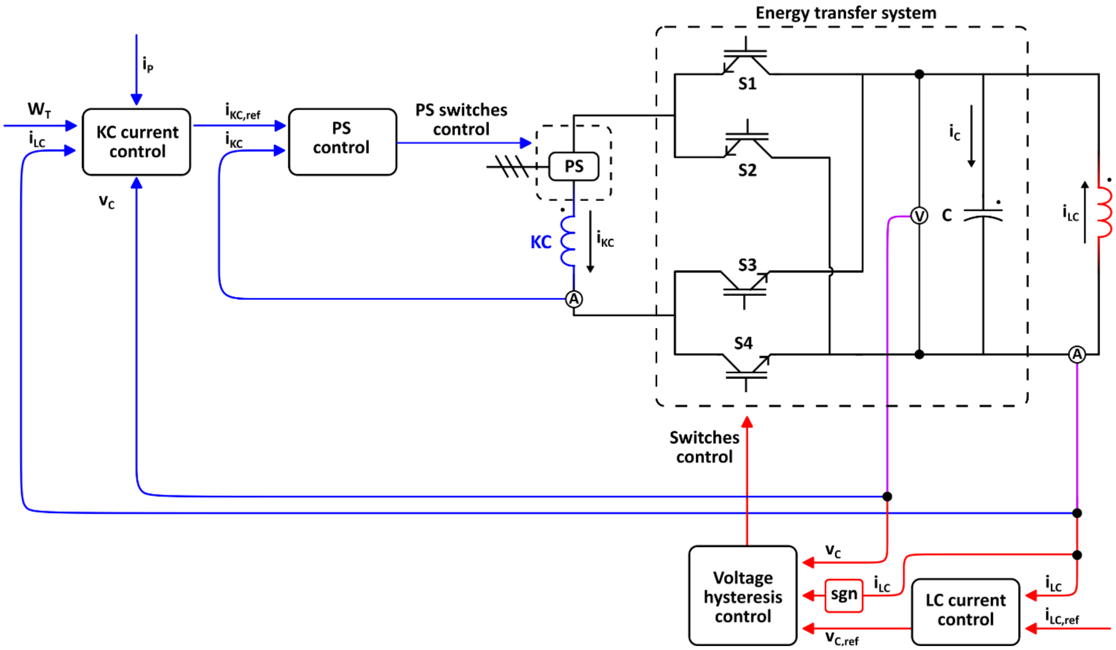

Figure 69 - Block diagram of the MEST control system

4.1.1.1 Switching states

Table 6 reports the relevant states of the MEST, where 1 indicates a closed switch and 0 is an open switch considering S1, S2, S3 and S4 as reported in Figure 68, with the time derivatives of the circuit variables.

Table 6 - Relevant states of the MEST system and trends of main variables.

State	dv_C/dt ($i_{LC}>0$)	dv_C/dt ($i_{LC}<0$)	i_C
A=[1, 0, 0, 1]	< 0	< 0 w/high derivative	$i_{KC}-i_{LC}$
B=[0, 1, 0, 1]	> 0	< 0	i_{LC}
C=[1, 0, 1, 0]	> 0	< 0	i_{LC}
D=[0, 1, 1, 0]	> 0 w/ high derivative	> 0	$i_{KC}+i_{LC}$

Table 6 shows that with $i_{LC} > 0$ there are three states to increase v_C and one to decrease v_C, while with $i_{LC} < 0$ there are three states to decrease v_C and one to increase v_C.

The most important constraint of the control is that i_{KC} must be always greater than $|i_{LC}|$ otherwise, the behaviour of the circuit expected by the control system does not occur. If this condition is not satisfied, v_C can't be decreased when i_{LC} is positive and v_C can't be increased when i_{LC} is negative.

The hysteresis control band is defined by the Lower Limit (LL) and the Upper Limit (UL), which are set above and below the reference voltage $v_{C,ref}$.

- <u>State A=[1,0,0,1] with i_{LC}>0</u>

State A is the only state that can be used to decrease v_C when i_{LC} >0, this is the reason why i_{KC} shall be always greater than $|i_{LC}|$. If $|i_{LC}| > i_{KC}$ and $i_{LC} > 0$ imposing the state A=[1,0,0,1], for Kirchhoff's current law, $i_C > 0$ so v_C increases instead of decreasing and an undamped oscillation between KC, LC and C is observed. In this state, since $i_{KC}>|i_{LC}|$, the capacitor voltage decreases from UL to LL. If v_C is positive, part of LC and C energy is transferred to KC. If v_C is negative part of KC energy is transferred both to LC and C (Figure 70).

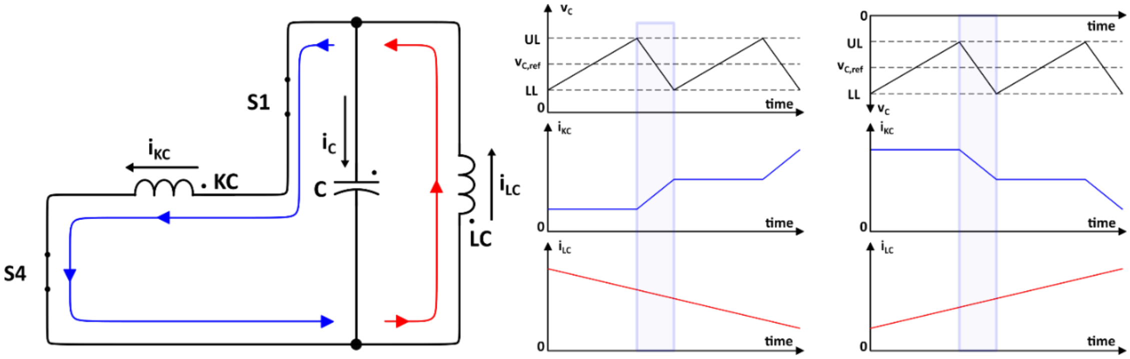

Figure 70 – State A=[1,0,0,1] with i_{LC}>0 and v_C, i_{KC} and i_{LC} trends

- <u>State B=[0,1,0,1] or C=[1,0,1,0] with i_{LC}>0</u>

These two states are equivalent and when they are applied KC is short-circuited by S1 and S3 (Figure 71) or by S2 and S4 (Figure 72). In this way, i_{KC} remains constant as the KC energy. Considering i_{LC}>0, v_C increases from LL to UL of the hysteresis band. If v_C is greater than 0 part of LC energy is transferred to C and if v_C is lower than zero part of the energy stored in C is transferred to KC.

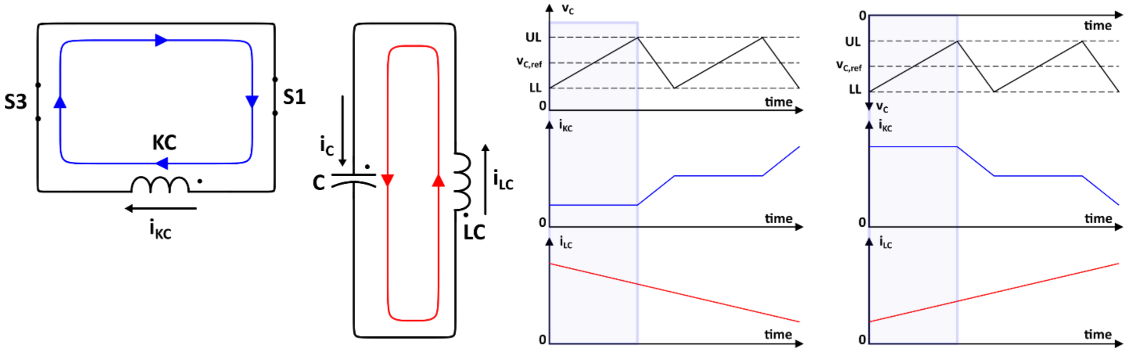

Figure 71 - State C=[1,0,1,0] with i_{LC}>0 and v_C, i_{KC} and i_{LC} trends

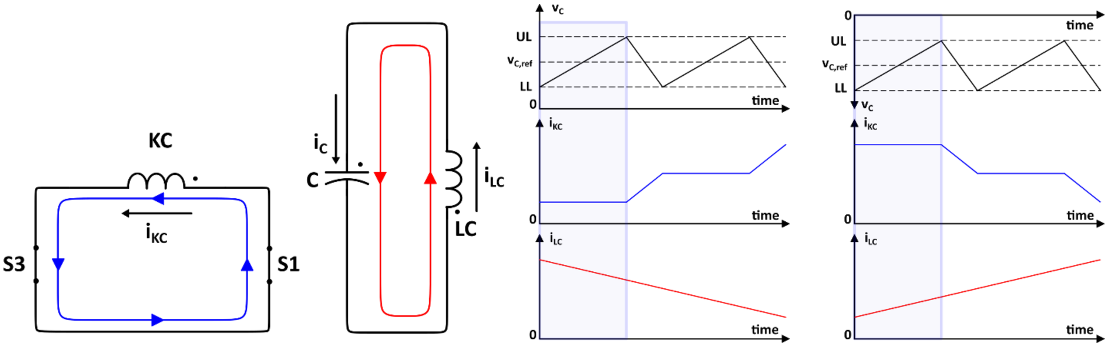

Figure 72 - State B=[0,1,0,1] with i_{LC}>0 and v_C, i_{KC} and i_{LC} trends

- <u>State D=[0,1,1,0] with i_{LC}>0</u>

With this state the current entering the capacitor is $i_C=i_{KC}+i_{LC}$ then the capacitor voltage increases from LL to UL. If v_C is positive both i_{KC} and i_{LC} decrease and part of KC and LC energy is transferred to C. If v_C is negative both i_{KC} and i_{LC} increase and part of C energy is transferred to KC and LC (Figure 73). This state is called "high derivative state" because it leads to the maximum derivative for the load voltage (i.e. C and LC voltage) and can be used when a fast variation of the load voltage is required, as explained in section 4.1.1.3. If $|i_{LC}| > i_{KC}$ and $i_{LC} < 0$ imposing the state D=[0,1,1,0], for Kirchhoff's current law, $i_C < 0$ so v_C decreases instead of increasing and an undamped oscillation between KC, LC and C is observed.

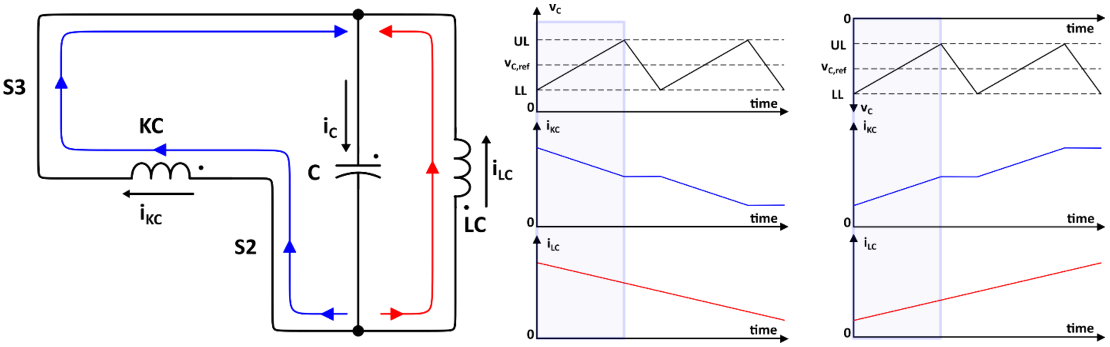

Figure 73 - State D=[0,1,1,0] with i_{LC}>0 and v_C, i_{KC} and i_{LC} trends

- <u>State A=[1,0,0,1] with i_{LC}<0</u>

With this state the current entering the capacitor is $i_C=i_{KC}-i_{LC}$ with negative i_{LC}. The capacitor voltage decreases from UL to LL with the maximum possible derivative, being this state (with i_{LC}<0) an "high derivative state". If v_C is positive, part of C energy is transferred both to LC and KC leading to an increase of i_{KC} and a decrease of i_{LC}. If v_C is negative, part of KC and LC energy is transferred to C with an increase of i_{LC} and a decrease of i_{KC} (Figure 74).

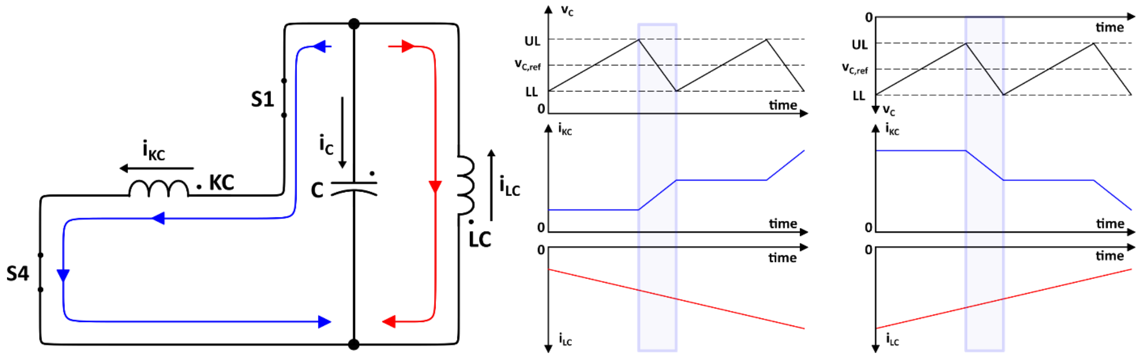

Figure 74 - State A=[1,0,0,1] with $i_{LC}<0$ and v_C, i_{KC} and i_{LC} trends

- ○ <u>State B=[0,1,0,1] or C=[1,0,1,0] with $i_{LC}<0$</u>

These two states are equivalent and when they are applied KC is short-circuited by S1 and S3 (Figure 75) or by S2 and S4 (Figure 76). In this way, i_{KC} remains constant as KC energy. Considering $i_{LC}<0$, v_C decreases from UL to LL of the hysteresis band. If v_C is greater than 0 part of LC energy is transferred to C and if v_C is lower than zero part of the energy stored in C is transferred to KC.

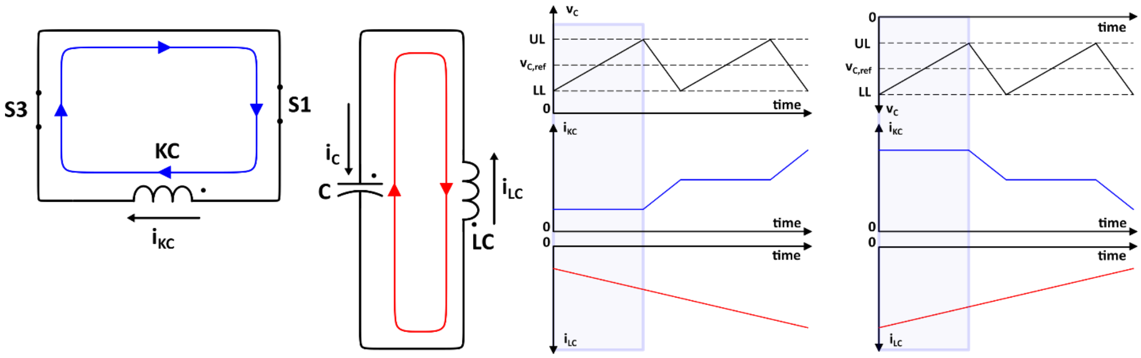

Figure 75 - State C=[1,0,1,0] with $i_{LC}<0$ and v_C, i_{KC} and i_{LC} trends

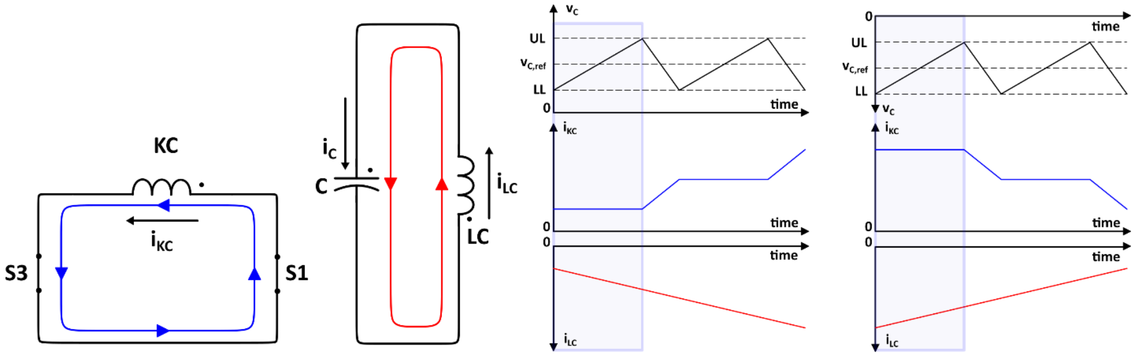

Figure 76 - State B=[0,1,0,1] with $i_{LC}<0$ and v_C, i_{KC} and i_{LC} trends

- State D=[0,1,1,0] with $i_{LC}<0$

State D is the only state that can be used to increase v_C when $i_{LC}<0$, this is the reason why i_{KC} shall be always greater than $|i_{LC}|$. If $|i_{LC}| > i_{KC}$ and $i_{LC} > 0$ imposing the state D=[0,1,1,0], for Kirchhoff's current law, $i_C < 0$ so v_C decreases instead of increasing and an undamped oscillation between KC, LC and C is observed. In this state, since $i_{KC}>|i_{LC}|$, the capacitor voltage increases from LL to UL. If v_C is positive, part of KC energy is transferred to C and LC. If v_C is negative part of C and LC energy is transferred to KC (Figure 77).

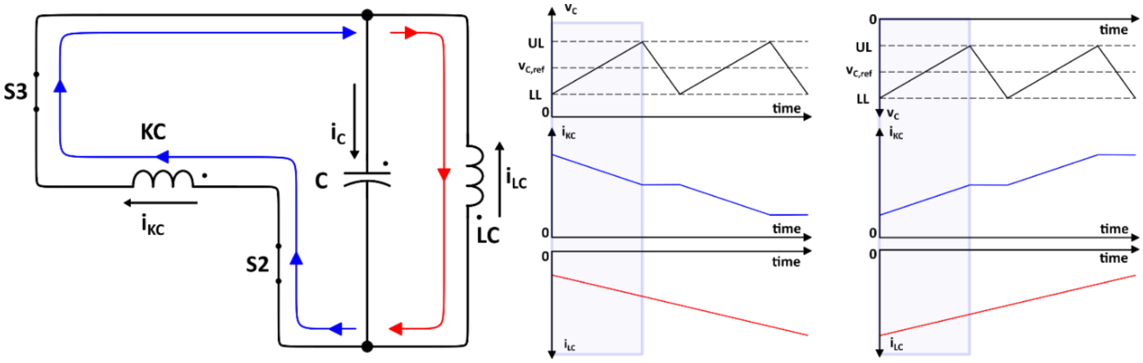

Figure 77 – State D=[0,1,1,0] with $i_{LC}<0$ and v_C, i_{KC} and i_{LC} trends

4.1.1.2 Switching patterns

Different patterns of the MEST states are imposed by the control system to maintain v_C within the hysteresis band limits (LL and UL).

During the first stages of the MEST control system development, a single-leg switching pattern was adopted. With this solution the commutations are concentrated on S1 – S2 to modulate v_C while S3 – S4 commutate only when i_{LC} changes polarity. The single-leg strategy adopts the sequence A-B-A-B… when $i_{LC}>0$ and D-C-D-C… when $i_{LC}<0$. With this solution, the commutations are in charge of S1 and S2 while S3 and S4 alternately carry i_{KC} depending on i_{LC} polarity.

The design optimization then leads to a new switching pattern, called the double-leg switching pattern, that focuses on the equalization of the commutation between the four equivalent switches:

- With $i_{LC}>0$ the sequence of the states for controlling v_C is A-B-A-C-A-B-A-C…
- With $i_{LC}<0$ the sequence of the states for controlling v_C is D-B-D-C-D-B-D-C…

The equalization of the switching losses between all four switches implies that the switching frequency of S1 and S2 is halved, in comparison with the single-leg switching pattern, for a given capacitance of C. In other terms, with the double-leg switching pattern, the C capacitance could be halved for a given limit on the switching frequency. This can be seen in the simulation results in section 4.5.2.2.

4.1.1.3 Patterns with increased dynamic performance

States D (with $i_{LC}>0$) and A (with $i_{LC}<0$) lead always to a higher derivative of v_C when compared to the other states. This behaviour results from the fact that the capacitor current module $|i_C|$

during these states is equal to $i_{KC}+|i_{LC}|$ (see Table 6) and is always higher than $|i_C|$ in the other states, which are equal to $i_{KC}-|i_{LC}|$ or i_{LC}. Figure 78 reports the different i_C values, depending on the states and considering LC inductance (L_{LC}) equal to KC inductance (L_{KC}), when varying i_{LC} from its minimum to its maximum value ($i_{LC,max}$ is the maximum LC current during the scenario and $i_{KC,min}$ is the minimum KC current during the scenario).

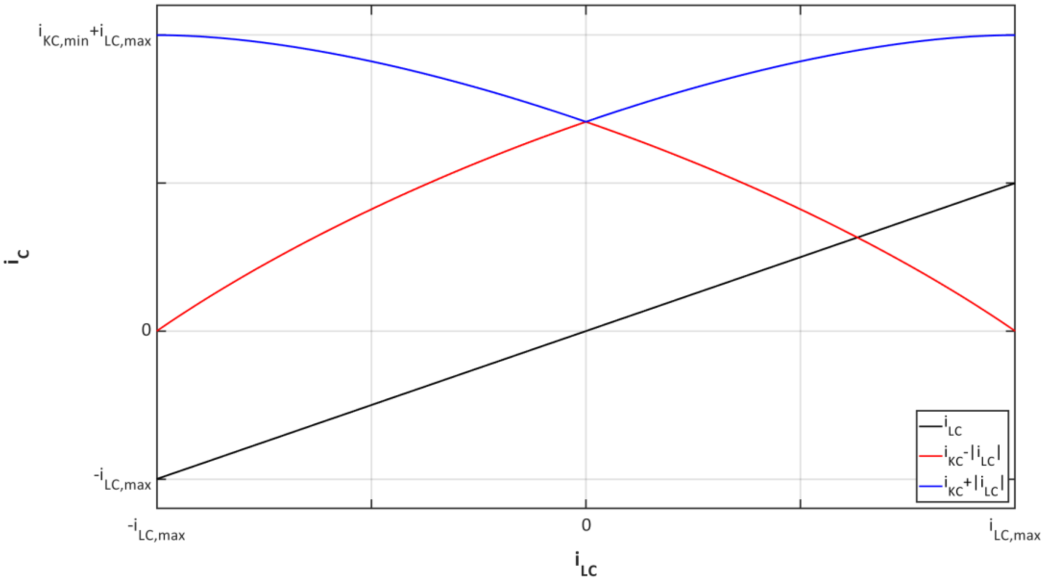

Figure 78 - i_C trends when varying i_{LC} from its minimum to its maximum value considering $L_{LC}=L_{KC}$

The use of patterns that comprise high voltage derivative states has the drawback to lead to the commutation of all four switches at each change of state (for instance if a sequence A-D-A-D… is imposed). Therefore, when the reference $v_{C,ref}$ is close to v_C and the MEST has a sufficient dynamic, the two high voltage derivative states should be avoided to keep the switching frequency within the design limit of the switches. The high voltage derivative states are used to increase the dynamic performance when $|v_{C,ref} - v_C| > \Delta V_{C,thr}$, with $\Delta V_{C,thr}$ a defined value, to increase (with $i_{LC}>0$) or decrease (with $i_{LC}<0$) v_C with the highest dynamic, and to follow as fast as possible $v_{C,ref}$.

In section 4.5.2.3 simulation results with the use of the high voltage derivative states are reported.

4.1.2 Sink coil current (i_{KC}) control strategy

During system operation, the PS has to compensate for the circuit losses and supply the power to the plasma. In other words, PS must keep constant the system energy constant during the pulse, and this is achieved by controlling i_{KC}. The i_{KC} control double loop (highlighted in blue in Figure 69) includes “KC current control” and “PS control” blocks. The first has as inputs the v_C, i_{LC}, the plasma current (i_P) and the total energy of the system (W_T). KC has to store before the pulse at least the double of the maximum energy stored by LC, the capacitor bank and the plasma during the foreseen scenario. Therefore, the maximum total energy of the system (W_T) is two times this value and can be known before the foreseen plasma pulse with this equation:

$$W_T = 2 \cdot max(w_{LC}(t) + w_C(t) + w_{\mathrm{P}}(\mathrm{t}) + w_{\mathrm{LC,P}}(t)) \qquad \textit{Eq. 14}$$

Considering the energy stored in the capacitor bank C equal to (C is the capacitance of the capacitor bank):

$$w_C(t) = \frac{1}{2} \cdot C \cdot v_C^2(t) \qquad \textit{Eq. 15}$$

The energy stored in LC:

$$w_{LC}(t) = \frac{1}{2} \cdot L_{LC} \cdot i_{LC}^2(t) \qquad \textit{Eq. 16}$$

The energy store in the plasma (L_P is the plasma inductance):

$$w_P(t) = \frac{1}{2} \cdot L_P \cdot i_P^2(t) \qquad \textit{Eq. 17}$$

And the energy stored due the magnetic coupling between LC and the plasma ($M_{LC,P}$ is the mutual inductance between LC and P):

$$w_{LC,P}(t) = M_{LC,P} \cdot i_P(t) \cdot \mathrm{i}_{\mathrm{LC}}(t) \qquad \textit{Eq. 18}$$

Then “KC current control” block computes KC current reference ($i_{KC,ref}$) to maintain constant the system energy. $i_{KC,ref}$ is derived as follows:

$$i_{KC,ref}(t) = \sqrt{\frac{2(W_T - w_{LC}(t) - w_C(t) - w_{\mathrm{P}}(\mathrm{t}) - w_{\mathrm{LC,P}}(\mathrm{t}))}{L_{KC}}} \qquad \textit{Eq. 19}$$

The “PS control” block is a PI controller that receives as input the measurement of i_{KC} and the reference $i_{KC,ref}$ and controls the PS to maintain near zero the difference between the two input signals. With this control scheme, the energy of the system remains constant during the pulse as can be seen in section 4.4.6.

4.2 Analytical calculation of the switching frequency

In the MEST system, the switching frequency of the switches is not fixed due to the hysteresis control: a band limits the functional region, but the capacitor voltage derivative (equal to the capacitor current i_C) depends on the circuit characteristics. The analytical calculation of the switching frequency depending on LC current is a fast tool to obtain a first estimation of the C capacitance to maintain the switching frequency under a defined maximum value during the MEST operation.

To evaluate the frequency of commutations, the variables of the frequency function have to be known. The capacitance C of the capacitor bank is a degree of freedom together with the band of the hysteresis control in the system design, which has the aim to maintain the switching frequency within a fixed maximum value. This maximum switching frequency value depends on the switches technology since the switch should undergo high voltages and high currents and it should commutate with a frequency of hundreds of Hz to obtain a sufficient dynamic. A great part of switch losses is due to the commutation of the switches which has to be limited to remain within the maximum junction temperature of the chosen components. Before setting up numerical simulations the switching frequency can be estimated with the following simplifications:

- during the switching period v_C is considered constant and equal to the reference $v_{C,ref}$;
- since the switching period is much lower than the time constant of the considered LC circuit, i_{LC} and i_{KC} are considered constant during the switching period.
- The “high derivate states” are not considered, since they are applied only sporadically.

The following calculation of the switching frequency considers the control of the system reported in section 4.1.1.2.

4.2.1 Switching frequency formula with negative Load Coil current ($i_{LC}<0$)

○ <u>State [0,1,1,0]:</u>

The energy needed to increase the capacitor voltage from the Lower Limit (LL) to the Upper Limit (UL), or vice versa, of the hysteresis band is:

$$\Delta W_C = \frac{1}{2} C \left[\left(v_{C,ref} + b \right)^2 - \left(v_{C,ref} - b \right)^2 \right] \qquad \textit{Eq. 20}$$

Where b is half of the total hysteresis band. The power entering the capacitor is:

$$P_{C,1} = v_{C,ref} \cdot (i_{KC} + i_{LC}) \tag*{Eq. 21}$$

The time interval in which S1 is off:

$$t_{S1,1} = \frac{\Delta W_C}{P_{C,1}} \tag*{Eq. 22}$$

This time interval is always a positive value because if $v_{C,ref}$ is positive both ΔW_C and $P_{C,1}$ are positive; if $v_{C,ref}$ is negative both ΔW_C and $P_{C,1}$ are negative.

- State [1,0,1,0] or state [0,1,0,1]:

The energy needed to decrease the capacitor voltage from the UL to the LL of the hysteresis band is calculated in Eq. 20. The capacitor ingoing power is:

$$P_{C,2} = v_{C,ref} \cdot i_{LC} \tag*{Eq. 23}$$

If $v_{C,ref}$ is positive also ΔW_C is positive and vice-versa. Now we are considering $i_{LC}<0$ therefore $P_{C,2}$ has always the opposite sign of ΔW_C.

To avoid negative time interval in the equation the absolute value of i_{LC} is considered.

The time interval in which S1 is on (state [1,0,1,0]) or off (state [0,1,0,1]) is:

$$t_{S1,2} = \frac{\Delta W_C}{v_{C,ref} \cdot |i_{LC}|} \tag*{Eq. 24}$$

- Switching frequency:

The switching period is the sum of the two intervals estimated before multiplied by 2 since the double leg-leg switching pattern is considered (see section 4.1.1.2):

$$\begin{aligned} T_{sw} = 2(t_{S1,1} + t_{S1,2}) = 2\left(\frac{\Delta W_C}{v_{C,ref} \cdot |i_{LC}|} + \frac{\Delta W_C}{P_{C,1}}\right) \\ = \frac{C\left[\left(v_{C,ref} + b\right)^2 - (v_{C,ref} - b)^2\right] i_{KC}}{v_{C,ref} \cdot (i_{LC}) \cdot (i_{KC} + i_{LC})} \end{aligned} \tag*{Eq. 25}$$

And the switching frequency is:

$$f_{sw} = \frac{1}{T_{sw}} = \frac{v_{C,ref} \cdot (i_{LC}) \cdot (i_{KC} + i_{LC})}{C\left[\left(v_{C,ref} + b\right)^2 - (v_{C,ref} - b)^2\right] i_{KC}} \qquad \text{Eq. 26}$$

4.2.2 Positive Load Coil current (i_{LC}>0)

- State [0,1,0,1] and [1,0,1,0]:

The energy needed to increase the capacitor voltage from the LL to the UL of the hysteresis band is calculated in Eq. 20. The capacitor incoming power:

$$P_{C,3} = v_{C,ref} \cdot i_{LC} \qquad \text{Eq. 27}$$

Time in which S1 is on (state [1,0,1,0]) or off (state [0,1,0,1]):

$$t_{S1,3} = \frac{\Delta W_C}{P_{C,3}} \qquad \text{Eq. 28}$$

This time interval is always a positive value because if $v_{C,ref}$ is positive both ΔW_C and $P_{C,1}$ are positive; if $v_{C,ref}$ is negative both ΔW_C and $P_{C,1}$ are negative.

- State [1,0,0,1]:

The capacitor incoming power:

$$P_{C,4} = v_{C,ref} \cdot (i_{KC} - i_{LC}) \qquad \text{Eq. 29}$$

The time in which S1 in on:

$$t_{S1,4} = \frac{\Delta W_C}{|P_{C,4}|} \qquad \text{Eq. 30}$$

This time interval is always a positive value because i_{KC}-i_{LC} is positive and if $v_{C,ref}$ is positive both ΔW_C and $P_{C,1}$ are positive; if $v_{C,ref}$ is negative both ΔW_C and $P_{C,1}$ are negative.

- Switching frequency:

The switching period is the sum of the two intervals estimated before multiplied by 2 since the double leg-leg switching pattern is considered (see 4.1.1.2):

$$T_{sw} = 2(t_{S1,3} + t_{S1,4}) = \frac{\Delta W_C}{|P_{C,4}|} + \frac{\Delta W_C}{P_{C,3}} = \frac{C\left[\left(v_{C,ref} + b\right)^2 - (v_{C,ref} - b)^2\right] i_{KC}}{i_{LC} \cdot v_{C,ref} \cdot (i_{KC} - i_{LC})} \tag{Eq. 31}$$

And the switching frequency is:

$$f_{sw} = \frac{1}{T_{sw}} = \frac{i_{LC} \cdot v_{C,ref} \cdot (i_{KC} - i_{LC})}{C\left[\left(v_{C,ref} + b\right)^2 - (v_{C,ref} - b)^2\right] i_{KC}} \tag{Eq. 32}$$

4.2.3 Considerations on the switching frequency

Eq. 26 and Eq. 1 are equal since Eq. 26 is evaluated for $i_{LC}<0$.

The switching frequency formula obtained in the previous sections can be simplified obtaining:

$$f_{sw} = \frac{1}{T_{sw}} = \frac{|i_{LC}| \cdot (i_{KC} - i_{LC})}{4 \cdot C \cdot b \cdot i_{KC}} = \frac{1}{4 \cdot C \cdot b} \cdot \frac{|i_{LC}| \cdot (i_{KC} - i_{LC})}{i_{KC}} \tag{Eq. 33}$$

Considering the hysteresis band constant during the MEST operation, the red factor is fixed and the blue factor varies during the pulse. In conclusion, considering $i_{KC}=i_{KC,ref}$ during the pulse, the complete system to evaluate the switching frequency is the following:

$$\begin{cases} f_{sw} = \dfrac{1}{4 \cdot C \cdot b} \cdot \dfrac{|i_{LC}| \cdot (i_{KC,ref} + i_{LC})}{i_{KC,ref}} \\ i_{KC,ref} = \sqrt{\dfrac{2(W_T - w_{LC} - w_C - w_{\mathrm{P}} - w_{\mathrm{LC,P}})}{L_{KC}}} \end{cases} \tag{Eq. 34}$$

Considering the MEST operation with values of voltage, current and LC inductance compatible with the power supply of a main poloidal field coil of a large tokamak reactor (with a similar size of ITER or EU DEMO or PILOT) it is possible to make additional considerations. With L_{LC} in the order of 1 H and the switching frequency limit of some hundreds of Hz the ratio $W_{KC,max}$/ $W_{C,max}$ ($W_{KC,max}$ and $W_{C,max}$ are the maximum energy that KC and C can store respectively) can become higher than 10^3. In this condition, the influence of the hysteresis band amplitude on i_{LC} and i_{KC} during the switching period is negligible as stated in the assumptions at the beginning of section 4.2. Moreover, in Eq. 34 can be seen that the switching frequency is virtually independent from the voltage reference $v_{C,ref}$ and inversely proportional to C and b. In detail, $v_{C,ref}$ affects w_C and then $i_{KC,ref}$, therefore f_{SW} depends on $v_{C,ref}$, but being w_C at least 3 order of magnitude lower than W_T its influence is negligible.

In Figure 79 is reported the switching frequency calculated using Eq. 34, for a swipe of i_{LC} from $I_{LC,max}$ and $-I_{LC,max}$ neglecting the plasma. The results in Figure 79 are generated considering $I_{LC,max}$, C, L_{LC} and L_{KC} are equal to the ones used for numerical simulation in section 4.4.

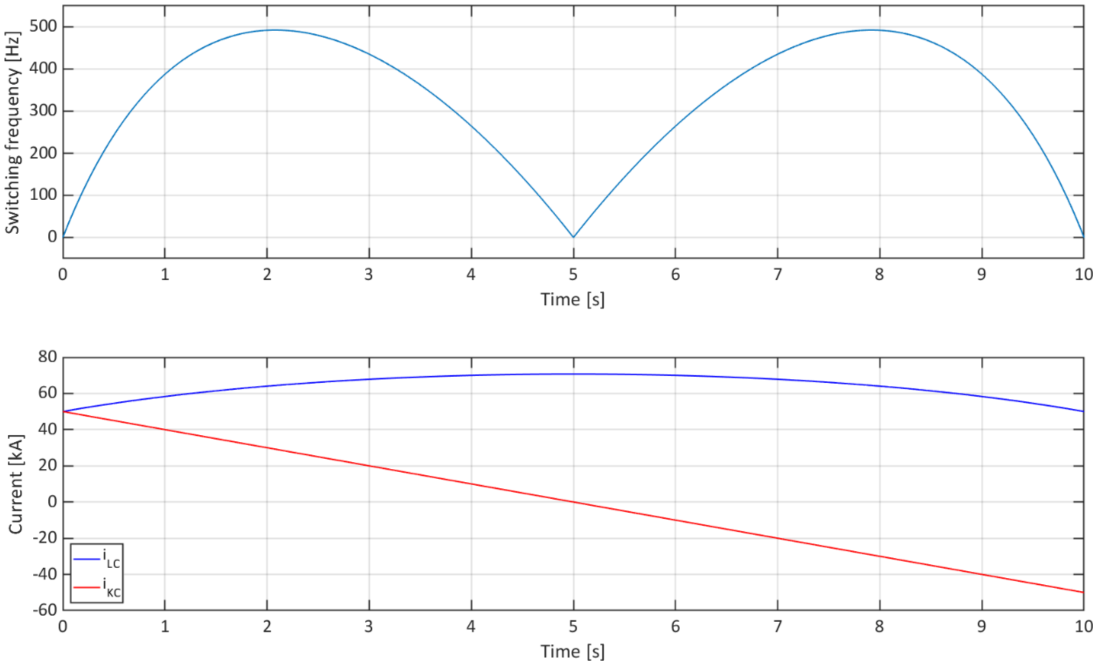

Figure 79 – Switching frequency for i_{LC} from $I_{LC,max}$ to $-I_{LC,max}$

From Eq. 34 can been derived that the $|i_{LC}/I_{LC,max}|$ value for witch the maximum switching frequency is reached depends only on the ratio L_{KC}/L_{LC}. The results are reported in Table 7.

Table 7 – $i_{LC}/I_{LC,max}$ value for witch the maximum switching frequency is reached

	$\|i_{LC}/I_{LC,max}\|$ (max. f_{sw})	Corresponding duty cycle of S1
$L_{KC}=L_{LC}$	0.584	55%
$L_{KC}=2L_{LC}$	0.550	53%

4.3 MEST numerical model

To verify the correct MEST operation and the design presented in section 4.4 and 4.5, a numerical model of MEST has been developed with Simulink. The numerical Simulink model will be reported and some blocks/subsystems operation will be explained and discussed individually. The model comprises two main objects:

- Model parameters and scenario script (script_modello.m): a MATLAB script where all the model data are defined as variables and i_{LC} reference is created according to the scenario.

- Simulink model (MEST.slx): the Simulink model with all the MEST system and control.

The model will be used to simulate the waveforms required by the plasma in the various phases of the pulse according to the reference scenario and the results obtained will be commented on.

4.3.1 Model parameters and scenario script

Figure 80 reports the code of script_modello.m MATLAB script in which all the variable required by the Simulink numerical model are declared (the values assigned to the variables changes according to the simulation).

```
%% SIMULATION DATA

t_step=5e-6;               % Fixed-step size of the simulation [s]

%% CIRCUIT DATA

L_KC=2.07;                  % Sink Coil inductance [H]
R_KC=0;                     % Sink Coil resistance [ohm]
L_LC=2.07;                  % Central Solenoid inductance [H]
R_LC=0;                     % Central Solenoid resistance [ohm]
C=7e-3;                     % Capacitor bank capacitance [F]
L_C=1e-8;                   % Capacitor bank parasitic inductance [H]

%% INPUT PARAMETETERS
f_sw=500;                   % [Hz] Maximum switching frequency of the MEST switches for
the frequency limiter
m=100;                      % [A] Minimum difference between i_KC and i_LC which is set
in the PS control
t_chargeTC=18;              % Time for the charge of KC [s]
t_chargeCS=8;               % Time for the charge of LC [s]
t_pulse=10;                 % Scenario pulse duration [s]
t_discharge=10;             % Time for the discharge of LC on KC [s]
w=0.1;                      % Hysteresis control tolerance with respect Vc_ref saturated
at w_inf and w_sup in the simulink model
w_inf=1000;                 % [V] minimum value of half hysteresis band
w_sup=1000;                 % [V] maximum value of half hysteresis band
d=4*w_sup;                  % When the difference between vC and vC_ref is higher than d
the control with high derivative states is used.
control=1;                 % choice between an open loop control (0) or a closed loop
control (1)
int_ext=1;                 % choice between an internal waveform (0) or an external
waveform (1)

%% PS CONTROL PARAMETERS
kp_PS=1.5;
ki_PS=100;
kd_PS=1;

%% CLOSED LOOP CURRENT CONTROL PARAMETERS
kp_iLC=170;
ki_iLC=0.5;
kd_iLC=1;

%% SWITCH DATA FOR "min ton min toff" BLOCK
toff_min=50e-6;                 % min toff of the IGCT [s]
ton_min=50e-6;                  % min ton of the IGCT [s]

%% SCENARIO
```

```
% folder where is located waveform_generator
path="…";
oldfolder = cd(path);
% scenario external waveform used during the pulse (PHASE 3)
sim('waveform_generator');
waveform=[waveform.time waveform.signals.values];
% return in the initial folder
cd(oldfolder);

% COMPUTATIONS

if control==1
    I_LC_max=max(abs(waveform(:,2)));                          % find max i_LC value in
the scenario [A]
    I_LC_0=waveform(1,2);                                      % find the intial i_LC
value in the scenario [A]
    Wt=(0.5*L_KC*(I_LC_max^2))+(0.5*L_LC*(I_LC_max^2));       % Total energy stored in
the inductors [J]
    I_KC_0=sqrt((Wt-(0.5*L_LC*(I_LC_0^2)))/((0.5*L_KC)));    % Initial KC and LC
current [A]
elseif control==0
    I_LC_max_ol=2000;                                          % Max LC current in the
scenario working in open loop [A]
    t_chargeCS=0;                                              % In open loop there is
not the pre-charge of CS (if I_LC_0 is set zero)
    I_LC_0=0;                                                  % Initial value if i_LC
[A]
    Wt=(0.5*L_KC*(I_LC_max_ol^2))+(0.5*L_LC*(I_LC_max_ol^2)); % Total energy stored in
the inductors [J]
    I_KC_0=sqrt((Wt-(0.5*L_LC*(I_LC_0^2)))/((0.5*L_KC)));    % Initial value of KC
current [A]
end

% PHASES

% PHASE 1
% charge of KC up to I_KC_0
ILC1=[0:t_step:t_chargeTC]';                                  % column vector of time
steps
ILC1=[ILC1, zeros(size(ILC1))];                               % i_LC=0 in the second
column
% PHASE 2
% charge of LC taking the energy from TC
ILC2=[t_chargeTC:t_step:(t_chargeCS+t_chargeTC)]';            % column vector of time
steps
ILC2=[ILC2, (ones(size(ILC2)))*I_LC_0];                       % i_LC=i_LC_0 in the
second column
% PHASE 3
% pulse
ILC3=[(t_chargeCS+t_chargeTC):t_step:(t_chargeCS+t_chargeTC+t_pulse); waveform(:,2)']'
% PHASE 4
% LC discharge into KC
ILC4=[(t_chargeCS+t_chargeTC+t_pulse):t_step:(t_chargeCS+t_chargeTC+t_pulse+t_discharge)]
';
ILC4=[ILC4, (ones(size(ILC4)))*0];
scenario=[ILC1; ILC2; ILC3; ILC4]';
save('scenario.mat', 'scenario');
```

Figure 80 – script_modello.m MATLAB script

4.3.2 Simulink model

Figure 81 reports Simulink model of the MEST circuit. The model is changed according to the simulation needed. All the control block and subsystem will be reported and explained in the next subsections.

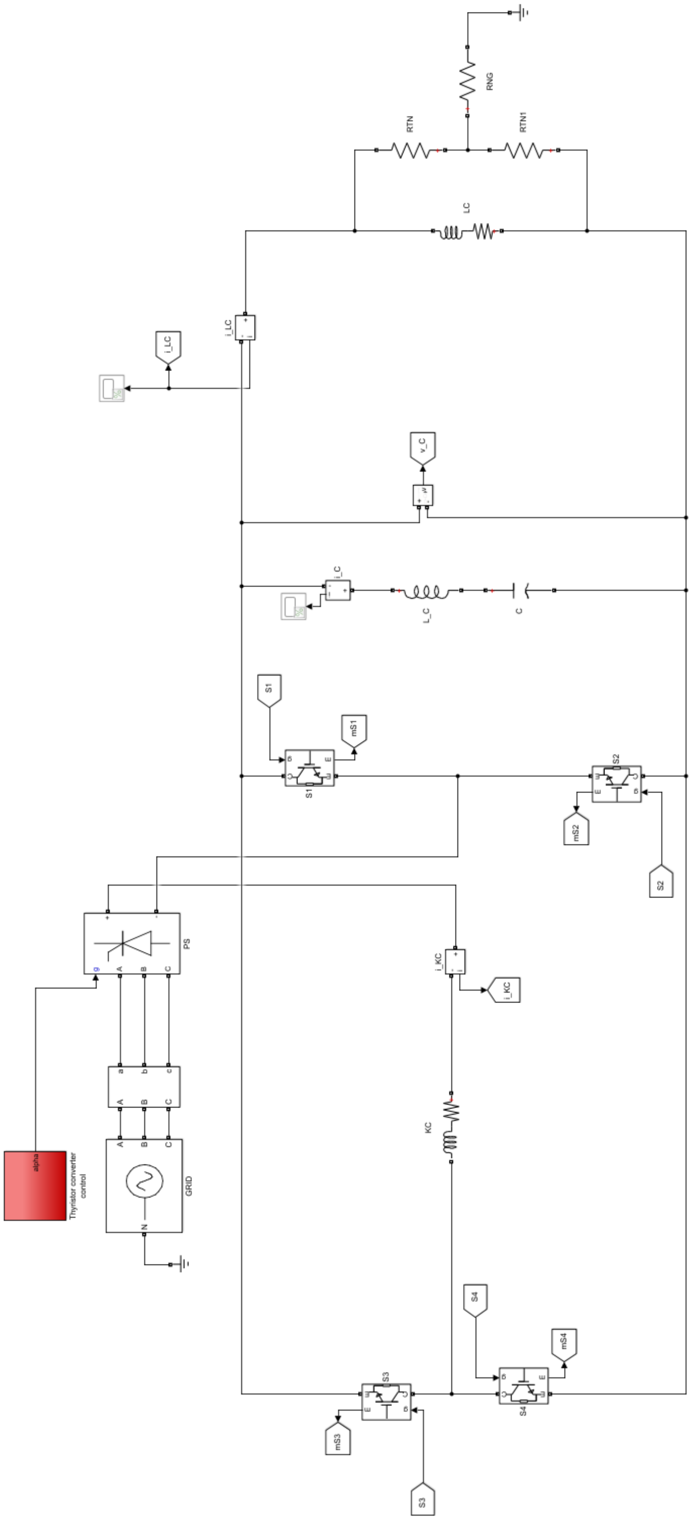

Figure 81 – MEST Simulink model

4.3.2.1 PS control (i_{KC} control)

As described in section 4.1.2 the PS is controlled with the aim to maintain constant the system total energy. In Figure 82 and Figure 83 are reported the MATLAB function block and its MATLAB function which compute the $i_{KC,ref}$. The reference $i_{KC,ref}$ is maintained higher than i_{LC} by a value m to assure that the KC current is always higher than the LC one (function i`_KC_ref  = fcn(i_LC,iP, v_C,L_LC,L_KC,M_LC_P,C,m,Wt)` Figure 83).

```
% INPUT:
% i_LC: LC current
% iP: plasma current
% v_C: C voltage
% L_LC: LC inductance
% L_KC: KC inductance
% L_P: plasma inductance
% M_LC_P: LC and plasma mutual inductance
% C: C capacitance
% m: margin between i_KC and i_LC
% Wt: total energy

W_LC=L_LC*(i_LC^2)/2;    %LC energy
W_C=C*(v_C^2)/2;         %C energy
W_P=18e-6*(iP^2)/2;      %Plasma energy
W_LC_P=M_LC_P*iP*i_LC;   %M_LC_P energy
i_KC_ref=sqrt(2*(abs(Wt-W_LC-W_C-W_P-W_LC_P))/L_KC);    %i_KC reference

% A margin is mantained between i_LC and i_KC
if (i_KC_ref-abs(i_LC))<m
    i_KC_ref=abs(i_LC)+m;
end
end
```

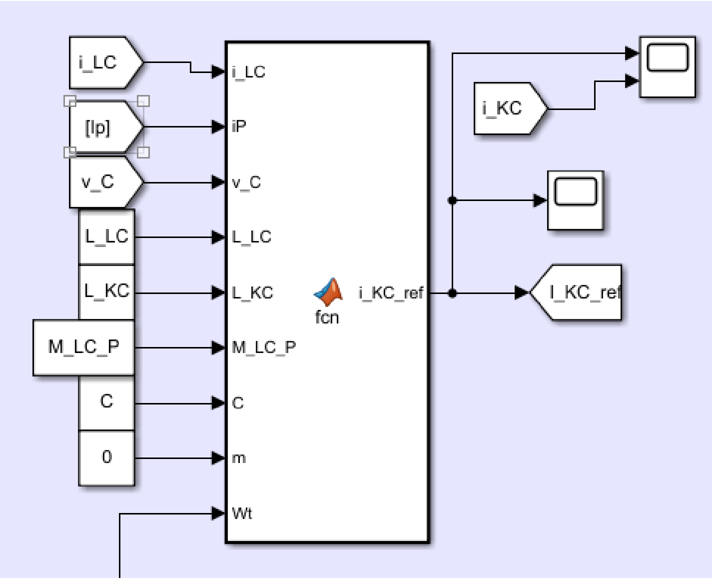

Figure 82 – Simulink block of the $i_{KC,ref}$ calculator

```
function i_KC_ref  = fcn(i_LC,iP, v_C,L_LC,L_KC,M_LC_P,C,m,Wt)
% INPUT:
```

```
% i_LC: LC current
% iP: plasma current
% v_C: C voltage
% L_LC: LC inductance
% L_KC: KC inductance
% L_P: plasma inductance
% M_LC_P: LC and plasma mutual inductance
% C: C capacitance
% m: margin between i_KC and i_LC
% Wt: total energy

W_LC=L_LC*(i_LC^2)/2;    %LC energy
W_C=C*(v_C^2)/2;         %C energy
W_P=18e-6*(iP^2)/2;      %Plasma energy
W_LC_P=M_LC_P*iP*i_LC;   %M_LC_P energy
i_KC_ref=sqrt(2*(abs(Wt-W_LC-W_C-W_P-W_LC_P))/L_KC);    %i_KC reference

% A margin is mantained between i_LC and i_KC
if (i_KC_ref-abs(i_LC))<m
    i_KC_ref=abs(i_LC)+m;
end
end
```

Figure 83 – MATLAB function of the $i_{KC,ref}$ calculator

In the numerical model the PS is modelled as a 6-pulse thyristor converter which is controlled by the subsystem reported in Figure 84. The subsystem is composed by a PI controller which receives as input the error between $i_{KC,ref}$ and i_{KC} providing the thyristor firing angle (alpha) as output. Alpha enters in the block Pulse Generator, which gives the proper command signal to all the thyristors of the PS, synchronized with the grid voltages using a PLL block.

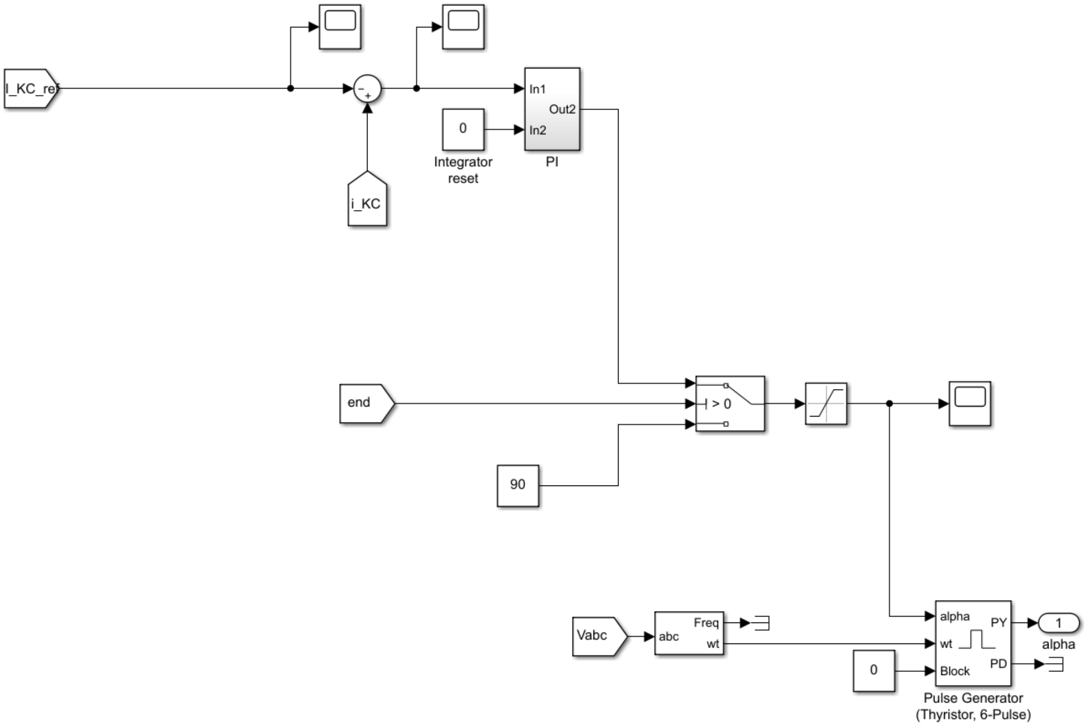

Figure 84 – Simulink subsystem of the PS control

4.3.2.2 Load current control (i_{LC} control)

As described in section 4.1.1, the voltage on LC (v_C) is regulated via an hysteresis control witch acts on the four switches to follow its reference $v_{C,ref}$ generated by the load current control loop. The control block and its function in the numerical model are reported in Figure 85 and Figure 86.

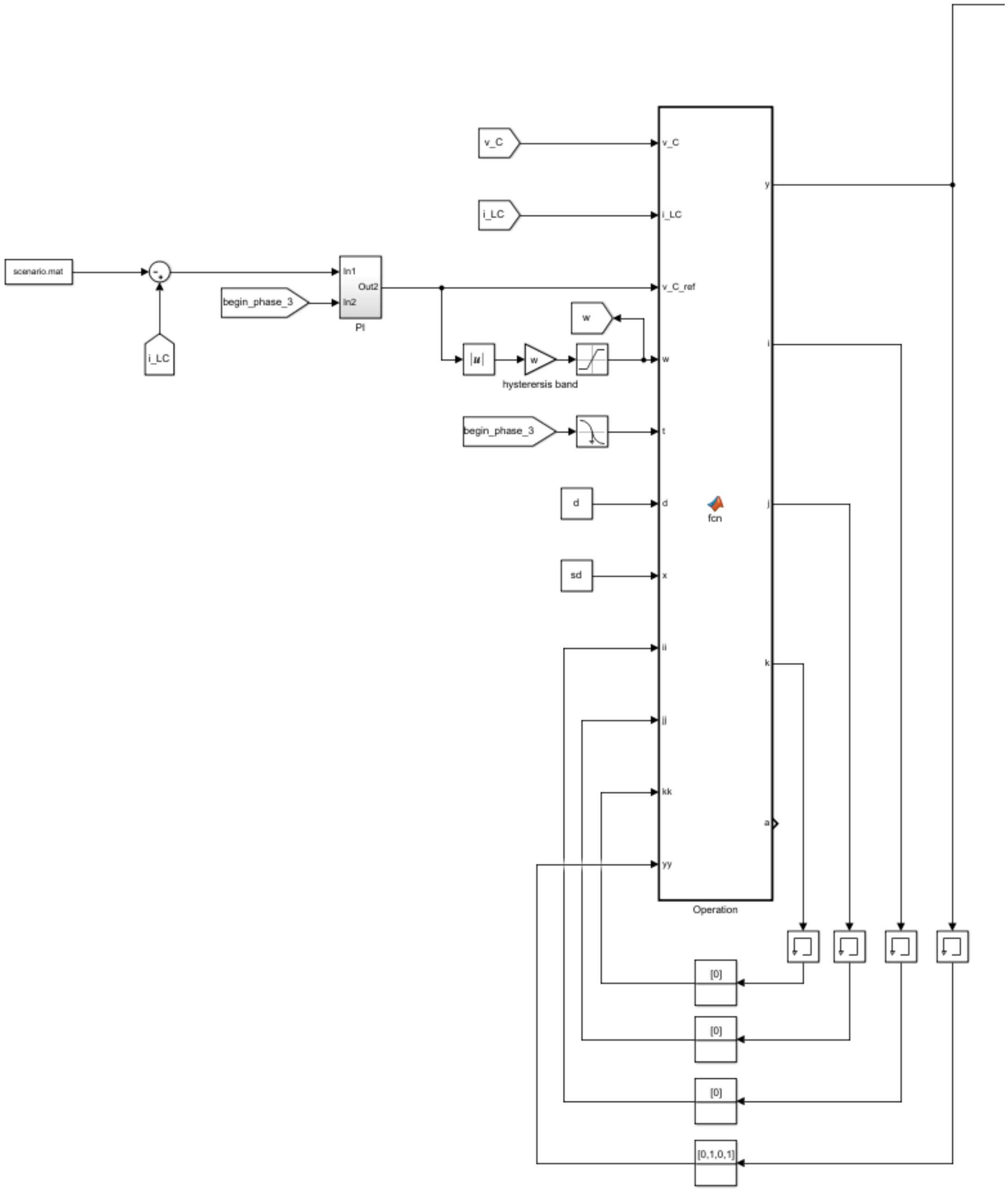

Figure 85 – i_{LC} control block

```
function [y,i,j,k,a,hh] = fcn(v_C,i_LC,v_C_ref,w,t2,t3,d,x,ii,jj,kk,yy)
% y: switches command signal
% yy: switches command signal in the previous step
% ii: i value in the previous step
% jj: j value in the previous step
% kk: k value in the previous step

y=yy;
i=ii;     %counter to alternate the switches change of state between the right and the
left legs when iLC>0
j=jj;     %counter to alternate the switches change of state between the right and the
left legs when iLC<0
k=kk;

hh=0;


%if the v_C-v_C_ref is over a certain limit the "high derivative" states
%are used increasing the dinamic of the system
if abs(v_C-v_C_ref)>=d
    a=1;
else
    a=0;
end

%x==0 single-leg strategy, x==1 dougle-leg strategy
if x==0
    i=0;
    j=0;
    a=0;
end
%to trigger the control system at the beginning of the scenario in case iLC initial value
is zero
if t3==2
    if v_C_ref>0
        y=[0,1,1,0]';
        k=1;
    else
        y=[1,0,0,1]';
        k=1;
    end
else
    if i_LC>0
        if v_C>=v_C_ref+w
            y=[1,0,0,1]';
            k=1;
            hh=1;
        elseif v_C<v_C_ref-w
            if a==0
                if i==0 && k==1 %switch right leg
                    y=[0,1,0,1]';
                    i=1;
                    k=0;
                elseif i==1 && k==1 %switch left leg
                    y=[1,0,1,0]';
                    i=0;
                    k=0;
                end
            elseif a==1
                y=[0,1,1,0]';
                k=0;
            end
        end
    elseif i_LC<0
        if v_C<v_C_ref-w
            y=[0,1,1,0]';
            k=1;
        elseif v_C>=v_C_ref+w
```

```
            if a==0
                if j==0 && k==1 %switch right leg
                    y=[1,0,1,0]';
                    j=1;
                    k=0;
                elseif j==1 && k==1 %switch left leg
                    y=[0,1,0,1]';
                    j=0;
                    k=0;
                end
            elseif a==1
                y=[1,0,0,1]';
                k=0;
            end
        end
    end

    yy=y;
    jj=j;
    ii=i;
    kk=k;
end
```

Figure 86 – MATLAB function of the i_{LC} control block

4.3.2.3 IGCTs Minimum on-time and off-time

The IGCTs require a variable time interval to fully turn-on and turn-off depending on the circuit conditions. If, for instance, the IGCT is turned off for a too short a time the turn-on characteristics specified in the data sheet cannot be guaranteed if a certain minimum off time is not maintained. A time interval during which the IGCT should not commute is considered in the model since it could be affect the system dynamic [33].

To implement the minimum on-time and off-time of the IGCTs in the model has been created the Simulink subsystem depicted in Figure 87. This block is located after the i_{LC} control block receiving as input the command signal of the switches and giving as output the modified IGCTs command signal. This subsystem maintains constant the input command signal of the IGCT for a time equal to minton after the switch is switched on or for a time equal to mintoff after the switch is switched off. In the numerical model, during these times, the IGCTs can’t commute.

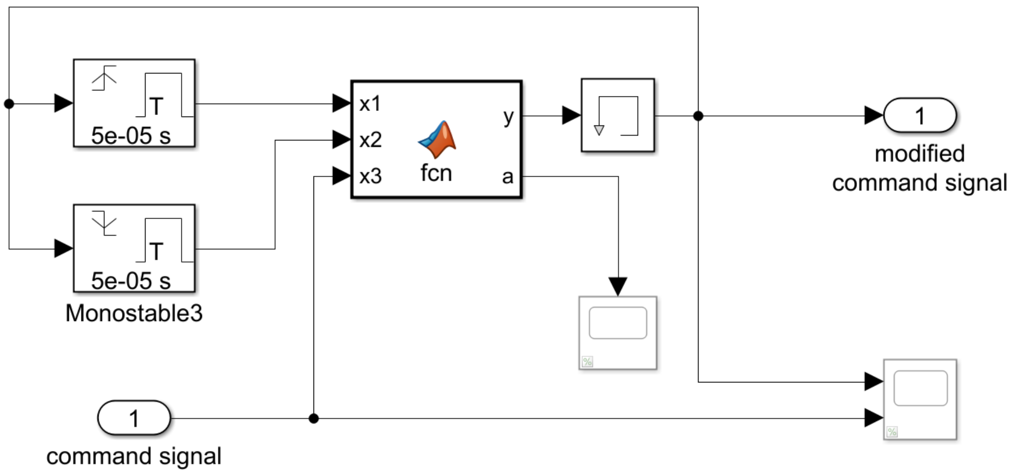

Figure 87 – IGCT minimum on-time and off-time subsystem

```
function [y,a] = fcn(x1,x2,x3)
%x1 is the signal from the monostable multivibrator with rising edge detection
%x2 is the signal from the monostable multivibrator with falling edge detection
%x3 is the unmodified signal (input)
%y is the modified signal
%a=1 when the input signal is modified (to see the time intervals when the input signal
is modified)
if x1==1 && x2==0
    y=1;
else
    if x2==1 && x1==0
        y=0;
    else
        y=x3;
    end
end
if y~=x3
    a=1;
else
    a=0;
end
end
```

Figure 88 – MATLAB function of IGCT minimum on-time and off-time

4.3.2.4 Frequency limiter

In the model, it is also implemented a frequency limiter for the IGCTs command signal to limit the switching frequency to the chosen value. The subsystem and its function, given in Figure 89 and Figure 90, are located after the i_{LC} control block and it receives as input the switches command signal and gives as output the modified command signal. The block ignores every variation of the command signal if it has a frequency faster than the maximum value imposed.

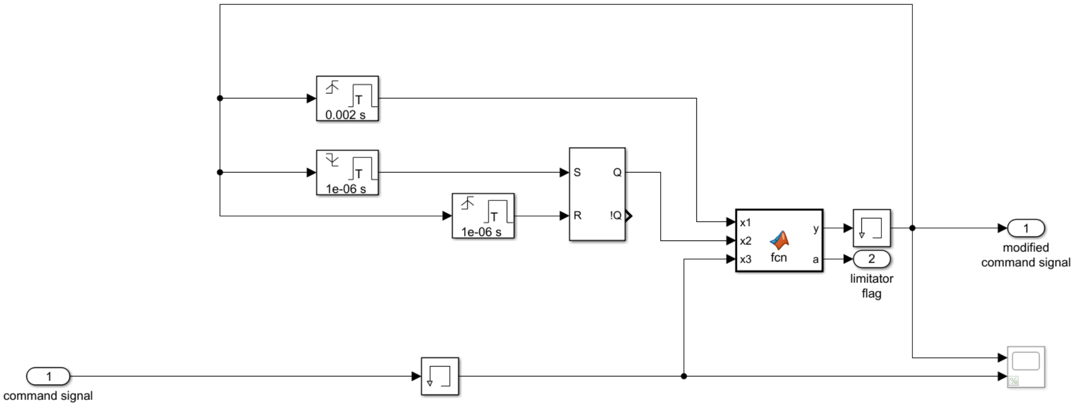

Figure 89 – Simulink subsystem of the frequency limiter

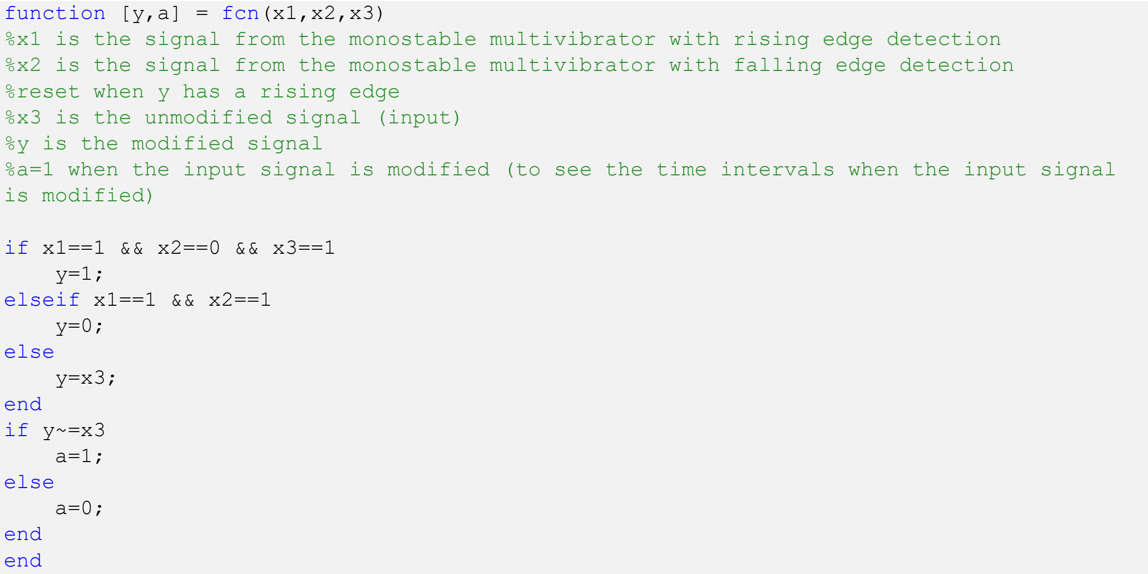

```
function [y,a] = fcn(x1,x2,x3)
%x1 is the signal from the monostable multivibrator with rising edge detection
%x2 is the signal from the monostable multivibrator with falling edge detection
%reset when y has a rising edge
%x3 is the unmodified signal (input)
%y is the modified signal
%a=1 when the input signal is modified (to see the time intervals when the input signal
is modified)

if x1==1 && x2==0 && x3==1
    y=1;
elseif x1==1 && x2==1
    y=0;
else
    y=x3;
end
if y~=x3
    a=1;
else
    a=0;
end
end
```

Figure 90 – MATLAB function of the frequency limiter

4.4 MEST system applied to PILOT Central Solenoid

In recent years, interest in Fusion-Fission Hybrid Reactor (FFHR) has grown due their potential applications in the production of electrical energy, the transmutation of nuclear waste, and the supply of fuel for fission reactors [25] [28] [29]. A fusion reactor in a FFHR has only to produce fast 14.1 MeV neutrons. With such a requirement the performance required to a fusion reactor for this application are much less stringent with respect a fusion reactor for energy production. The RFP seems a valid solution as fusion neutron source for three main reasons:

- the ability to reach the burning regime only using the ohmic heating therefore avoiding complex and sophisticated additional heating systems;

- Toroidal field windings rated for low magnetic field (the core toroidal flux is mainly generated by the plasma itself) avoiding superconductor technology and achieving a great simplification of the whole reactor;
- Self-organized plasma, relatively easy to produce and whose weak disruption are not harmful for the machine.

RFP reactors have a higher plasma loop voltage with respect to a tokamak with the same major and minor radii and plasma current. This leads to a lower duration of the plasma pulse for a given available magnetic flux stored by the Central Solenoid (CS) before the pulse. For its characteristic, a large RFP reactor requires high peaks of active power, for the gas breakdown and plasma current ramp-up, with a high rate (one every tens of seconds). Furthermore, the use of SNU to obtain the magnetic flux variation for the plasma current initiation and ramp-up will dissipate a great amount of energy that will significantly reduce the overall system efficiency. In this frame, the MEST seems a promising solution to cope with the frequently active power peaks required by a large RFP reactor, achieving a decoupling between the reactor main coils and the grid. In addition, the MEST allows to recover the magnetic energy that can be transferred between KC, LC and plasma without dissipations. The MEST principle is then applied to the CS circuit of a Fusion-Fission Hybrid Reactor (FFHR), based on RFP configuration, operated by exploiting the flux double swing reversing the magnetizing current towards high negative values. A RFP reactor can operate in a so-called “continuously pulsed operation” as shown in Figure 91 reaching a high duty cycle.

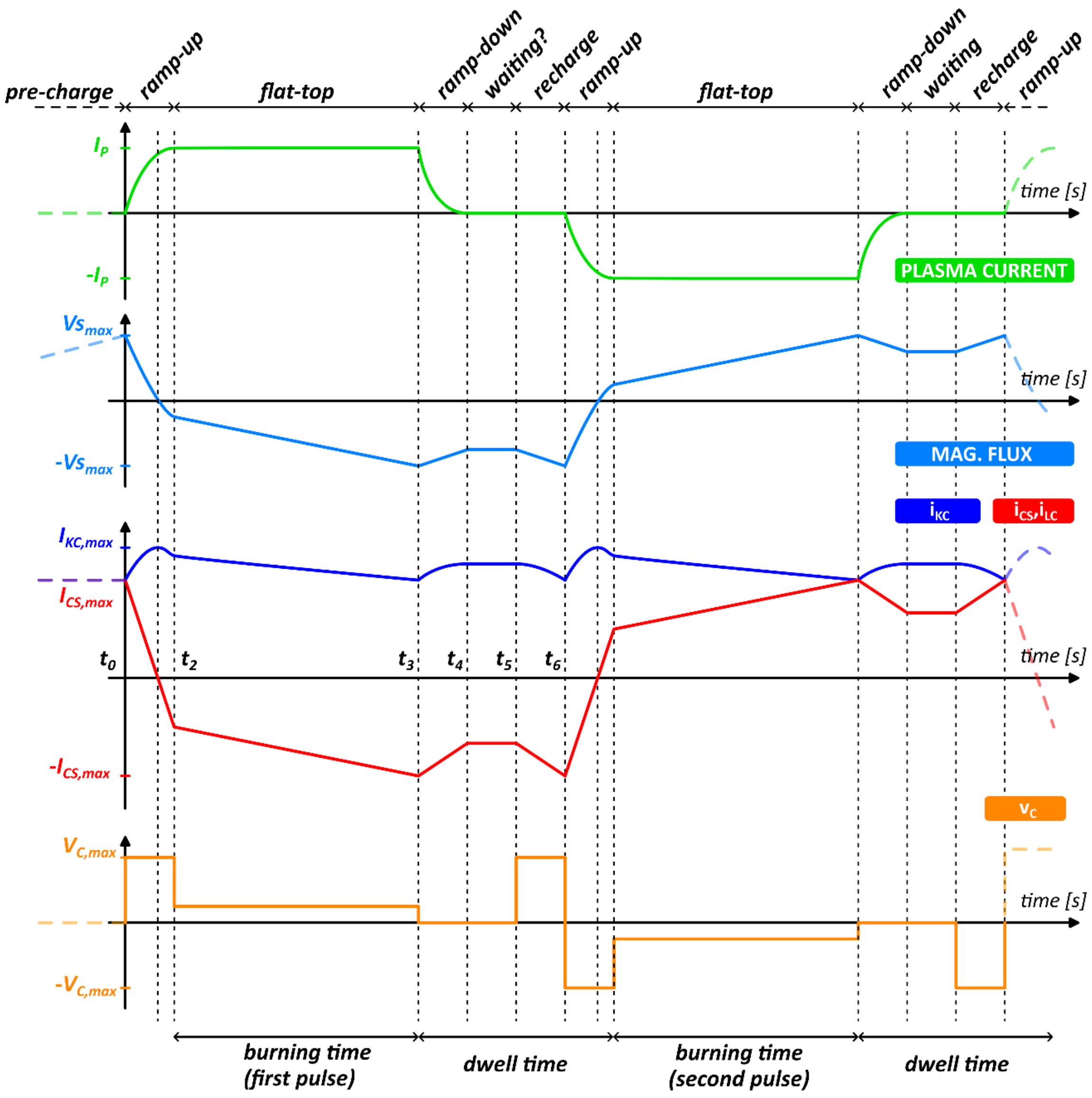

Figure 91 - Sketch of the “continuous pulsed mode” operation.

The phases of the pulse in the “continuously pulsed operation” can be summarized as follows:

- After the CS pre-charge the gas breakdown and plasma current fast ramp-up is obtained by an abrupt decrease of the CS current. The consequent decrease of the magnetizing flux induces a high toroidal loop voltage that ionizes the plasma and increase the plasma current to the flat-top value. In RFP reactors there are not intrinsic limitation on the plasma current increase rate, due to its self-organizing behaviour, and the current can increase with value of tens of MA/s as in RFX-mod experiment.
- The plasma current is sustained at a constant flat-top value decreasing the magnetizing flux down to its minimum value ($-Vs_{max}$) with a derivative proportional to the needed loop voltage. The duration of this phase depends on the value of plasma loop voltage, the higher

the loop voltage and the lower is the time duration of the flat-top and therefore of the plasma pulse.

- Immediately after reaching the minimum magnetizing flux value, the decrease of the plasma current to zero takes place. During this process, the magnetizing current is almost constant or decrease by a small value depending on the method used to terminate the plasma current. After the ramp-down of the plasma current the magnetizing flux is recovered up to its minimum value ($-Vs_{max}$) and another pulse can take place again. The following pulse, starting from the minim value of the magnetizing flux, will have a plasma current in the opposite direction of the previous one.

This sequence of pulses with positive and negative plasma currents can be repeated continuously with a short dwell time. The dwell time (time interval in which the reactor does not produce energy between two flat-top phases) is composed by the ramp-up, the ramp-down and the recharge phases.

4.4.1 Parameters of the reference PILOT reactor

A conceptual design of the MEST system has been performed assuming as reference the PILOT RFP reactor [25], characterized by the main tentative parameters summarized in Table 8.

Table 8. Main data of PILOT RFP reactor

Parameters	Value
Major radius (R_0)	6 m
Minor radius (a)	1.5 m
Plasma current	20 MA
Plasma loop voltage	4 V
Central Solenoid rated current ($I_{CS,max}$)	50 kA
Turns of the Central Solenoid(N)	1000
Central Solenoid sectors / turns per sector	6 / 166
Central Solenoid radius (R_M)	2.2 m

In this first design study, the rated voltage of the Central Solenoid has been considered 90 kV, as a trade-off between the number of series connected switches per equivalent switch, in the energy transfer system of each sector, and the duration of the ramp-up phase, therefore the rated voltage of each magnetizing winding sector is 15 kV. In Figure 92, the proposed scheme is enriched with the plasma branch, mutually coupled with CS coil.

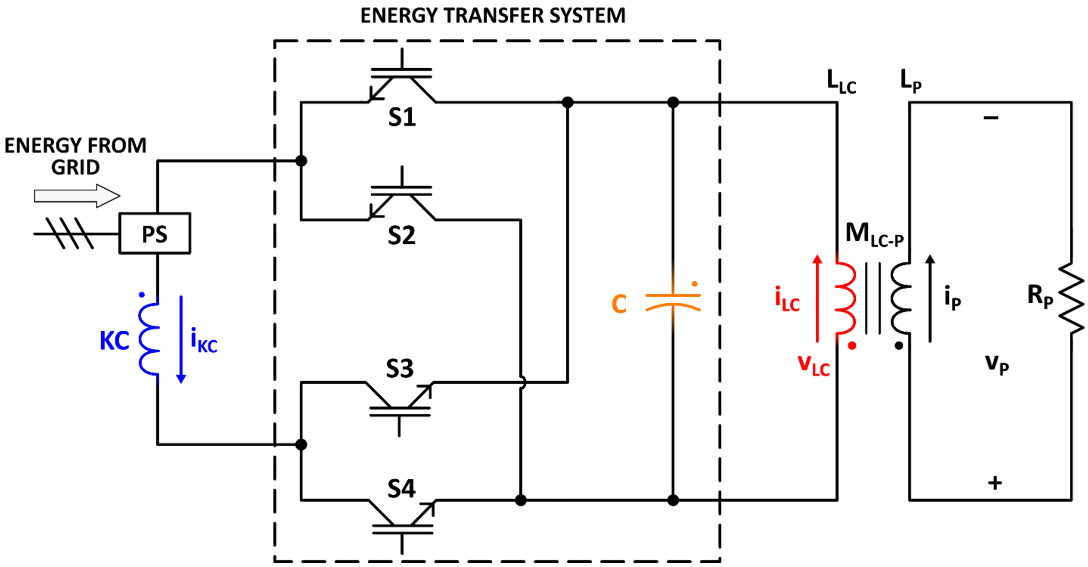

Figure 92 - Equivalent scheme of MEST supplying the CS magnet coupled with the plasma

In section 4.4.2 and 4.4.3 the circuit inductances and the pulse phases characteristic are calculated to confirm the main data of PILOT reactor and derive the data necessary for the design of the MEST system. In the proposed design, as a first design approach, the KC inductance is chosen equal to LC inductance. Using different values of KC inductance leads to different values of the KC current during the plasma pulse but does not affect the CS voltage and current and the overall operation of the MEST system from CS and plasma side. In other words, it will lead to a different design of KC coil, PS and the switches of the energy transfer system. Some of these different design considerations can be found in section 4.5.

4.4.2 Circuit inductances calculation

To evaluate the magnetic coupling between the magnetising winding, also called Central Solenoid (CS), and the plasma, the situation is schematically described by two currents (the magnetising current I_M and the plasma current I_P) distributed on toroidal coaxial layers M and P that represent respectively the magnetising winding and the plasma as shown in Figure 93.

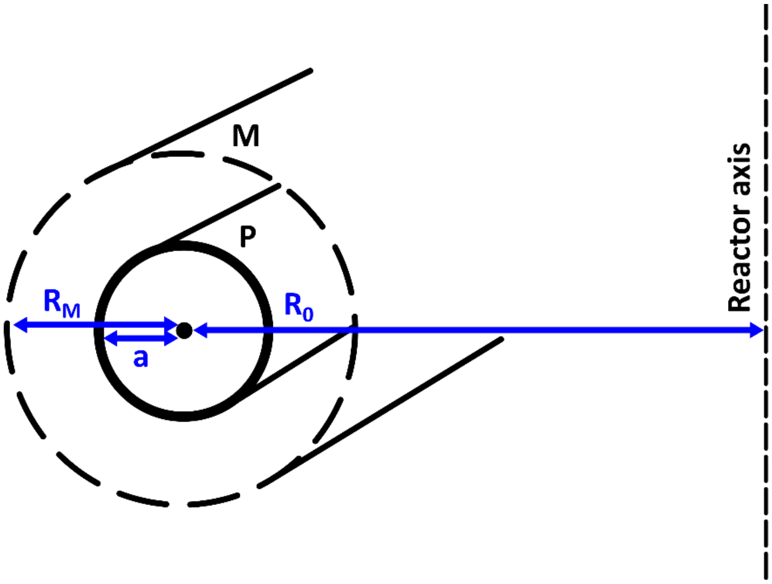

Figure 93 – Sketch of plasma current and magnetizing current coaxial distribution

The plasma inductance can be estimated considering two components: the plasma internal inductance ($L_{P,int}$) and plasma external inductance ($L_{P,ext}$). The internal inductance refers to the one correlated to the total magnetic flux inside the plasma, since the external toroidal magnetic flux, usually generated by toroidal field coils in tokamak reactors, is negligible with respect to the one generated by the plasma itself and it is obtained as follows:

$$L_{P,int} \cong (3 \div 4)\mu\frac{R_0}{4} = (3 \div 4) \times 1.25 \times 10^{-6} \times \frac{6}{4} = 5.6 \div 7.5\ \mu H \qquad \text{Eq. 35}$$

The plasma external inductance and the single turn magnetising winding inductance can be computed as the inductance of a thin wall cylindrical conductor with a superficial distribution of the current:

$$L_{P,ext} = \mu R_0\left(\ln\left(\frac{8R_0}{a}\right) - 2\right) = 1.25 \times 10^{-6} \times 6 \times \left(\ln\left(\frac{8 \times 6}{1.5}\right) - 2\right) = 10.99\ \mu H \cong 11\ \mu H \qquad \text{Eq. 36}$$

$$L_{CS,st} = \mu R_0\left(\ln\left(\frac{8R_0}{R_M}\right) - 2\right) = 1.25 \times 10^{-6} \times 6 \times \left(\ln\left(\frac{8 \times 6}{2.2}\right) - 2\right) = 8.12\ \mu H \qquad \text{Eq. 37}$$

The total plasma inductance is:

$$L_P = L_{P,int} + L_{P,ext} \cong 7\ \mu H + 11\ \mu H = 18\ \mu H \qquad \textit{Eq. 38}$$

From the previous calculations the inductance matrix describing the coupling between the central solenoid and the plasma is:

$$\begin{vmatrix} V_{CS} \\ V_P \end{vmatrix} = \begin{vmatrix} L_{CS} & M_{CS-P} \\ M_{CS-P} & L_P \end{vmatrix} \times \begin{vmatrix} \frac{di_{CS}}{dt} \\ \frac{di_p}{dt} \end{vmatrix}$$

$$= \begin{vmatrix} N^2 \times L_{CS-single\ turn} & N \times L_{CS-single\ turn} \\ N \times L_{CS-single\ turn} & L_P \end{vmatrix} \times \begin{vmatrix} \frac{di_{CS}}{dt} \\ \frac{di_p}{dt} \end{vmatrix} \qquad \textit{Eq. 39}$$

$$= \begin{vmatrix} 8.12 & 0.00812 \\ 0.00812 & 0.000018 \end{vmatrix} \times \begin{vmatrix} \frac{di_{CS}}{dt} \\ \frac{di_p}{dt} \end{vmatrix}$$

With M_{CS-P} the mutual inductance between the plasma and the central solenoid computed considering the magnetizing flux fully linked with the plasma.

The plasma resistance during the ramp-up is higher than the usual Spitzer value because of the plasma relaxation processes and MHD instabilities and is estimated from experimental data. The total contribution to the volt-second consumption during plasma current rump-up is assumed equivalent to about half the flux related to the internal plasma inductance [25] [30]; consequently, the resistance R_P is substituted with an equivalent inductance equal to 4 µH. During the flat top R_P produces 4 V resistive voltage drop, at 20 MA plasma current.

Since during the ramp-up phase the plasma loop voltage is higher than the flat-top one, the higher plasma resistance is modelled through an additional inductance equal to half of the plasma internal inductance:

$$L_{P,ramp\ up} = L_P + \frac{L_{P,int}}{2} \cong 18\ \mu H + 4\ \mu H = 22\ \mu H \qquad \textit{Eq. 40}$$

4.4.3 Pulse phases calculation

The following calculations have been performed with reference to the equivalent t-circuit (see Figure 94) to consider the magnetic coupling between the CS and the plasma. Considering the equivalent t-circuit of the coupled inductors L_{CS} and L_P, on the plasma-side there are the following inductances:

$$L_M = \frac{M_{CS-P}}{N} = \frac{0.00812}{1000} = 8.12\ \mu H \qquad \text{Eq. 41}$$

$$L_{CS,st} = \frac{L_{CS}}{N^2} - L_M = \frac{8.12}{10^6} - \frac{0.00812}{10^3} = 0\ H \qquad \text{Eq. 42}$$

$$L_{P,eq} = L_P - L_M = 18 - 8.12 = 9.88\ \mu H \qquad \text{Eq. 43}$$

Where L_M is the magnetizing inductance, $L_{CS,st}$ is the single turn equivalent inductance of CS and $L_{P,eq}$ is the equivalent plasma inductance.

The single turn equivalent inductance of the CS coil is equal to zero because the magnetising flux is fully linked with plasma (as usual) thus the magnetising inductance and the CS single turn inductance are equal.

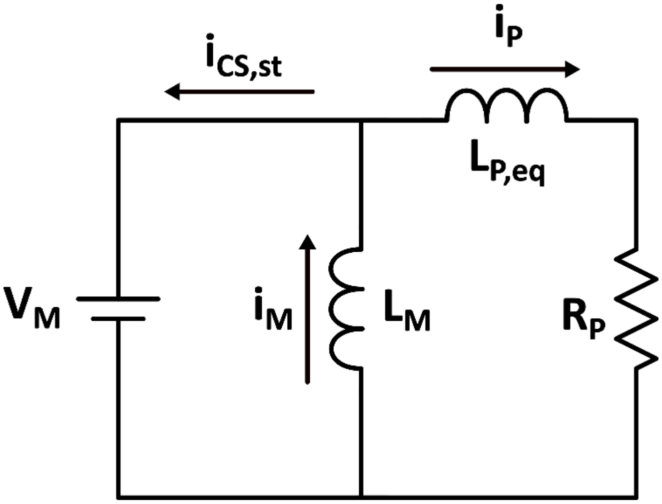

Figure 94 – Simplified equivalent scheme of the mutual coupling between CS and the plasma

4.4.3.1 Ramp-up phase

During the ramp-up the plasma current rises from 0 A to 20 MA and the additional inductance which considers the higher plasma resistance during the ramp-up is equal to 4 µH has discussed previously. Therefore, the plasma magnetic flux variation during the ramp-up is:

$$\Delta\Phi_{P,ramp\ up} = \Delta i_P \times L_{P,eq-ramp\ up} = (20 \times 10^6) \times [(9.88 + 4) \times 10^{-6}] = 277.6\ Wb \qquad \text{Eq. 44}$$

The initial value of the magnetising winding L_M magnetic flux, with i_M equal to 50 MA (on the plasma-side), is:

$$\Phi_{L_M}(t_0) = i_M(t_0) \times L_M = (50 \times 10^6) \times (8.12 \times 10^{-6}) = 406\ Wb \qquad \text{Eq. 45}$$

And the L_M flux variation is equal to the plasma flux variation during the ramp-up:

$$-\Delta\Phi_{L_M,ramp\ up} = \Delta\Phi_{P,ramp\ up} = 277.6\ Wb \qquad \text{Eq. 46}$$

Part of the $\Delta\Phi_{P,ramp\text{-}up}$ is devoted to increase the plasma current against the resistive loop voltage:

$$\begin{aligned}\phi_{ramp-up\ resistive} &= (L_{P,eq-ramp\ up} - L_{P,eq}) \times \Delta i_P \\ &= [(13.88\ - 9.88\ ) \times 10^{-6}] \times (20 \times 10^6) = \ 80\ \ Wb\end{aligned} \qquad \text{Eq. 47}$$

The plasma voltage drop caused by the resistive loop voltage is:

$$V_{pl-resitive,ramp-up} = \frac{80\ Wb}{3.084\ s} = 25.94\ V \qquad \text{Eq. 48}$$

The magnetising flux at the end of the ramp-up phase is:

$$\Phi_{L_M}(t_2) = \Phi_{L_M}(t_0) + \Delta\Phi_{L_M,ramp\ up} = 406 - 277.6 = 128.4\ Wb \qquad \text{Eq. 49}$$

At t_2 the current of the magnetising winding L_M is:

$$i_M(t_2) = \frac{\Phi_{L_M,ramp\ up}}{L_M} = \frac{128.4}{8.12 \times 10^{-6}} = 15.813\ MA \qquad \text{Eq. 50}$$

Therefore, the variation of i_M during the ramp-up is:

$$\Delta i_M = i_M(t_2) - i_M(t_0) = \frac{\Delta\Phi_{L_M,ramp\ up}}{L_M} = -34.187\ MA \qquad \text{Eq. 51}$$

At $t=t_2$ the current of the central solenoid is:

$$i_{CS,st}(t_2) = i_M(t_2) - i_P(t_2) = 15.813 - 20 = -4.187\ MA \qquad \text{Eq. 52}$$

Which corresponds to -4.187 kA on the CS-side.

Considering 90 V ($V_{M\text{-ramp up}}$) applied to the magnetizing winding and a linear shape of i_M during the ramp-up, the ramp-up duration is:

$$V_{M-ramp\ up} = 90\ V = L_M \frac{di_{M-ramp\ up}}{dt} = 8.12 \times 10^{-6} \times \frac{34.187 \times 10^6}{t_{ramp-up}} \qquad \text{Eq. 53}$$

$$t_{ramp-up} = 3.084\ s \qquad \text{Eq. 54}$$

The dissipated energy by the resistive loop voltage can be calculated as follows:

$$E_{ramp-up\ resistive} = \int_{t_0}^{t_2} V_{pl-resistive,ramp-up} \cdot i_P(t)dt = 25.94 \cdot 20 \cdot 10^6 \cdot 3.084 \cdot 0.5 = 800\ MJ \qquad \text{Eq. 55}$$

The additional inductance of the plasma considered during the ramp-up can be replaced by an additional resistor characterized by the following resistance:

$$R_{pl,ramp-up} = \frac{E_{ramp-up\ resistive}}{\int_{t_0}^{t_2} i_P^2(t)dt} = \frac{3 \cdot 800 \cdot 10^6}{3.084 \cdot 4 \cdot 10^{14}} = 1.95\mu\Omega \qquad \text{Eq. 56}$$

4.4.3.2 Flat-top phase

During the flat-top phase the plasma resistance is:

$$R_{P,flat-top} = \frac{V_{P,flat-top}}{i_P(t_2)} = \frac{4}{20000000} = 0.2\ \mu\Omega \qquad \text{Eq. 57}$$

The minimum $i_{CS,st}$ that can be reached is -50 MA and considering that the plasma flat-top current is 20 MA, the minimum value of i_M is 30 MA. Therefore, the magnetizing current variation available during the flat-top is 45.812 MA and the magnetising flux variation during the flat-top is:

$$\Delta\Phi_{L_M,flat\ top} = \Delta i_{M,flat\ top} \times L_M = 45.813 \times 10^6 \times 8.12 \times 10^{-6} = 372\ Wb \qquad \text{Eq. 58}$$

The magnetizing flux at the end of the flat-top is:

$$\Phi_{L_M}(\mathrm{t}_3) = i_M(\mathrm{t}_3) \times L_M = -30 \times 10^6 \times 8.12 \times 10^{-6} = -243.6\ Wb \qquad \text{Eq. 59}$$

The flat-top duration is:

$$t_{flat-top} = \frac{\Delta\Phi_{L_M,flat\ top}}{V_{loop,flat\ top}} = \frac{372}{4} = 93\ s \qquad \text{Eq. 60}$$

Since the plasma current remains constant during the flat-top, the $i_{CS,st}$ variation is:

$$\Delta i_{CS,st,flat-top} = \Delta i_{M,flat-top} = -45.813\ MA \qquad \text{Eq. 61}$$

At the end of the flat-top $i_{CS,st}$ is:

$$i_{CS,st}(t_3) = i_{CS,st}(t_2) + \Delta i_{CS,st,flat-top} = -4.187 - 45.813 = -50\ MA \qquad \text{Eq. 62}$$

4.4.3.3 Ramp-down phase

The plasma magnetic flux variation during the ramp-down is:

$$\begin{aligned}\Delta\Phi_{P,ramp\ down} &= \Delta i_P \times L_{P,eq-ramp\ down} = (-20 \times 10^6) \times [(9.88) \times 10^{-6}] \\ &= -197.6\ Wb\end{aligned} \qquad \text{Eq. 63}$$

In this study the plasma current is decreased applying -90 V in the central solenoid, other strategies could be considered, for instance increase the plasma resistance with gas puffing. This last solution will lead to a lower variation of the magnetizing current, but the overall operating concept would remain valid. In the considered case, the time duration of the ramp down phase is:

$$t_{ramp\ down} = \frac{\Delta\Phi_{P,\text{ramp down}}}{V_{p,ramp\ down}} = \frac{-197.6}{-90} = 2.2\ s \qquad \text{Eq. 64}$$

The magnetizing current variation is:

$$\Delta i_M = \frac{-\Delta\Phi_{P,ramp\ down}}{L_M} = \frac{197.6}{0.00812} = 24.335\ MA \qquad \text{Eq. 65}$$

And the magnetizing current at the end of the ramp down is:

$$i_{M,end} = \mathrm{i}_{\mathrm{CS,st}} = -30 + 24.335 = -5.665\ MA \qquad \text{Eq. 66}$$

4.4.3.4 Recharge phase

During the recharge phase, the current in the CS coil has to be restored from ±5.665 kA to its nominal value (±50 kA) to have the maximum flux available in the following plasma pulse. The recharge phase has to be as short as possible to reduce the dwell time, which depends also by other systems that have to set up the reactor for the next pulse. The minimum time to recharge the CS when a voltage of 90 V is applied is:

$$t_{recharge} = \frac{8.12 \times 10^{-6} \times 44.335 \times 10^{6}}{90} = 4\ s \qquad \text{Eq. 67}$$

4.4.3.5 Calculated waveforms

In Figure 95 the calculated waveforms for i_P, i_M, $i_{CS,st}$ and v_C are reported. From these waveforms it is possible to design the MEST system applied to PILOT CS.

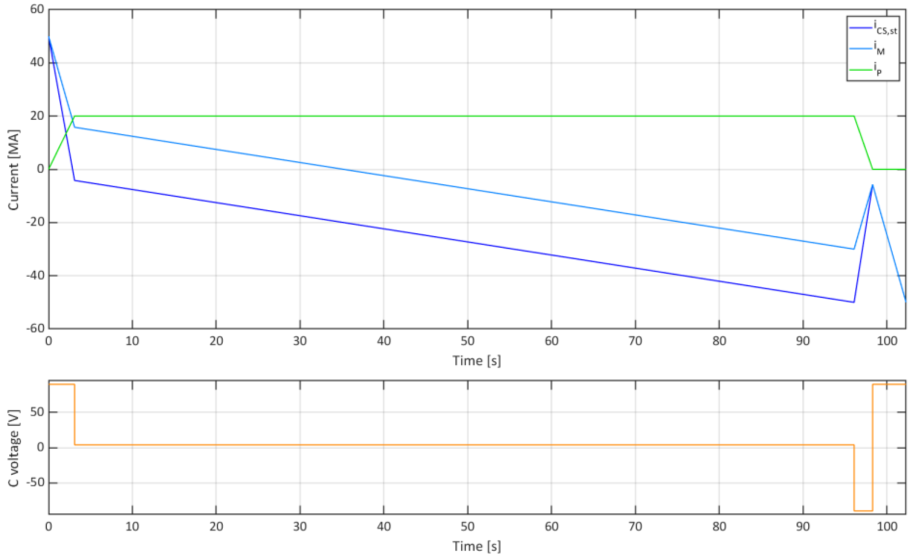

Figure 95 - Calculated i_P, i_M, $i_{CS,st}$ and v_C during PILOT pulse

The details of each pulse phase are reported below:

- Ramp-up (t_0-t_2):
    - Duration: 3.1 s
    - i_{CS} (t_0)=50 kA
    - magnetizing flux(t_0)=407 Wb
    - i_{CS} (t_2)= -4.2 kA
    - magnetizing flux(t_2)=128.4 Wb
    - v_C(from t_0 to t_2)= -90 kV
- Flat-top (t_2-t_3):
    - Duration: 93 s
    - i_{CS} (t_3)=-50 kA
    - magnetizing flux(t_3)=-243.6 Wb
    - v_C(from t_2 to t_3)=-4 kV
- Ramp-down(t_3-t_4):
    - Duration=2.2 s
    - i_{CS} (t_4)=-5.7 kA
    - magnetizing flux(t_4)=-46 Wb
- Recharge (t_5-t_6):
    - Duration: 4 s
    - i_{CS} (t_5)=-5.7 kA
    - magnetizing flux(t_5)=-46 Wb
    - i_{CS} (t_6)=-50 kA
    - magnetizing flux(t_6)=-407 Wb
    - v_C(from t_5 to t_6)=90 kA

4.4.4 Power supply design

After the calculation of the trends of the main quantities in the CS circuit and the plasma the PS can be designed. The PS, fed by the distribution network, is connected in series with KC to compensate the energy dissipated by the plasma during the discharge and the losses in the system. In this first application study, the PS is considered a unidirectional thyristor converter.

All the following calculations are made considering the energy dissipated in the plasma as the only dissipation, neglecting the power losses in all the circuit components. Multiplying i_{CS} and v_C it is obtained the power supplied to the CS, shown in Figure 96. The energy in the figure is obtained integrating the CS power during the pulse.

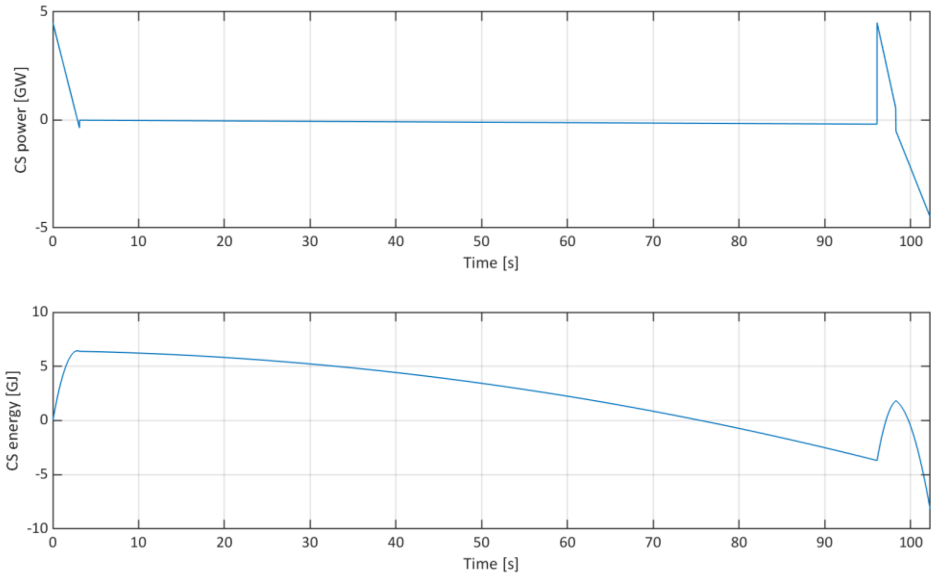

Figure 96 – CS power and energy during the pulse

At the end of the discharge the CS energy is -8.3 GJ higher than the initial value (0 J) therefore the converter has to compensate this energy during the pulse.

With the control strategy described in section 4.1.2 the converters will operate varying its output voltage to maintain constant the system energy. Studying this application, the minimization of the active and reactive power required from the grid by the PS has been achieved trying to operate the thyristor converter at its maximum power (i.e. at its minimum firing angle for the thyristors) during all the pulse. Considering the total energy dissipated during the pulse (8.3 GJ), the mean dissipated power dissipated is:

$$P_{PS\,mean} = \frac{8.3 \times 10^9}{t_6} = \frac{8.8 \times 10^9}{102.3} = 86.02\,MW \;\cong 86\,MW \qquad \textit{Eq. 68}$$

Since the power of the thyristor converter varies with i_{KC}, if the firing angle is kept constant to its minimum value, the DC voltage supplied by the converter can be estimated considering the mean value of i_{KC} during the pulse (Figure 91, in which is considered a perfect compensation by PS to maintain constant the system energy), that is equal to 66.8 kA:

$$V_{PS} = \frac{P_{PS\,mean}}{63700} = \frac{86 \times 10^{6}}{66800} = 1287.7\ V \cong 1288\ V \qquad \textit{Eq. 69}$$

Assuming a minimum firing angle of 15°, the RMS phase-to-phase voltage at the converter AC side is (neglecting the transformer voltage drop):

$$V_{LL} = \frac{V_{conv}}{1.35 \times \cos{(15°)}} = \frac{1288}{1.35 \times \cos{(15°)}} = 987.7\ V\ \cong 1000\ V \qquad \textit{Eq. 70}$$

With this converter design that considers only the mean power dissipated by the plasma, the converter control maintains the thyristors firing angle at its minimum value during all the pulse and the reactive power exchanged with the grid is kept at its minimum value. Otherwise, adopting a PS rated for an higher power to cope with possible plasma instabilities to control, will cause an higher reactive power exchanged with the grid when the PS operates at a power level lower than the maximum one. Knowing main currents and voltage waveforms during the pulse (see section 974.4.3.5), the maximum energy stored by the system during the pulse can be calculated and the energy stored by LC, C, the plasma and their sum are reported in Figure 97. From this calculations the maximum energy stored by the system during the pulse results 10.16 GJ at the end of LC charge and at the end of the flat-top.

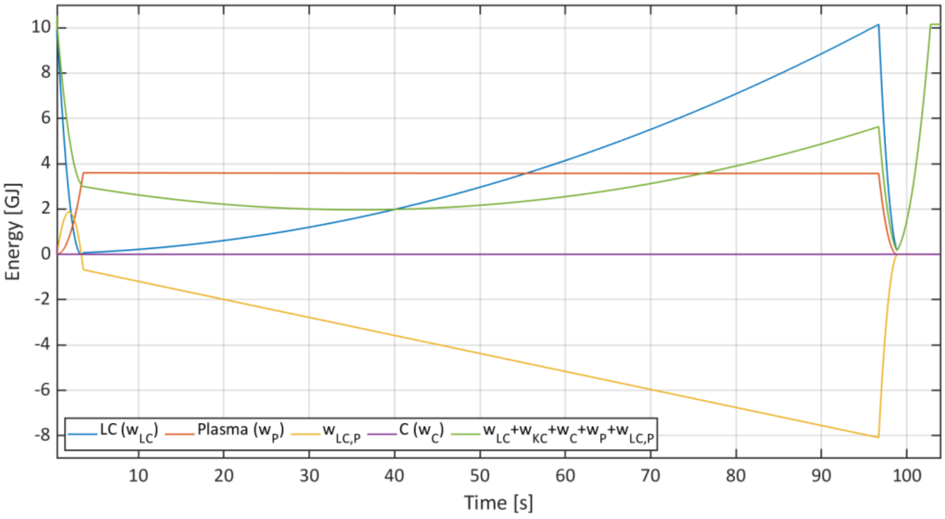

Figure 97 – Calculated w_{LC}, w_P, $w_{LC,P}$, w_C and their sum during PILOT pulse

Knowing W_T the maximum current on KC during the pulse (considering $L_{LC}=L_{KC}$), and on PS, can be calculated as follow:

$$I_{KC,max} = \sqrt{\frac{W_T}{L_{KC}}} = \sqrt{\frac{2 \cdot 2 \cdot 10.16 \cdot 10^9}{8.12}} = 70.746\ kA \qquad \text{Eq. 71}$$

4.4.5 Capacitor bank design

The capacitance of the capacitor bank is designed using Eq. 34, considering the double-leg switching strategy (section 4.1.1.2), and evaluating the maximum switching frequency during the calculated scenario in section 4.4.3.5. In Figure 98 are shown the switching frequencies for different values of C capacitance. As trade-off between dynamic performances and switching losses of the semiconductor switches and considering the power level of this application, a reasonable limit of 500 Hz for the switching frequency has been tentatively assumed. Therefore, the C capacitance value chosen is 1 mF. These computed values of switching frequency will be compared with the one resulting from numerical simulation in section 4.4.6.

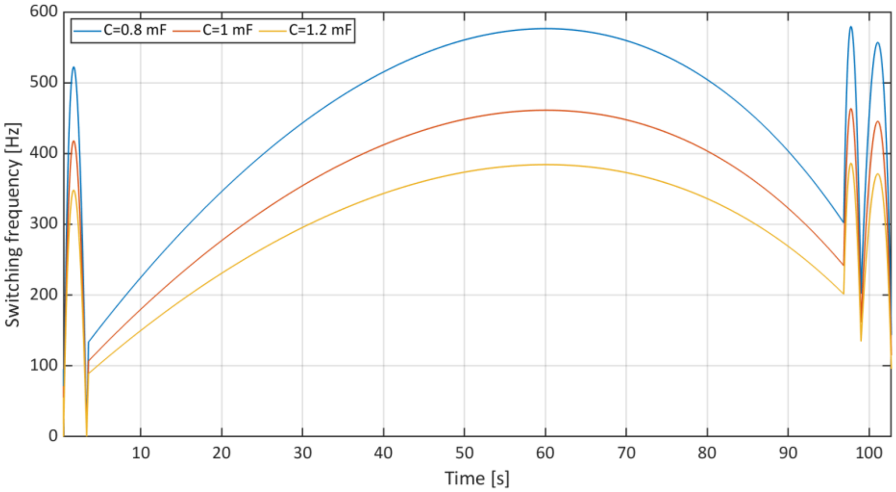

Figure 98 – Switching frequency for a swipe of i_{CS} from 50 kA to -50 kA for different values of C capacitance.

Considering a constant half hysteresis band value, equal to 9 kV (10% of C rated voltage), the total energy stored in the capacitor banks is:

$$W_{C,max} = \frac{1}{2} C V_{C,max}^2 = 0.5 \cdot 1 \cdot 10^{-3} \cdot (99 \cdot 10^3)^2 = 4.9\ MJ \qquad \text{Eq. 72}$$

The maximum energy stored by KC is:

$$W_{KC,max} = \frac{1}{2} \cdot L_{LC} \cdot i_{LC,max}^2 \cdot 2 = 8.13 * (50 \cdot 10^3)^2 = 20.3\ GJ \qquad \text{Eq. 73}$$

The ratio between the maximum energy stored in KC and the maximum energy stored in C is higher than 4000. Therefore, with the adopted design it is possible to reach a ration between the maximum energy stored in KC and the maximum energy stored in C higher than 1000.

The voltage rating of the capacitor bank and the MEST energy transfer system of each CS sector is 15 kV. The resulting capacitance of each sector is.

$$C_{sector} = \frac{W_{C,max}}{6} \cdot \frac{2}{V_{CS-sector,max}^2} = \frac{4.9 \cdot 10^6}{6} \cdot \frac{2}{(16.5 \cdot 10^3)^2} = 6\ mF \qquad \text{Eq. 74}$$

Where $V_{CS\text{-}sector,max}$ is the maximum voltage of the CS sector capacitor that is 15 kV plus 1.5 kV to consider half of the hysteresis band.

4.4.6 Simulation results

The operation of the circuit in Figure 92 has been reproduced using the numerical model reported in section 4.3. The simulation parameters are reported in Table 9.

Table 9 – Simulation parameters of MEST model applied to CS PILOT

Parameters	Value
$L_{LC} = L_{KC}$	8.21 H
C capacitance	1 mF
Plasma current	20 MA
Plasma loop voltage (flat-top)	4 V
Central Solenoid rated current ($I_{CS,max}$)	± 50 kA
Max v_C	± 90 kV
Hysteresis band	± 9 kV
Turns of the Central Solenoid(N)	1000
Plasma inductance (ramp-up)	22 µH
Plasma inductance (flat-top, ramp-down)	18 µH
Switching frequency limit	500 Hz
Switching pattern	Double-leg

Figure 99 shows plasma, CS and KC currents resulting from the numerical simulations while Figure 100 reports C voltage and the magnetizing flux. All the simulation results are compatible with the analytical calculation made in section 4.4.2 and confirm the design choices.

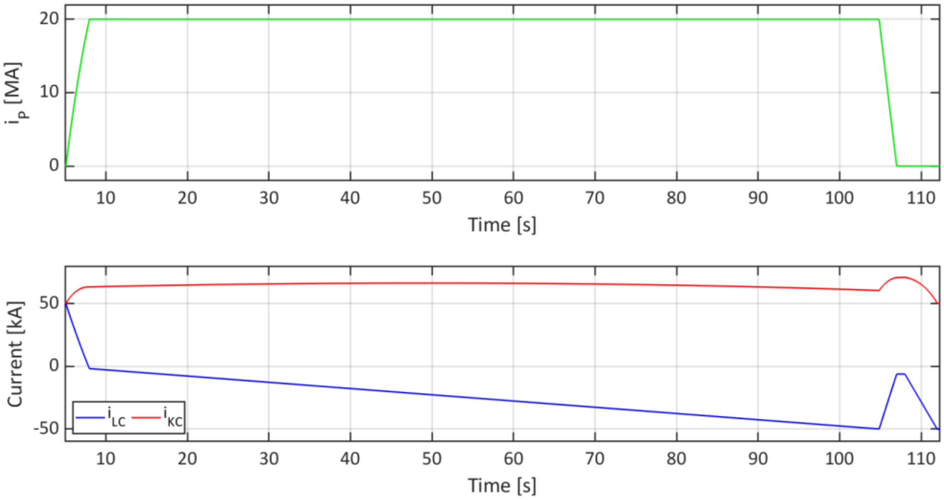

Figure 99 – Plasma current, i_{CS} and i_{KC} resulting from numerical simulation of MEST applied to PILOT CS

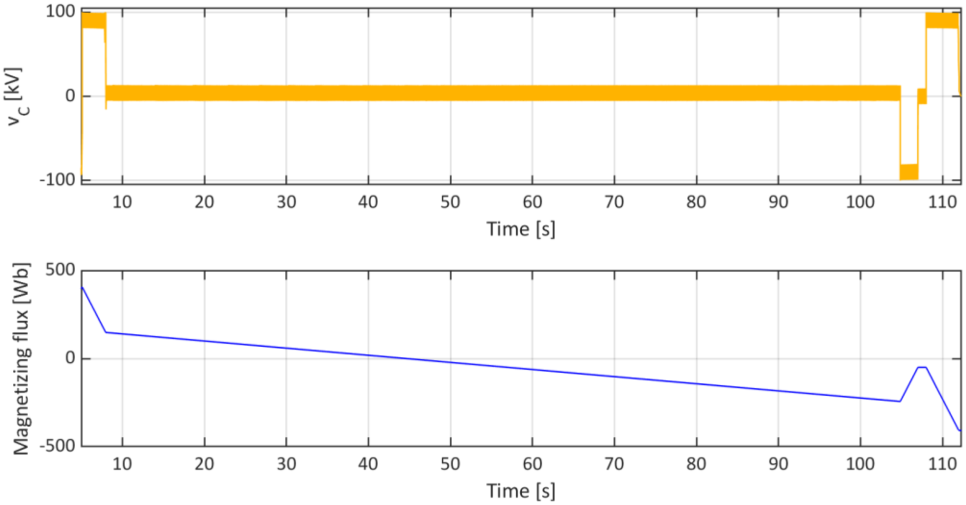

Figure 100 – v_C and magnetizing flux resulting from numerical simulation of MEST applied to PILOT CS

KC current does not follow the $i_{KC,ref}$ coming from a perfect losses compensation by the PS, as can be seen in Figure 101. This happens because the PS does not compensate instantly the power supplied to the plasma, allowing a decoupling also between plasma dissipated power and the grid. In fact, in section 4.4.4, the PS has been rated for the mean losses during the pulse.

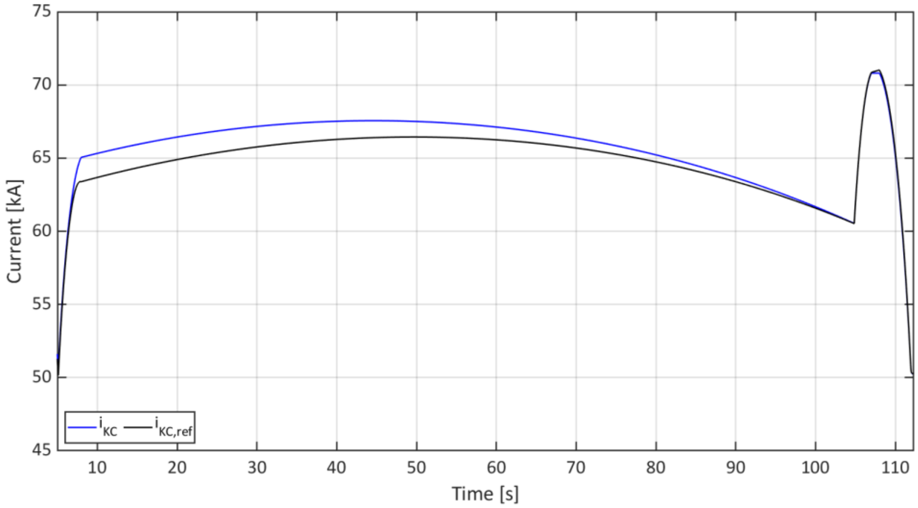

Figure 101 – i_{KC} and $i_{KC,ref}$ resulting from numerical simulation of MEST applied to PILOT CS

In Figure 102 the grid active and reactive power are reported. The firing angle of the thyristor converter that compose the PS remain constant at the minimum value (i.e. 15 degrees) during all the plasma pulse. This means that the i_{KC} current control, as explained in 4.1.2, gives the current reference $i_{KC,ref}$ to maintain the system total energy constant during the pulse, but, thanks to the PS design and control, the power losses are not instantly compensated flattening the power required from the grid along the whole pulse time. This behaviour allows minimizing the reactive power exchanged with the grid and the active and reactive power fluctuations depends only on the variation of i_{KC}. This is a first tentative design of the PS that shows the achievable results in flattening the active power and in reducing the reactive power exchanged with the grid. A margin on the PS power rating should be taken in consideration during the design of the PS if non-predictable active power request are foreseen during a pulse (for instance plasma instability control).

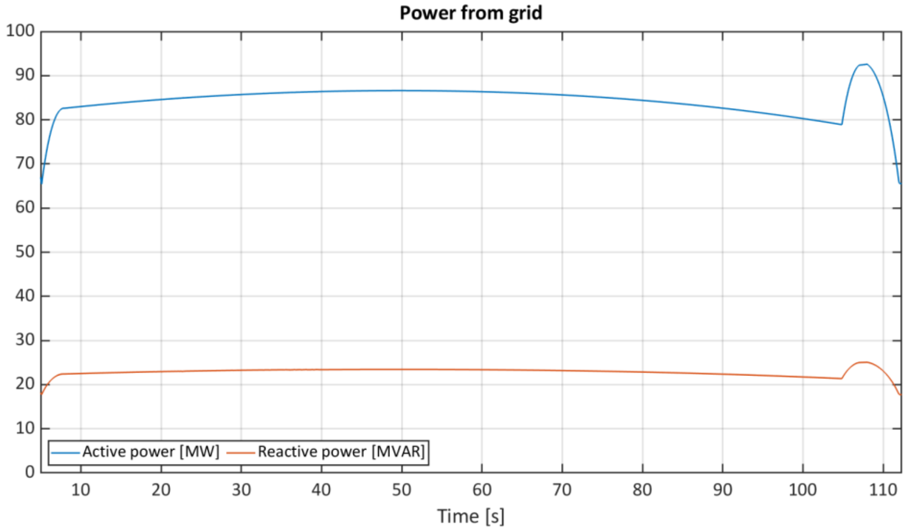

Figure 102 – Active and reactive power exchanged with the grid resulting from numerical simulation of MEST applied to PILOT CS

Figure 103 shows a comparison between the power supplied to the CS by the MEST system, obtained multiplying v_C and i_{CS}, and the active power absorbed from the grid. The power supplied to the CS reaches peaks around 5 GW while the power required from the grid remains always lower than 100 MW, validating the decoupling between grid and CS operated by the MEST system. This result shows how the power required to have fast magnetic flux variations is much higher that the power dissipated by the plasma. Achieving this magnetic flux variation without dissipation on the SNUs it's crucial to increase the system efficiency in the PILOT reactor that can operate with relatively short plasma pulses.

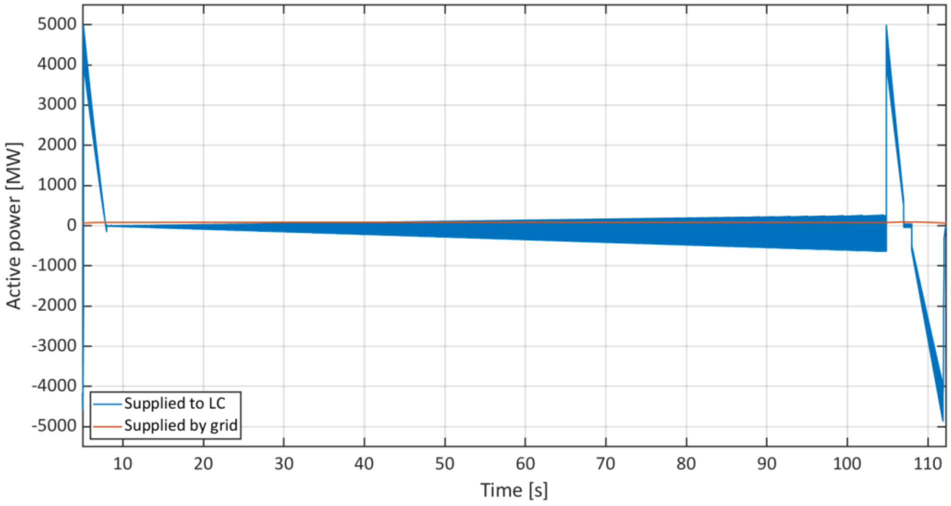

Figure 103 – Comparison between active power supplied to PILOT CS and active power supplied by the grid resulting from numerical simulation of MEST applied to PILOT CS

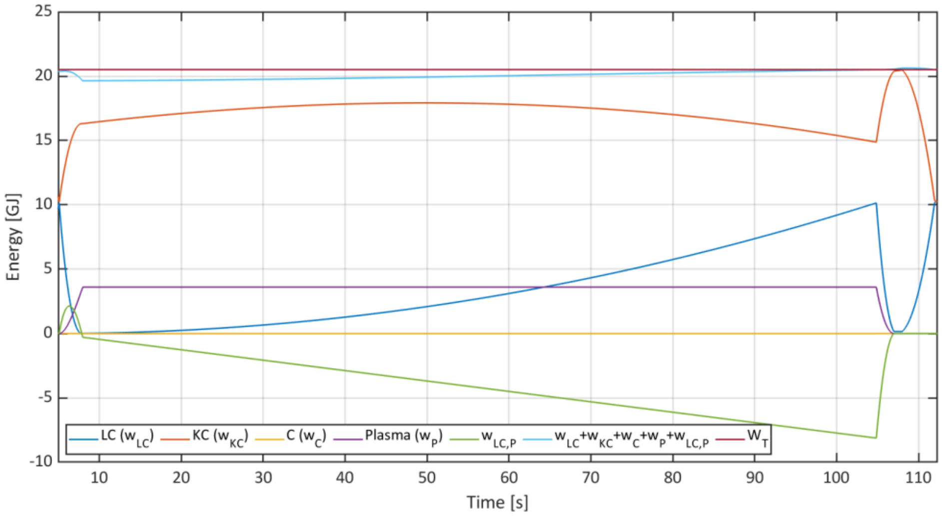

Figure 104 – Comparison between LC, KC, C, plasma energies and their sum with W_T resulting from numerical simulation of MEST applied to PILOT CS

Figure 105 shows the switching frequency of the four switches during the simulated pulse. As can be seen, the frequency remains under 500 Hz confirming the design of the capacitor bank. The switching frequencies of the four switches are the same during the whole pulse and that can be explained by the fact that the commutations are distributed between all four switches thanks to the double-leg switching strategy. A comparison between the switching frequencies between the double-leg and the single-leg switching strategy can be found in section 4.5.2.2.

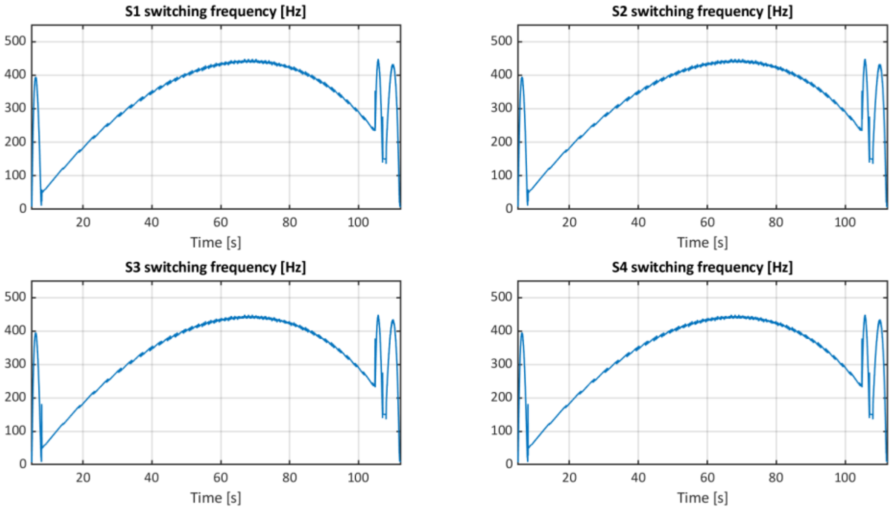

Figure 105 – Switching frequency of the four switches resulting from numerical simulation of MEST applied to PILOT CS

In Figure 106 a comparison between the switching frequency measured during the numerical simulation and the one calculated with Eq. 34 is reported. This comparison confirm the validity of Eq. 34 besides its simplifying hypotheses. The gaps between the two curves are mainly due to the aforementioned assumptions and the time step of the discrete-time numerical simulation (10 µs) that introduces a delay in the switches control.

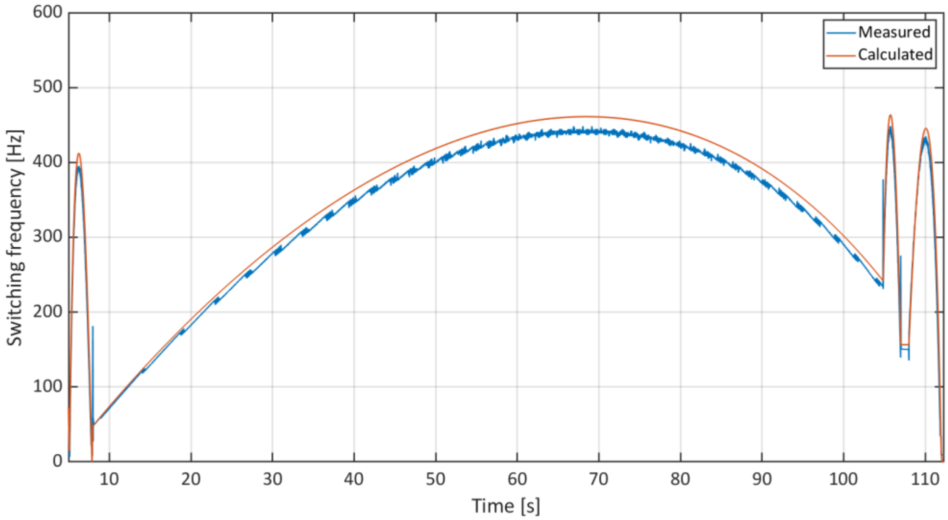

Figure 106 – Measured and calculated S1 switching frequency resulting from numerical simulation of MEST applied to PILOT CS

4.5 MEST applied to EU DEMO

From the operational point of view, the MEST could solve both the FDU (only for LC) and the SNU functions, as shown in the following sections. Future studies will be crucial to understand and evaluate which solution is the most convenient, considering the final requirements in term of current and voltage waveforms, the reliability of the overall Coils Power Supply (CPS) system and all the fault analysis and protection strategies which increases in complexity together with the increasing number of subsystems in the CPS system.

The first outline of a CS circuit of DEMO supplied by the MEST system has been tentatively depicted in Figure 107 with the MEST system supplying the coils and maintaining, on the contrary, the ITER-like approach for the Switching Network Units (SNUs), the FDUs and the earthing circuits. The SNUs are, basically, resistors with circuit breaker and making switch in parallel. Their aim is to produce the additional voltage required at plasma breakdown and ramp-up. The Fast Discharge Units (FDUs), instead, are protecting devices able to completely discharge the coils in case of quench or other abnormal conditions. It is assumed that the CS magnet is divided in 6 sectors (CS1U, CS1L, CS2U, CS2L, CS3U, CS3L) and CS1U and CS1L are connected in series, since their currents are identical (as in ITER), interleaved with the respective power supplies, SNUs and FDUs to equally distribute the voltage to ground. The other CS coils circuits, in series with their SNU and FDU, are fed by the respective power supply, independently.

The ITER-like topology has been considered for the coil earthing circuit, which is made of two terminal-to-neutral resistors R_{TN} and one neutral-to-ground resistor R_{NG}. With this earthing circuit topology, the middle point of the coil is virtually at ground potential halving the potential of the two coil terminals-to-ground with respect the total voltage applied to the coil.

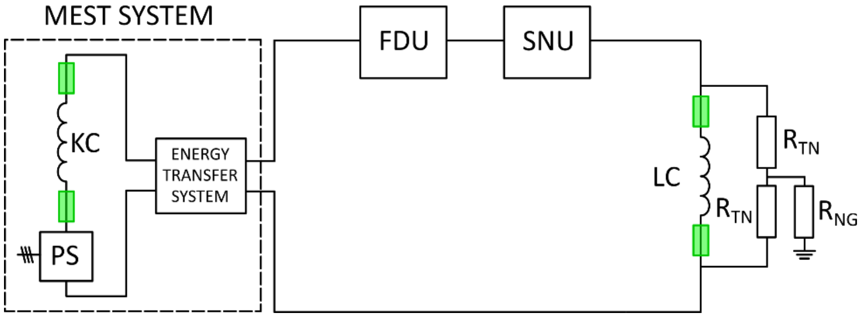

Figure 107 - Scheme of the coil power supply circuit for CS3U, CS2U, CS2L, CS3L, PF1 and PF6 coils.

As studied in [14], the MEST can support the operation of the CS sectors or the PF coils; this application study is addressed to verify its capability to provide the LC voltage and current waveforms necessary for plasma ignition and control by regulating the capacitor voltage and transferring the energy between KC and LC. The MEST system design involves also the evaluation of the number of parallel components per equivalent switch needed and the estimation of area occupancy. This allows a comparison of the MEST system with other technologies to supply the main SC coils in DEMO in terms of requirements of space.

The MEST operation applied to DEMO is divided in 5 phases, three of them cyclically repeated and related to the DEMO pulse phases, shown in Figure 108 where a simplified typical current waveform of a CS sector is reproduced:

- **KC pre-charge**: considering that i_{KC} shall always be greater than $|i_{LC}|$, the KC is pre-charged by the PS at the current value $i_{KC,\,max}$. The energy stored in KC, when its current varies from $i_{KC,max}$ and $i_{LC,max}$ (maximum value of i_{LC} during the pulse), corresponds to the maximum energy stored in LC during the plasma pulse. Therefore, KC is pre-charged at least up to twice the maximum energy expected in LC, depending on the inductance values of KC. If $L_{KC} \leq L_{LC}$, KC is pre-charged up to twice the maximum energy expected in LC while, if $L_{KC} > L_{LC}$, KC is pre-charged up to more than twice the maximum energy expected in LC (because of the constrain $i_{KC}>|i_{LC}|$).
- **LC charge**: transferring energy from KC to LC the current of LC is pre-charged to its initial value ready for the pulse to begin.
- **Pulse**: during the plasma pulse, the energy is transferred between KC and LC. The considered pulse is divided in ramp-up (the first part of which is the plasma breakdown), flat top and ramp-down. During ramp-up LC has to provide a magnetic flux variation needed for plasma ignition and for plasma current rise up to the flat-top value. To achieve this task, LC current decreases and LC energy is transferred from LC to KC, where it is stored. When becomes negative (during the last part of ramp-up or during the flat-top) KC releases its stored energy to LC to fulfil magnetic flux variation. During ramp-down LC recovers part of the plasma energy which is transferred to the KC.
- **LC discharge**: LC is discharged and its energy is recovered in KC. Then, the phase 1 could take place.

- **KC discharge:** if is foreseen a reactor shutdown, KC will be discharged. In this last case KC energy will be dissipated or transferred to the grid depending on the PS technology.

In principle, the MEST can be designed for the total needed voltage, thus avoiding the use of SNUs. This could represent a smart design solution but implies a significant increase of the ratings of the MEST system which would mean a higher number of semiconductor switches and an increase of the capacitor bank voltage.

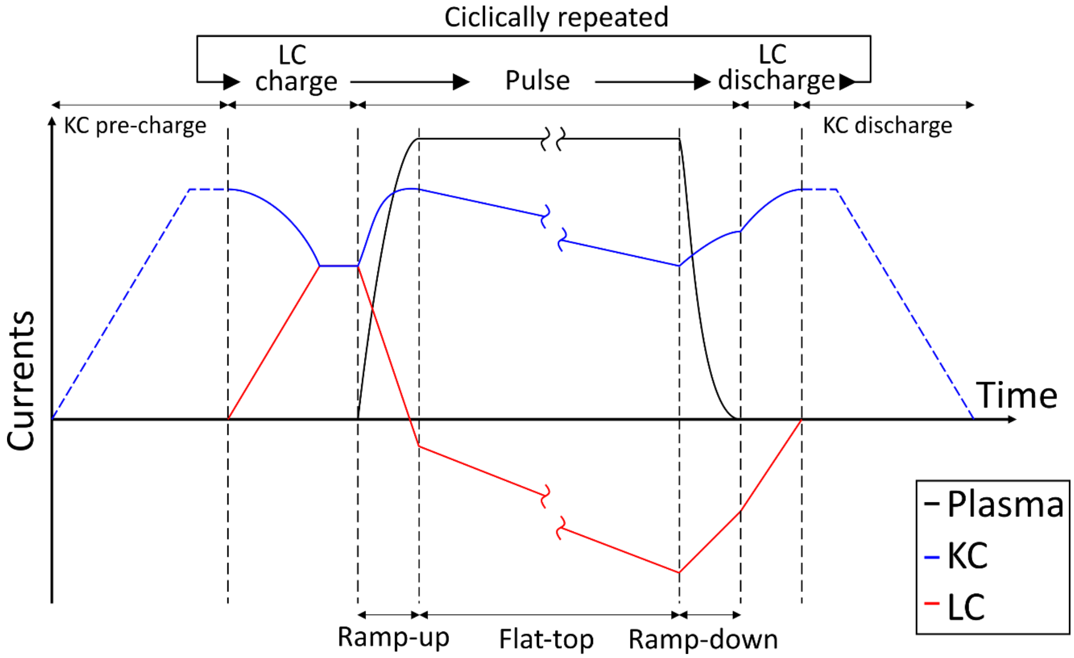

Figure 108 – Typical current waveform of a CS sector

Another very important aspect to be studied for the MEST integration in the circuit is related to the fast discharge of the SC coils, both the load and the sink ones. In principle, the MEST should be capable to fast discharging the LC in case of quench with the required time constant; in that case just a backup Fast Discharging Unit (FDU) could be provided. However, this aspect needs to be deeply investigated also considering the very high reliability level required to FDUs. In addition, suitable provisions to fast discharge also the sink coil has to be studied in detail.

4.5.1 MEST components design for EU DEMO

In the following sections is studied the application of the MEST system to one circuit of EU DEMO Central Solenoid (CS).

The ratings of DEMO base converters are tentatively outlined in [12]; they are recalled in Table 10 and compared with the ITER base converters ratings.

Table 10 - Tentative configuration of magnet base converters and comparison with ITER

Name	Load	On-load voltage rating [kV]	Current rating [kA]	ITER on-load voltage rating [kV]	ITER current rating [kA]
CS1-PS-U	CS1U	±8	±45	±2.1	±45
CS1-PS-L	CS1L	±8	±45	±2.1	±45
CS2-PS-U	CS2U	±8	±45	±2.1	±45
CS2-PS-L	CS2L	±8	±45	±2.1	±45
CS3-PS-U	CS3U	±8	±45	±2.1	±45
CS3-PS-L	CS3L	±8	±45	±2.1	±45
PF1-PS	PF1	±8	±45	±2.1	±55
PF2-PS	PF2	±10	±45	±3.15	±55
PF3-PS	PF3	±10	±45	±3.15	±55
PF4-PS	PF4	±10	±45	±3.15	±55
PF5-PS	PF5	±10	±45	±3.15	±55
PF6-PS	PF6	±8	±45	±2.1	±55

The maximum voltage on coils including the voltage from the main converters and switching networks is 10kV. In the following subsections, will be reported and discussed a tentative design of the MEST system components applied to DEMO CS3U circuit.

For this first tentative design for the MEST system applied to DEMO CS3U circuit the following assumption are considered:

- Fixed half hysteresis band amplitude w=1000 V;
- The rated load current is 45 kA, thus i_{LC} varies from +45 kA to -45 kA;
- $L_{LC}=L_{KC}=2.07$ H as reference but some considerations are done also for $L_{KC}=2L_{LC}$.

4.5.1.1 Capacitor bank design

The value of the capacitance C is defined using Eq. 34, considering the double-leg witching strategy (section 4.1.1.2), considering $v_{C,ref}=0$ which is the worst case for the switching frequency (see section 4.2.3) and varying i_{LC} from +45 kA to -45 kA. In the Table 11 are reported the value of C to maintain the switching frequency under the imposed limits (300 Hz, 400 Hz and 500 Hz are considered) and are also reported the capacitance values for $L_{KC}=2L_{LC}$.

Table 11 – Minimum capacitance value at different f_{sw} limits

	f_{sw} limit [Hz]	C [mF]
$L_{KC}=L_{LC}$	500	7.2
	400	9.0
	300	12.0
$L_{KC}=2L_{LC}$	500	6.6
	400	8.2
	300	11.0

4.5.1.2 Considered semiconductor devices

Two different IGCTs will be considered: ABB® 5SHY42L6500 [31] which has higher V_{DRM} (less series IGCTs per equivalent switch are needed) but higher conduction and switching losses and ABB® 5SHY35L4521 (Annex 1) which has lower V_{DRM} but also lower conduction and switching losses (lower parallel connected IGCTs per equivalent switch are needed).

The selected IGCTs are asymmetric devices and the MEST system, which can be considered as a current source converter for the component behaviour, they have to block both forward and reverse voltage. The reverse voltage block capability of asymmetric IGCTs is in the order of some tens of volt therefore a series connected diode is needed for each IGCT. For the diode connected in series with the IGCTs, to withstand the reverse voltage, the ABB® 5SDF20L4520 [32] is considered, which has higher conduction losses but lower switching losses than the ABB® 5SDF28L4520.

The relevant characteristics of the considered semiconductor devices are reported in the following sections.

4.5.1.2.1 IGCT terminology and transient waveforms

Table 12 and Figure 109 reports the IGCTs terminology and transient waveform respectively.

Table 12 – IGCTs terminology

V_D	Device commutation voltage/static on-state voltage.
I_T	Constant forward load current
I_{TGQM}	Maximum current that the IGCT can turn-off
di_T/dt	The rate of rise of the forward load current
V_{DSP}	The first peak of the IGCT () direct voltage during the turn-off; depends upon its characteristics and stray inductances.
V_{DM}	Max. device voltage. The second peak of the IGCT transient voltage during the switch-off; depends upon external clamp circuit.
CS	The electrical command signal sent to the gate unit
SF	The electrical status-feedback signal (opposite to CS during the normal operation)
t_{don}	Turn-on delay time
t_{donSF}	Turn-on status-feedback time
t_{doff}	Turn-off delay time
t_{doffSF}	Turn-off status-feedback time
t_r	Anode voltage fall time

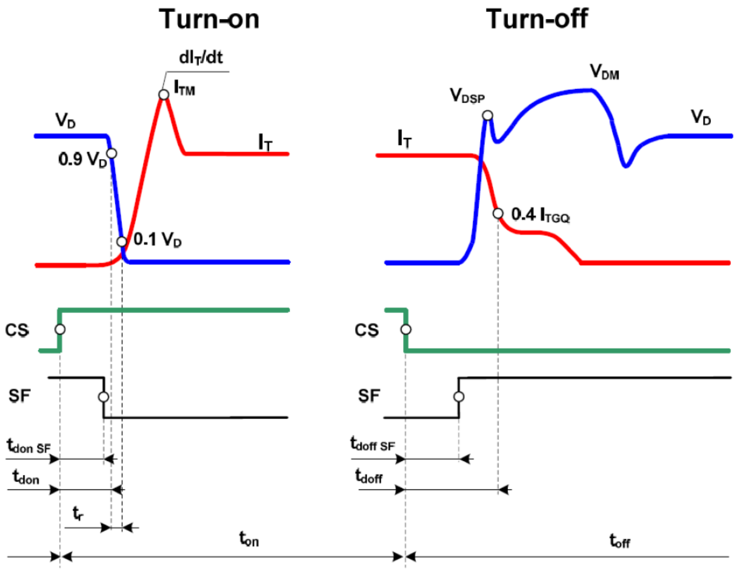

Figure 109 – Typical IGCT transient waveforms [33]

The main characteristics of the selected IGCTs are reported in Table 13 and Table 14.

Table 13 – IGCT ABB® 5SHY42L6500 ratings [31]

	Symbol	Conditions	Max
Rep. peak off-state voltage	V_{DRM}		6500 V
Permanent DC voltage for 100 FIT failure rate of GCT	V_{DC}		4000 V
Reverse voltage	V_{RRM}		17 V
On-state voltage	V_T	I_T=3800 A, T_j=125°C	4 V
Threshold voltage	$V_{(T0)}$	I_T=1000..3800 A, T_j=125°C	1.88 V
Slope resistance	r_T		0.56 mΩ
Max. controllable turn-off current	I_{TGQM}	V_{DM} ≤V_{DRM}, T_j=125°C	3800 A
Turn-on energy per pulse	E_{on}	V_D=4000 V, T_j=0..125°C	3.1 J
Turn-off energy per pulse	E_{off}	V_D=4000 V, T_j=0..125°C	44 J
Turn-on delay time	$t_{d(on)}$	V_D=4000V, I_T=3800 A, T_j=0..125°C	4 µs
Turn-off delay time	$t_{d(off)}$	V_D=4000V, T_j=0..125°C	8 µs
Optical control input/output			
Min. on-time	t_{on}		40 µs
Min. off-time	t_{off}		40 µs
Thermal			
Junction operating temperature	T_{vj}		125°C
Thermal resistance junction-to-case	$R_{th(j-c)}$	Double side cooled	8.5 K/kW

Thermal resistance case-to-heatsink of GCT	$R_{th(c-h)}$	Double side cooled	3 K/kW

Table 14 – IGCT ABB® 5SHY35L4521 ratings (Annex 1)

	Symbol	Conditions	Max
Rep. peak off-state voltage	V_{DRM}		4500 V
Permanent DC voltage for 100 FIT failure rate of GCT	V_{DC}		2800 V
Reverse voltage	V_{RRM}		17 V
On-state voltage	V_T	I_T=4000 A, T_j=125°C	2.7 V
Threshold voltage	$V_{(T0)}$	I_T=1000..4000 A, T_j=125°C	1.4 V
Slope resistance	r_T		0.325 mΩ
Max. controllable turn-off current	I_{TGQM}	$V_{DM} \leq V_{DRM}$, T_j=125°C	4000 A
Turn-on energy per pulse	E_{on}	V_D=2800 V, T_j=0..125°C	1.4 J
Turn-off energy per pulse	E_{off}	V_D=2800 V, T_j=0..125°C	22 J
Turn-on delay time	$t_{d(on)}$	V_D=2800V, I_T=4000 A, T_j=125°C	3.5 µs
Turn-off delay time	$t_{d(off)}$	V_D=2800V, T_j=0..125°C	7 µs
Optical control input/output			
Min. on-time	t_{on}		40 µs
Min. off-time	t_{off}		40 µs
Thermal			
Junction operating temperature	T_{vj}		125°C
Thermal resistance junction-to-case	$R_{th(j-c)}$	Double side cooled	8.5 K/kW
Thermal resistance case-to-heatsink of GCT	$R_{th(c-h)}$	Double side cooled	3 K/kW

The main characteristics of the selected diode are reported in Table 15.

Table 15 – Diode ABB® 5SDF20L4520 ratings [32]

	Symbol	Conditions	Max
Rep. peak reverse voltage	V_{RRM}	T_{vj}=140°C	4500 V
Permanent DC voltage for 100 FIT failure rate	$V_{DC-link}$	100% duty	2800 V
On-state voltage	V_F	I_F=3300 A, T_{vj}=140°C	4.2 V
Threshold voltage	$V_{(F0)}$	I_T=500..3500 A, T_{vj}=140°C	1.56 V
Slope resistance	r_F		0.80 mΩ
Turn-off energy	E_{off}	$V_{DC-link}$=2800V, I_{FQ}=3300 A, T_j=140°C	13 J
Thermal			

Operating junction temperature	T_{vj}		140°C
Thermal resistance junction-to-case	$R_{th(j-c)}$	Double side cooled	6 K/kW
Thermal resistance case-to-heatsink of GCT	$R_{th(c-h)}$	Double side cooled	3 K/kW

4.5.1.2.2 Steady state thermal analyses

The thermal analyses of the IGCTs and diode permits to evaluate the number of parallel components per equivalent switch needed to maintain the junction virtual temperature T_{vj} within the limit imposed by the manufacturer. For the thermal analyses, the most stressful operating condition for the components should be considered. Since for the considered IGCTs the conduction losses are lower with respect the switching losses (also considering the lower frequency limit of 300 Hz as can be seen in section 4.5.1.4), the worst case is when the switching frequency reaches its maximum value. The thermal analyses are made considering $L_{LC}=L_{KC}$.

4.5.1.3 General formulae of steady state thermal analyses

In the thermal analysis, the considered diode and IGCTs cooling water temperature is supposed equal to 35°C and a margin of 15°C is taken with respect to the maximum junction temperature. With these assumptions, the maximum over temperatures on the junction of the two components are:

- IGCT: $\Delta T_{MAX}=T_{vj}-15-35=125-50=75$ K;
- diode: $\Delta T_{MAX}=T_{vj}-15-35=140-50=90$ K.

To calculate the over temperature in relation with the number of parallel components (N_P), the following equations are used.

The conducting losses can be calculated as follows, where I_{AV} and I_{RMS} are the average current and the RMS current of the switch, respectively:

$$P_{CON} = V_{TO}\left(\frac{I_{AV}}{N_P}\right) + r_T\left(\frac{I_{RMS}}{N_P}\right)^2 \tag*{Eq. 75}$$

The switch-on losses can be calculated as follows:

$$P_{SW_{ON}} = E_{ON} f \frac{V_D}{V_{DC}} \frac{\sum I_{COMM,ON}}{I_{TGQM}} \frac{1}{N_P} \tag*{Eq. 76}$$

while this formula is valid for the switch-off losses:

$$P_{SW_{OFF}} = E_{OFF} f \frac{V_D}{V_{DC}} \frac{\sum I_{COMM,OFF}}{I_{TGQM}} \frac{1}{N_P} \qquad \text{Eq. 77}$$

where E_{ON}, E_{OFF}, V_{DC} and I_{TGQM} are specified in the data-sheets [31], Annex 1 and [32] and reported in Table 13, Table 14 and Table 15. f is the considered frequency to evaluate the losses and will be equal to f_{SW}, limit and $I_{COMM,ON}$ and $I_{COMM,OFF}$ are the current commutated at each switch-on or switch-off respectively. The multiplication factor highlighted in blue in Eq. 76 scales the switching losses E_{ON} with the direct voltage applied to the switch, while the multiplication factor highlighted in red scales E_{ON} with the commutation current of the component. The same factors can be found in Eq. 77.

The total losses are calculated as follows:

$$P_{TOT} = P_{CON} + P_{SW_{ON}} + P_{SW_{OFF}} \ [W] \qquad \text{Eq. 78}$$

The over-temperature can be calculated considering the thermal resistances of the component and of the heat-sink:

$$\Delta T = \left(R_{th(j-c)} + R_{th(c-h)} + R_{th(h-s)}\right) P_{TOT} \ [K] \qquad \text{Eq. 79}$$

Where $R_{th(j-c)}$ can be found in Table 13, Table 14 and Table 15. $R_{th(h-s)}$ is derived from RFX-mod power supply system and it is considered equal to 5 Ω.

4.5.1.4 IGCTs and diodes over-temperature

As explained in section 4.2.3 the IGCT maximum over-temperature occurs with $i_{LC}/I_{LC,max}$ = 0.584 (considering L_{LC}=L_{KC}) and this corresponds to i_{LC}=26280 A and i_{KC}=57960 A with a duty cycle of 55%. The parallel connection of several devices will leads to a current unbalancing between the parallel branches. The current unbalance depends on the devices characteristics, control, temperature and position in the system layout; several design solution could be adopted to lower the impact of this phenomenon but considering the high number of parallel-connected devices it has to be taken into account in the following thermal analyses. The factor cs=1.2 takes into account the maximum current unbalance between parallel components this value has been assumed considering the results achieved on ITER PF converter bridge prototype [34] and reasonable future improvements.

Figure 110 shows the considered equivalent IGCT and diode current waveform with f_{sw}=500 Hz; its average value is I_{AV}=38250 A, while the RMS value is I_{RMS}=51580 A and I_{COMMON}= $I_{COMMOFF}$= 69552 A. Table 16 reports the results of the thermal analyses of the considered IGCTs and series connected diodes, in which the number of parallel connected switches N_P is calculated to maintain the over-temperature within the previously defined limit.

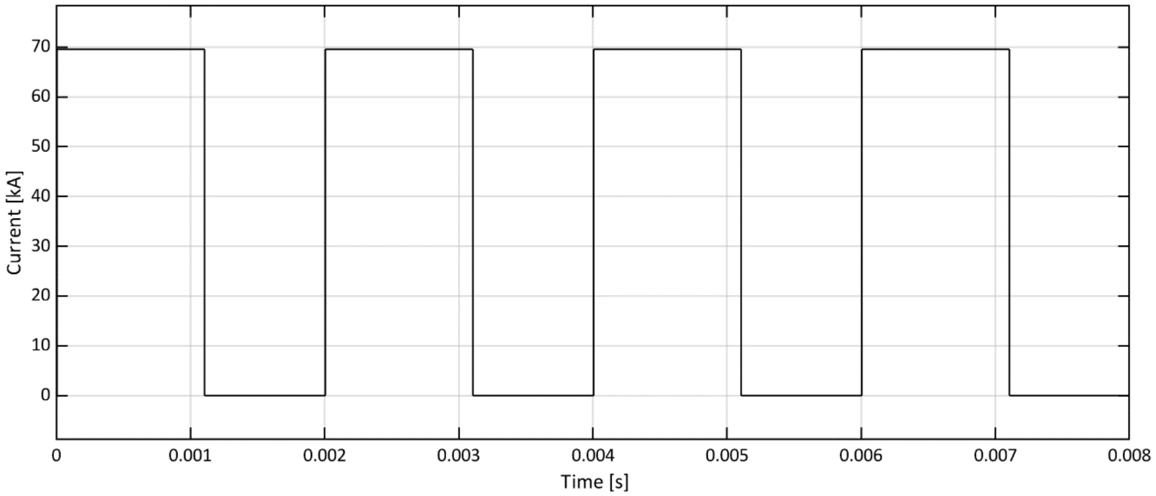

Figure 110 – Total current on MEST equivalent IGCT and diode at considered operating condition for thermal analyses, for f_{SW}=500 Hz.

Table 16 – Conducting and switching losses and junction over-temperature of the MEST IGCTs and diodes for f_{SW}=500 Hz

$f_{sw,limit}$	Component	N_P	P_{CON} [W]	$P_{SW\ ON}$ [W]	$P_{SW\ OFF}$ [W]	P_{TOT} [W]	ΔT [K]
500 Hz	IGCT ABB 5SHY35L4521	60	1133	217	3188	4538	74.9 < 75
	Diode ABB 5SDF20L4520	60	1586	0	2283	3869	54.2 < 90
	IGCT ABB 5SHY42L6500	114	745	249	3532	4526	74.7 < 75
	Diode ABB 5SDF20L4520	114	687	0	1202	1889	26.4 < 90

Table 17 and Table 18 reports the steady state thermal analyses considering f_{SW}=400 Hz and f_{SW}=300 Hz respectively.

Table 17 – Conducting and switching losses and junction over-temperature of the MEST IGCTs and diodes for f_{SW}=400 Hz

$f_{sw,limit}$	Component	N_P	P_{CON} [W]	$P_{SW\ ON}$ [W]	$P_{SW\ OFF}$ [W]	P_{TOT} [W]	ΔT [K]
400 Hz	IGCT ABB 5SHY35L4521	52	1348	201	2943	4492	74.1 < 75
	Diode ABB 5SDF20L4520	52	1932	0	2108	4040	56.5 < 90
	IGCT ABB 5SHY42L6500	96	910	236	3356	4502	74.3 < 75
	Diode ABB 5SDF20L4520	96	852	0	1142	1994	27.9 < 90

Table 18 – Conducting and switching losses and junction over-temperature of the MEST IGCTs and diodes for f_{SW}=300 Hz

$f_{sw,limit}$	Component	N_P	P_{CON} [W]	$P_{SW\ ON}$ [W]	$P_{SW\ OFF}$ [W]	P_{TOT} [W]	ΔT [K]
300 Hz	IGCT ABB 5SHY35L4521	44	1662	178	2608	4448	73.4 < 75
	Diode ABB 5SDF20L4520	44	2452	0	1868	4320	60.5 < 90
	IGCT ABB 5SHY42L6500	77	1184	221	3138	4543	74.9 < 75
	Diode ABB 5SDF20L4520	77	1133	0	1068	2201	30.8 < 90

4.5.1.5 Number of series connected semiconductor devices

For the selection of the number of series connected devices for each equivalent switch the V_{DRM} and the V_{RRM} of the IGCTs and Diode respectively are considered. The number of series connected devices (N_S), considering a safety margin of 1.6 [35], is derived as:

$$N_s \geq \frac{V_{C,max} \cdot 1.6}{V_{DRM/RRM}} \qquad \text{Eq. 80}$$

The derived N_S for each component, considering the case whit SNU and without SNU, are reported in Table 19.

Table 19 – Number of series connected IGCTs and diodes per equivalent switch

Component	N_S w/ SNU	N_S w/o SNU
IGCT ABB 5SHY35L4521	(8000+1000)*1.6/4500=**4**	(10000+1000)*1.6/4500=**4**
IGCT ABB 5SHY42L6500	(8000+1000)*1.6/6500=**3**	(10000+1000)*1.6/6500=**3**
Diode ABB 5SDF20L4520	(8000+1000)*1.6/4500=**4**	(10000+1000)*1.6/4500=**4**

4.5.1.6 Size estimation and comparison

In this section, an estimation of the MEST system size is attempted neglecting the PS, and eventual FDU for the sink coil. As a starting point, the layout of Acceleration Grid Power Supply Conversion System (AGPS-CS) of ITER Neutral Beam Injectors (NBI) has been considered [36]. The AGPS-CS is made by thyristor bridges in 12-pulse configuration connected to the ITER grid, which supply five Neutral Point Clamped (NPC) IGCT-based inverters connected in parallel at the input side.

Each cubicle of AGPS-CS is 1 m × 1.4 m × 2.5 m [width × depth × height]. Half of it (footprint A_{AGPS} = 0.7 m^2) contains 3 modules, each module being an arm of the NPC inverter, made by 4 snubberless IGCTs, 4 freewheeling diodes, 2 clamp diodes and the clamping network as depicted in Figure 111. Therefore, each half-cubicle contains 30 components (N_{AGPS}) in total, excluding the diodes Dcp and Dcl of the clamping network, with a rated power of 6 MVA and a switching frequency equal to 150 Hz.

The second half of the cubicle (footprint A_{AGPS} = 0.7 m^2) contains the capacitor banks, composed by 3 capacitive modules, each made by a pair of capacitor banks of 3 × 800 µF (oil-immersed film capacitors, nominal dc-link voltage equal to 3250 V). Therefore, each half-cubicle has 76.05 kJ of stored energy ($W_{c,AGPS}$).

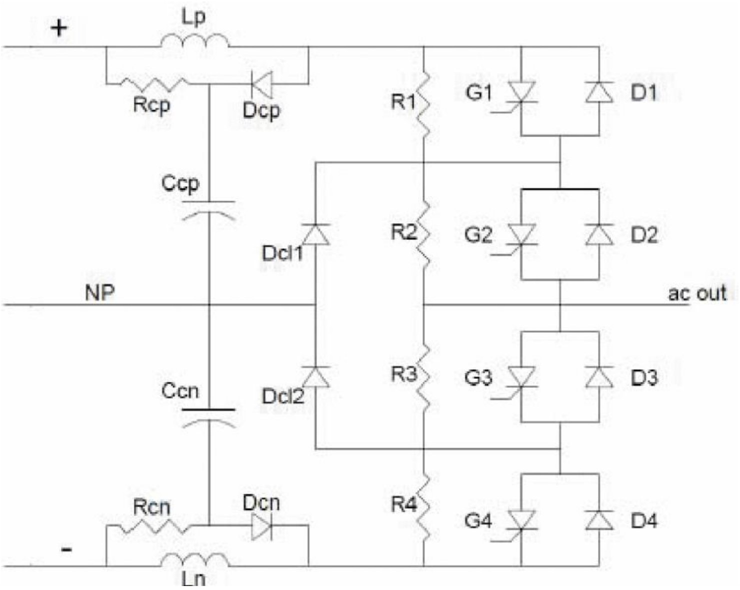

Figure 111 – Scheme of one NPC inverter leg of the AGPS-CS [36]

Scaling the AGPS-CS size proportionally with the number of components of a DEMO MEST system rated for 10 kV and 45 kA we could tentatively estimate the area occupancy of the following elements:

- MEST number of switches (N_{SW}) and area occupancy (A_{SW}) can be estimated as:

$$A_{sw} = \frac{N_{sw}}{N_{AGPS}} \times A_{AGPS} \qquad \text{Eq. 81}$$

Table 20 – Area occupancy of semiconductor switches at different switching frequencies

$f_{sw,limit}$	Component	N_P	N_S	Components number	N_{SW}	A_{SW} [m^2]
500 Hz	IGCT ABB 5SHY35L4521	60	4	4 · 4 · 60 = 960	1920	1920/30*0.7=**44.8**
	Diode ABB 5SDF20L4520	60	4	4 · 4 · 60 = 960		
	IGCT ABB 5SHY42L6500	114	3	4 · 3 · 114 = 1368	3192	3192/30*0.7=**74.5**
	Diode ABB 5SDF20L4520	114	4	4 · 4 · 114 = 1824		
400 Hz	IGCT ABB 5SHY35L4521	52	4	4 · 4 · 52 = 832	1664	1664/30*0.7=**38.8**
	Diode ABB 5SDF20L4520	52	4	4 · 4 · 52 = 832		
	IGCT ABB 5SHY42L6500	96	3	4 · 3 · 96 = 1152	2688	2688/30*0.7=**62.7**
	Diode ABB 5SDF20L4520	96	4	4 · 4 · 96 = 1536		
300 Hz	IGCT ABB 5SHY35L4521	44	4	4 · 4 · 44 = 704	1408	1408/30*0.7=**32.8**
	Diode ABB 5SDF20L4520	44	4	4 · 4 · 44 = 704		
	IGCT ABB 5SHY42L6500	77	3	4 · 3 · 77 = 924	2156	2156/30*0.7=**50.3**
	Diode ABB 5SDF20L4520	77	4	4 · 4 · 77 = 1232		

- Considering $V_{C,max}$ the maximum voltage on the capacitor bank, the maximum energy of the capacitor bank ($W_{c,max}$) and its area occupancy (A_c) can be estimated as:

$$W_{c,max} = 0.5 \times \mathrm{C} \times V_{C,max}^2 \qquad \textit{Eq. 82}$$

$$A_c = \frac{W_{c,max}}{W_{c_{AGPS}}} \times A_{AGPS} \qquad \textit{Eq. 83}$$

Table 21 – Area occupancy of capacitor bank at different switching frequencies

$f_{sw,limit}$	C [mF]	E_C [kJ]	A_C [m^2]
500 Hz	7.2	$0.5 \cdot 0.0072 \cdot 11000^2 = 435.6$	435.6/76.05*0.7=**4.0**
400 Hz	9	$0.5 \cdot 0.009 \cdot 11000^2 = 544.5$	544.5/76.05*0.7=**5.0**
300 Hz	12	$0.5 \cdot 0.012 \cdot 11000^2 = 726$	726/76.05*0.7=**6.7**

- Sink Coil footprint is considered the same of CS3U sector which, according to DEMO baseline 2017 geometry, has a 2.77 m radius of radial thickness of 0.8 m and an axial thickness of 2.99 m:

$$A_{KC} = (2.77 + 0.8)^2 \cdot \pi = 40.0\, m^2 \qquad \textit{Eq. 84}$$

The total MEST system footprint is the following:

$$A_{fp} = (A_{sw} + A_c + \mathrm{A_{KC}}) * 1.2 \qquad \textit{Eq. 85}$$

Including a margin of 20% to include auxiliaries, cooling systems and possible disconnectors and bypasses.

In ITER the ratio between the footprint of the base converter (including dc reactors + disconnectors and bypasses) and the internal area occupancy of Building 32 and Building 33 at ITER site is 1/4.20. This ratio has been derived from the available CAD drawings. Considering the same ratio the internal area occupancy of the MEST system is:

$$A_{MEST} = A_{fp} * 4.2 \qquad \textit{Eq. 86}$$

The results of the MEST area occupancy calculation are reported in Table 22.

Table 22 – MEST system area occupancy

$f_{sw,limit}$	Component (IGCT + Diode)	A_{fp} [m^2]	A_{MEST} [m^2]
500 Hz	IGCT ABB 5SHY35L4521	(44.8 + 4 + 40) · 1.2 = 107	96.5 · 4.2 = **448**
	IGCT ABB 5SHY42L6500	(74.5 + 4 + 40) · 1.2 = 142	132.1 · 4.2 = **597**
400 Hz	IGCT ABB 5SHY35L4521	(38.8 + 5 + 40) · 1.2 = 101	90.5 · 4.2 = **422**
	IGCT ABB 5SHY42L6500	(62.7 + 5 + 40) · 1.2 = 129	119.2 · 4.2 = **543**
300 Hz	IGCT ABB 5SHY35L4521	(32.8 + 6.7 + 40) · 1.2 = 95	85.3 · 4.2 = **401**
	IGCT ABB 5SHY42L6500	(50.3 + 6.7 + 40) · 1.2 = 116	106.2 · 4.2 = **489**

To make a comparison Table 23 [12] reports area occupancy of ITER thyristor base converters, the estimated area occupancy of DEMO thyristor-based converter and DEMO base converter based on AFE technology. For the thyristor-based option, the areas of the converter and of the corresponding portion of RPC&HF system have been tentatively estimated from those of ITER by scaling with the converter power ratings. For the VSC+AFE solution, the footprint has been derived from the size of existing applications based on IGCTs [36], as for the MEST, by scaling with the number of components and the dc-link and input inductor stored energies; then, the building area has been derived multiplying by the same filling factor of ITER; in this case, the area of RPC&HF system should be negligible, if proper control strategies are adopted to minimize the reactive power and the harmonic distortion. While area occupancy for crowbars is included in the case of traditional solution, the presence of crowbars in case of AFEs is under consideration, so the related occupancy is not accounted in the area estimation.

Table 23 – Area occupancy of ITER and DEMO base converters based on thyristors and AFE technology [12]

		BASE CONVERTER					RPC&HF SYSTEM			BASE CONVERTER + RCP&HF SYSTEM
Technology	Plant	Ratings	Footprint indoor [m2]	Internal Area Occupancy [m2]	External Area Occupancy [m2]	Total Area Occupancy [m2]	Internal Area Occupancy [m2]	External Area Occupancy [m2]	Total Area Occupancy [m2]	Area Occupancy [m2]
THYRISTOR	ITER	2.1 kV x 45 kA	98.2	413.0	260.0	673	52	537	589	1262
		2.1 kV x 55 kA	98.2	413.0	260.0	673	64	656	720	1393
		3.15 kV x 55 kA	147.3	619.5	390.9	1010	96	984	1080	2090

	DEMO	8 kV x 45 kA	246	1031	814	1846	199	2045	2244	4090
		10 kV x 45 kA	344	1444	1140	2584	249	2556	2805	5388
AFE	DEMO	8 kV x 45 kA	205	859	803	1662	0	0	0	1662
		10 kV x 45 kA	307	1288	1204	2492	0	0	0	2492

4.5.2 Simulations results

Considering the breakdown scenarios provided by CREATE Consortium, numerical simulations have been set-up to verify the dynamic performance of MEST for the available pulse phases, since presently current and voltage profiles are not available for the entire plasma pulse. The operation of the circuit in Figure 92 has been reproduced using the numerical model reported in section 4.3. The simulation parameters are reported in Table 24. In all the following simulations the circuit of the coil is considered without the SNU, therefore the MEST is rated for the nominal voltage (10 kV).

Table 24 – Simulation parameters of MEST model applied to EU DEMO CS3U

Parameters	Value
$L_{LC} = L_{KC}$	2.07 H
C capacitance	7.2 mF
CS3U rated current	± 45 kA
Max v_C	± 10 kV
Hysteresis band	± 1 kV
Switching frequency limit	500 Hz
Switching pattern	Double-leg

4.5.2.1 Breakdown phase simulation results

Figure 112 shows the CS3U circuit current and voltages of the central inboard scenario provided by CREATE group. The voltage applied to the CS3U sector results from the sum of the main converter voltage and the SNU voltage. As can be seen during the breakdown scenario the SNU applies an almost constant voltage of about 7 kV while the main converter is used to modulate the total voltage applied to the coil terminals. The maximum voltage derivative required in the CS3U scenario during the breakdown is 111 V/ms. The MEST, adopting a proper control, can satisfy this dynamics performance.

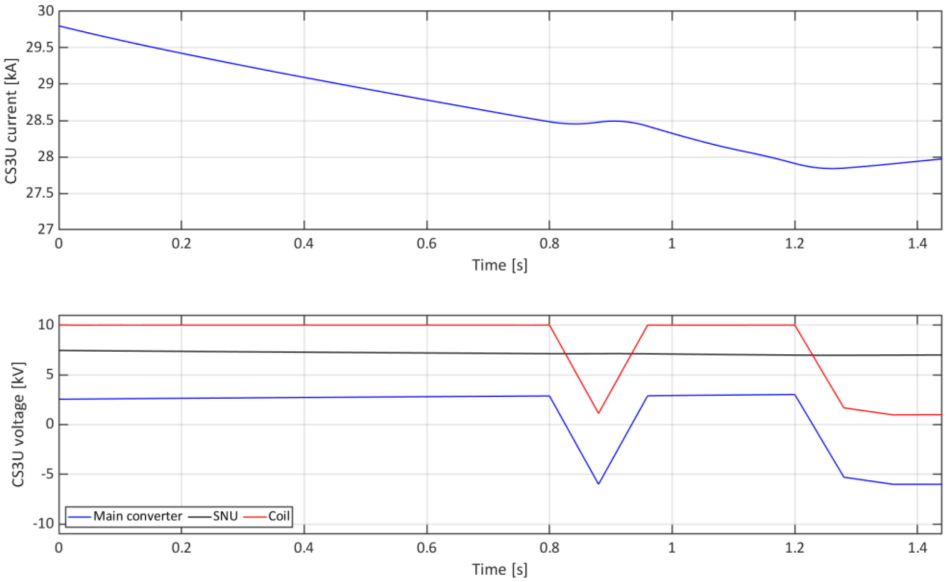

Figure 112 – CS3U circuit current and voltages of central inboard scenario

Figure 113 shows i_{LC}, i_{KC} and v_C during the KC pre-charge, LC-charge and the plasma breakdown (initial part of the pulse), which lasts 1.44 seconds and occupies the right part of the figure.

Figure 113 shows in detail the LC current reference ($i_{LC,ref}$) and actual LC current during the plasma breakdown. As can be seen, the current supplied by the MEST to the CS3U coil follows the reference with a good accuracy. It has to be noted that in this first application study, the magnetic coupling between the CS3U coil with the other coils and the plasma is neglected and this is the motivation behind the difference between the simulated coil voltage and the scenario one.

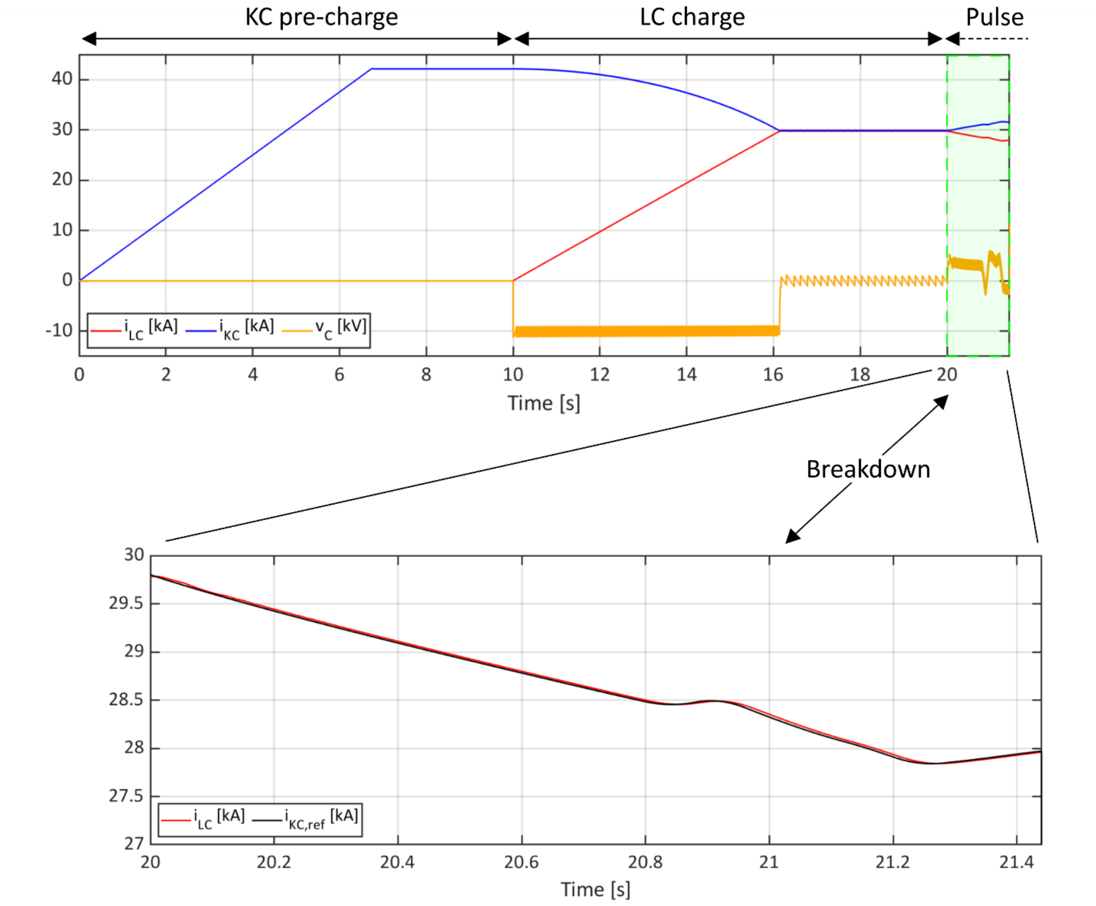

Figure 113 – Waveforms of the main MEST variables during the pulse set-up and the plasma breakdown

During the simulated breakdown scenario the maximum switching frequency is 310 Hz, well below the design limit (Figure 114), and this occurs during the LC charging phase. During the breakdown its maximum is 125 Hz and this is due to the fact that initial currents of tank coil and central solenoid are very close to each other and so the difference is small (see Eq. 34) and also because the maximum LC current is 29.8 kA, below the value of 45 kA considered to design the MEST system.

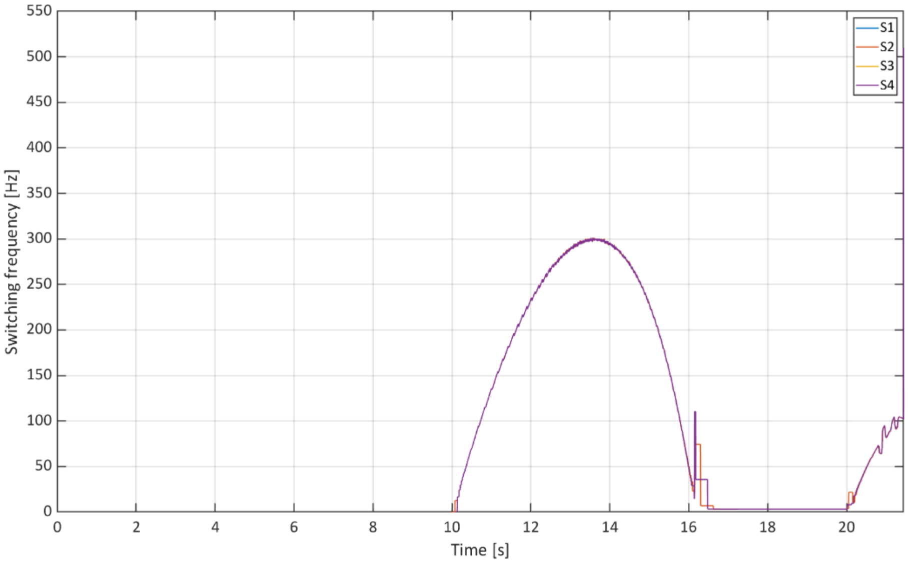

Figure 114 – Switching frequency during the LC charge and the plasma breakdown

The tentative ratings and the numerical simulation of a model of the MEST supplying one DEMO CS coils shows that the dynamic requirements during the breakdown and start-up phase of the pulse could be satisfied with reasonable values of the switching frequency of the MEST switches.

4.5.2.2 Comparison between single-leg and double-leg switching strategy

The same simulation scenario has been carried out with the single-leg strategy and the double-leg strategy. In Figure 115 and Figure 116 it can be seen that the frequency during the simulation with the double-leg strategy leads to a decrease of the maximum switching frequency from 600 Hz to 300 Hz. In Figure 115 can be seen that with the single-leg polarity only S1 and S2 commutates while S3 and S4 commutates only when i_{LC} changes polarity. In Figure 116 the switching frequencies of the four switches are the same during the whole simulation. These results can be explained by the fact that the commutations are distributed between all four switches. In this way, the maximum switching frequency can be halved using the same C capacitance value or the C capacitance can be halved for a given value of maximum switching frequency.

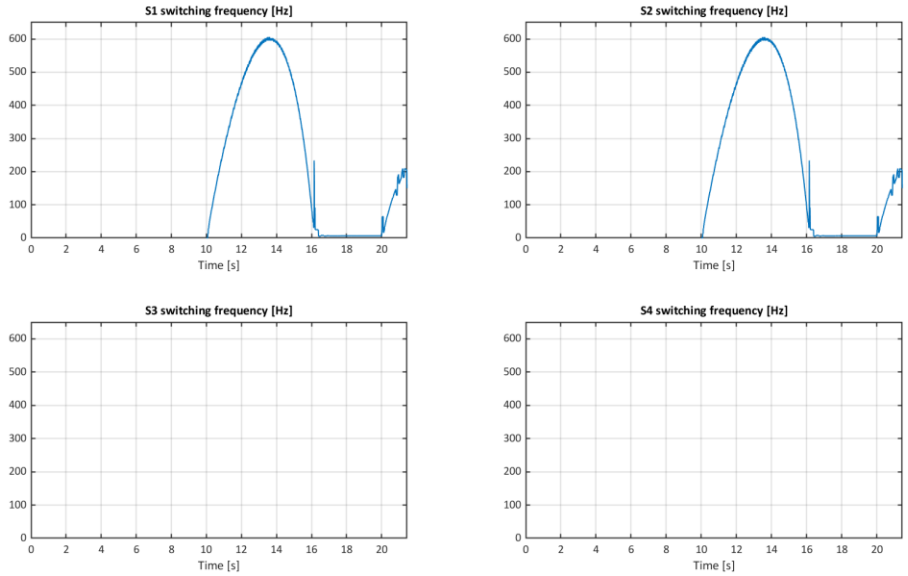

Figure 115 - Switching frequency of S1÷S4 during the pulse simulation with double-leg switching pattern

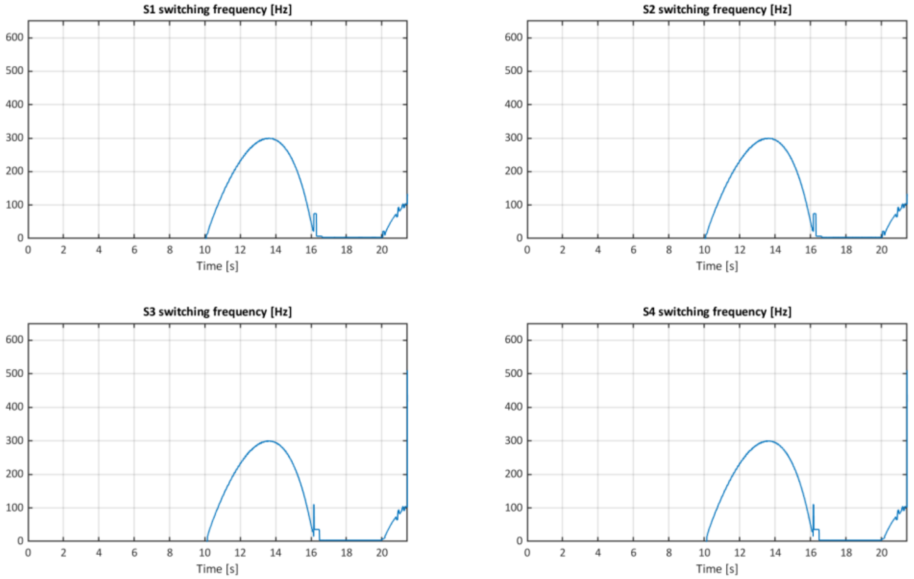

Figure 116 - Switching frequency of S1÷S4 during the pulse simulation with single-leg switching pattern

4.5.2.3 Simulation of patterns with increased dynamic performance

To evaluate with numerical simulations the dynamic performance increase deriving from the use of patterns with increased dynamic performance (see section 4.1.1.3) a simulation with the same numerical model has been set-up.

Figure 117 and Figure 118 show the results of numerical simulations in which $v_{C,ref}$ has a step variation from -10 kV to +10 kV in a model which simulates the DEMO CS3U circuit (i_{LC}≈i_{KC}≈+25 kA in the moment of $v_{C,ref}$ variation, C=7.2 mF). Figure 117 reports v_C variation without the use of the "high derivative" state and it rises to the new $v_{c,ref}$ value in about 6 ms while in Figure 118 the high derivative state [0,1,1,0] is used and v_C reaches the new references in about 2.5 ms.

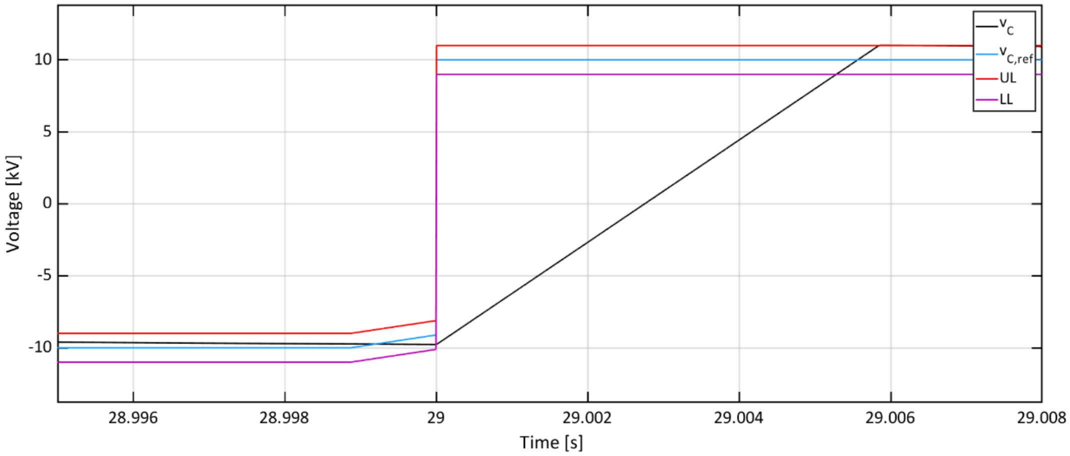

Figure 117 – v_C variation from -10 kV to 10 kV without the use of the "high derivative" state in DEMO CS3U circuit (i_{LC}≈i_{KC}≈+25 kA in the moment of $v_{C,ref}$ variation, C=7.2 mF)

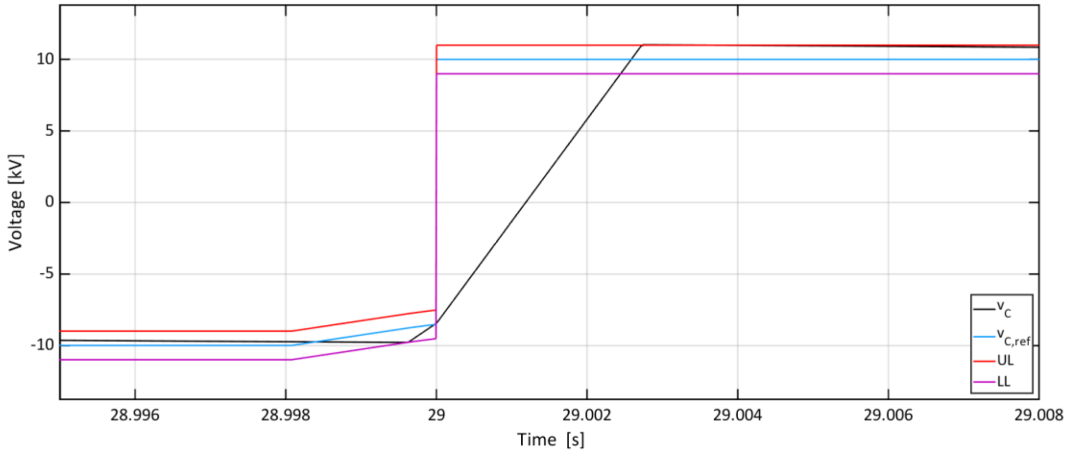

Figure 118 – v_C variation from -10 kV to 10 kV with the use of the "high derivative" state in DEMO CS3U circuit (i_{LC}≈i_{KC}≈+25 kA in the moment of $v_{C,ref}$ variation, C=7.2 mF)

The results show that the dynamic response of the MEST following the load voltage (v_C) can be significantly increased with the use of the high derivative states. As can be seen in Figure 78 the dynamic performance increase is maximum when $i_{LC}=\pm i_{LC,max}$ and it is negligible when i_{LC} is close to 0 A.

4.6 MEST small-scale prototype development and procurement

For a first step to explore the industrial feasibility of such a scheme, the development and procurement of a small-scale prototype has started in the first half of 2022. The main scope of this small-scale prototype is to characterize the MEST system operation.

It is pointed out that even in case of successful results, much additional studies will be required to confirm the viability of this design strategy for EU DEMO. The power level difference between the MEST prototype and the DEMO circuit is actually fairly large. Additionally, the prototype will be connected to copper coils, with no negligible stray resistance; this means that the temporal evolution of the waveform is very different with respect to that expected in EU DEMO. Furthermore, in the application for EU DEMO the energy stored in the LC (which can be CS or PF) and in the KC is orders of magnitude higher than in the capacitor bank, while in the MEST prototype the energy stored in the capacitor bank is not negligible with respect to that stored in the inductors. All this aspects has to be considered to perform a correct interpretation of the results more significant for DEMO.

The inductors that will be used for the load and sink coils have the following characteristics: L=6.16 mH R=28.82 mΩ. These inductors can sustain a current of 6.25 kA with a duty cycle of 0.5 s/600 s (corresponding to a maximum i^2t of 19.5 MA^2s), with natural air-cooling.

The development will be articulated in two phases. The aim of the first phase is the detailed design, manufacturing and test of the simplest circuit configuration with only one switch per branch; this is an important step to characterize the basic MEST operation since it is a new scheme: no similar examples have been found either in the field of fusion or in other fields. The requirements of the MEST module for the first phase are reported in Table 25.

Table 25 – Minimum requirements of the reference MEST circuit for the first phase of the contract

Nominal load voltage	± 2 kV
Maximum load current	± 2 kA
Maximum current in the sink coils / PS	2.8 kA (if L_{LC}=L_{KC})
Nominal PS voltage	≥ 150 V
PS ac input voltage	380 V rms three phase
Max switching frequency	≥ 500 Hz
Max percentage hysteresis voltage band	± 20% of the nominal voltage or lower
Duty cycle	1 / 300 s

The requirements has been chosen considering a power rating that make possible the use of a single switch per branch and the reproduction of reference waveform on the inductors used as LC and KC.

The aim of the second phase of the contract is to select the most suitable circuit topology to increase the power identifying basic module to be connected in series and in parallel; then, to realize and test a prototype with up to two modules to be connected both in series or in parallel.

To approach, even if at low power, a realistic representation of the MEST implementation in DEMO, LC cannot be divided in sectors each supplied by a single cell.

Table 26 – Minimum requirements of the reference MEST circuit for the second phase of the contract

Nominal load voltage	± 4 kV (series connection)
Maximum load current	± 4 kA (parallel connection)
Maximum current in the sink coils / PS	5.6 kA (if LLC=LKC)
Nominal PS voltage	≥ 300 V

As can be seen in Table 26, during the second phase two equal module of the MEST prototype can be series-connected to reach 4 kV / 2 kA or can be parallel-connected to reach 2 kV / 4 kA. Figure 119 shows a simplified scheme of the series and parallel connection of two MEST modules. The reference design for the MEST prototype has been studied for the case of one of these inductors for KC and one for LC but different operating ranges can be explored using series or parallel connections of the inductors.

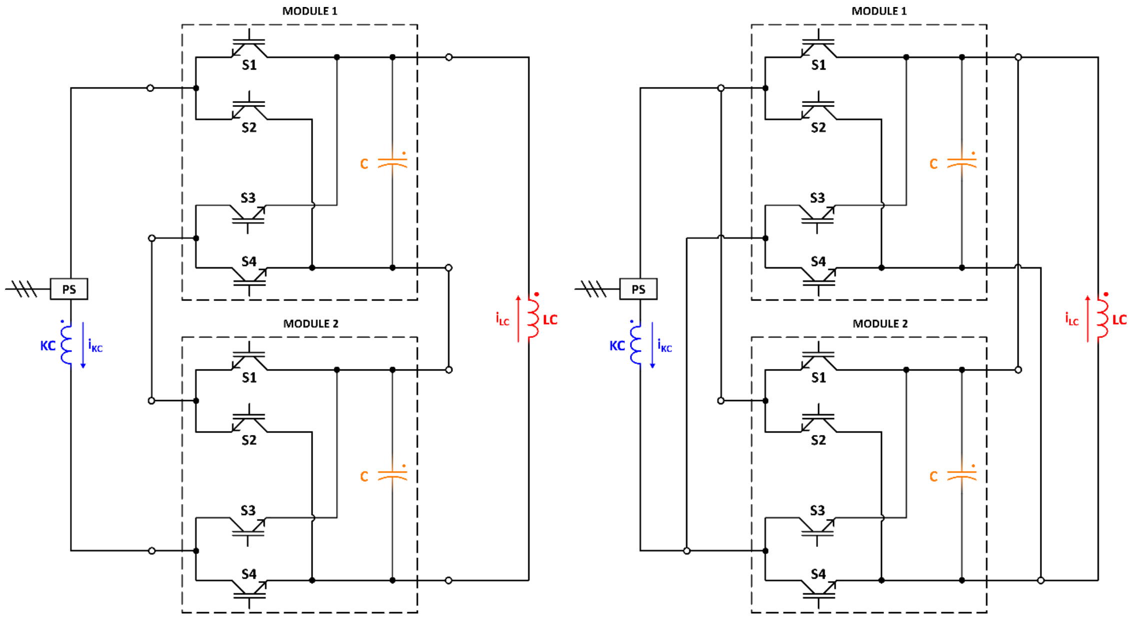

Figure 119 – reference MEST circuit for the second phase of the contract

5 Conclusions

This thesis investigates the electric power handling in existing and future large-sized magnetic fusion experiments. In the first part, two possible reconfigurations of RFX-mod2 poloidal PS system are proposed with the objective to increase the maximum achievable plasma current and flat-top duration, over the initial target performance, essential to explore the new advanced confinement scenarios and fully exploiting and raising the new potential of the RFP configuration. With the proposed solutions the magnetizing winding can operate in the double swing mode increasing the available poloidal magnetic flux variation. The first studied solution is based on magnetic energy storage through an additional inductor and the revision of the poloidal circuit. To analyse this solution a first simplified numerical model of RFX-mod2 poloidal circuit has been developed to define the first design requirements of the additional magnetic energy storage, the needed poloidal circuit modifications and to make a first estimation of the achievable plasma current and flat-top duration. An alternative solution has been proposed and relies on improving the present energy transfer system using electrostatic energy storage and reconfiguring the poloidal circuit. Also in this case, a first numerical model based on a simplified equivalent poloidal circuit has been used to simulate the effect of the main circuit modifications, to support the design of the electrostatic energy storage and the achievable plasma current and flat-top duration.

The first results suggest that with both solutions a plasma current over 2.5 MA could be reached with a flat-top duration of several hundreds of milliseconds. The key driver of the design is remaining within the design limits of the present converters and main transformers, achieving a limited impact on the present PS system and the 400 kV grid. In future, further studies will be addressed to assess the applicability of these applications to RFX-mod2, considering all the operating conditions. The protection systems will need to be adapted to the new machine configuration and it will be fundamental also a revision of the F-coils control to manage the plasma position while the compensation of the magnetomotive force saturates.

In the second part, the MEST, a new scheme based on SMES technology, has been studied to supply SC coils avoiding high power peaks required from the grids and the reactive power demand usually associated with the use of thyristor-based converters. The MEST operating principle has been studied and presented together with a dedicated control strategy which allows obtaining independent control over LC and KC currents. Then, a first application study to the CS circuit of the PILOT, a FFHR based on RFP configuration, has been performed. The system exploits the flux double swing and achieves a continuously pulsed operation, consisting of subsequent pulses with positive and negative plasma currents, repeated with a short dwell time. Firstly, the magnetic coupling between the PILOT CS and the plasma has been analytically evaluated along with the requirements in terms of voltage, currents and magnetizing flux variations during all the pulse phases. Then, the MEST power supply and capacitor bank have been designed. A numerical model comprehensive of the switching section, PS, capacitor bank and control system has been developed to confirm the analytical calculations, the MEST control system operation and the achievable results in terms of active and reactive power exchanged with the grid. The numerical results confirm the decoupling between the grid and CS operated by the MEST system. These results show how the power required to have fast magnetic flux variations is much higher that the power dissipated by the plasma. Achieving this magnetic flux variation without dissipation on the SNUs it’s crucial to increase the system efficiency in the PILOT reactor that can operate with relatively short plasma pulses.

A similar MEST application study is performed for one EU DEMO CS circuit. The purpose of this application study is to confirm that by controlling the capacitor voltage and transferring energy between the KC and LC, the MEST system is capable of supplying the LC voltage and current waveforms required for plasma ignition. The evaluation of the required number of parallel components per equivalent switch and the calculation of area occupancy allowed a comparison of the MEST system space needs with those of competing technologies for powering the main SC coils of EU DEMO. The results show the dynamic requirements during the breakdown and start-up phase of the pulse could be satisfied and that the area occupancy of the MEST system is in the same order of magnitude as the area occupancy of a thyristor-based converter with RPC system and VSC converter with AFE technology.

In the end, the development and procurement of a MEST small-scale prototype, to characterize the MEST system operation, is described.

6 References

[1] "BP energy outlook 2015", https://www.bp.com/content/dam/bp/business-sites/en/global/corporate/pdfs/energy-economics/energy-outlook/bp-energy-outlook-2015.pdf (December 2022)

[2] "BP energy outlook 2020", https://www.bp.com/content/dam/bp/business-sites/en/global/corporate/pdfs/energy-economics/energy-outlook/bp-energy-outlook-2020.pdf (December 2022)

[3] IPCC Global Warming of 1.5°C Special Report, https://www.ipcc.ch/sr15/download/ (December 2022)

[4] Ongena, J., Koch, R., Wolf, R. et al. *Magnetic-confinement fusion.* Nature Phys ***12**, 398–410 (2016). https://doi.org/10.1038/nphys3745*

[5] J. Wesson and D. Campbell, Tokamaks. International Series of Monogr, OUP Oxford, 2011.

[6] H.A.B. Bodin and A.A. Newton 1980 Nucl. Fusion 20 1255.

[7] L. Marrelli et al 2021 Nucl. Fusion 61 023001

[8] F Gnesotto, P Sonato, W.R Baker, A Doria, F Elio, M Fauri, P Fiorentin, G Marchiori, G Zollino, The plasma system of RFX, Fusion Engineering and Design, Volume 25, Issue 4, 1995.

[9] J. Tao et al.*, "ITER Coil Power Supply and Distribution System,"* 2011 IEEE/NPSS 24th Symposium on Fusion Engineering*, 2011, pp. 1-8, doi: 10.1109/SOFE.2011.6052201.*

[10] Fan, R., Tao, J., Suh, I. et al. Control and Protection Strategy Design of ITER Toroidal Field Coil Power Supply System. J Fusion Energ 38, 236–243 (2019). https://doi.org/10.1007/s10894-019-00214-8

[11] A. D. Mankani et al.*, "The ITER reactive power compensation and harmonic filtering (RPC & HF) system: Stability & performance,"* 2011 IEEE/NPSS 24th Symposium on Fusion Engineering*, 2011, pp. 1-6, doi: 10.1109/SOFE.2011.6052341.*

[12] A. Ferro, F. Lunardon, S. Ciattaglia, E. Gaio, "The reactive power demand in DEMO: Estimations and study of mitigation via a novel design approach for base converters," Fusion Engineering and Design, 2019.

[13] E. Gaio et al., Status and challenges for the concept design development of the EU DEMO Plant Electrical System, Fusion Engineering and Design 177 (2022) 113052.

[14] F. Lunardon, et al., "The MEST, a new magnetic energy storage and transfer system: Application studies to the European DEMO", Fusion Engineering and Design, Volume 157, 2020.

[15] R. Piovan, E. Gaio, F. Lunardon and A. Maistrello, "MEST: a new Magnetic Energy Storage and Transfer system for improving the power handling in fusion experiments," Fusion Engineering and Design, 2019.

[16] S. Peruzzo, M. Agostini, P. Agostinetti, M. Bernardi, P. Bettini, et al., "Design concepts of machine upgrades for the RFX-mod experiment," Fusion Engineering and Design, Volume 123, 2017, Pages 59-62.

[17] A Stella, M Guarnieri, F Bellina, P.P Campostrini, G Chitarin, F Trevisan, P Zaccaria, "The RFX magnet system," Fusion Engineering and Design, Volume 25, Issue 4, 1995, Pages 373-399.

[18] A. Maschio, R. Piovan, I. Benfatto, P. Collarin, A. De Lorenzi, L. Fellin, et al., "The power supply system of RFX", Fusion Engineering and Design, Volume 25, Issue 4, 1995, Pages 401–424.

[19] Valisa, M., Bolzonella, T., Buratti, P., Carraro, L., Cavazzana, R., Dal Bello, S., ... & Zuin, M. (2008). High current regimes in RFX-mod. Plasma Physics and Controlled Fusion, 50(12), 124031.

[20] Marrelli, L., Martin, P., Puiatti, M. E., Sarff, J. S., Chapman, B. E., Drake, J. R., ... & Masamune, S. (2021). The reversed field pinch. Nuclear Fusion, 61(2), 023001.

[21] F. Lunardon, A. Maistrello, E. Gaio, R. Piovan, "Feasibility study of RFX-mod2 performance improvement by additional magnetic energy storage", Fusion Engineering and Design, Volume 173, 2021.

[22] L. Zanotto, C. Finotti and V. Toigo, "Overview of the toroidal power supply system of RFX-mod after ten years of operation," 2015 IEEE 15th International Conference on Environment and Electrical Engineering (EEEIC), 2015, pp. 926-931.

[23] L. Novello, A. Zamengo, A. Ferro, L. Zanotto, M. Barp, R. Cavazzana, C. Finotti, M. Recchia, E. Gaio, "Enhancement of the power supply systems in RFX-mod towards 2MA plasma current", Fusion Engineering and Design, Volume 86, Issues 6–8, 2011, Pages 1393-1397.

[24] A. Ferro, J. J. Framarin, L. Novello, A. Zamengo, L. Zanotto and E. Gaio, "Review of the RFX-Mod AC/DC Conversion System and Possible Improvements for New Plasma Scenarios," in IEEE Transactions on Plasma Science, vol. 42, no. 3, pp. 645-650, March 2014.

[25] R. Piovan, et al., "A continuously pulsed Reversed Field Pinch core for an ohmically heated hybrid reactor", Fusion Engineering and Design, Volume 136, 2018.

[26] Valisa, M., Bolzonella, T., Buratti, P., Carraro, L., Cavazzana, R., Dal Bello, S., ... & Zuin, M. (2008). High current regimes in RFX-mod. Plasma Physics and Controlled Fusion, 50(12), 124031.

[27] P. Piovesan et al 2014 Nucl. Fusion 54 064006

[28] R. Piovan et al.*, "Status and Perspectives of a Reversed Field Pinch as a Pilot Neutron Source," in* IEEE Transactions on Plasma Science*, vol. 48, no. 6, pp. 1708-1714, June 2020, doi: 10.1109/TPS.2019.2957888.*

[29] R. Piovan et al.*, "Double Poloidal Field System With Superconducting and Conventional Copper Coils for Induced High Loop Voltage: A New Concept and a Feasibility Study for an RFP FFHR," in* IEEE Transactions on Plasma Science*, vol. 50, no. 11, pp. 4311-4317, Nov. 2022, doi: 10.1109/TPS.2022.3179291.*

[30] P. Collarin, A. De Lorenzi and R. Piovan, "Influence of RFX engineering parameters on plasma behaviour," 15th IEEE/NPSS Symposium. Fusion Engineering*, 1993, pp. 657-660 vol.2, doi: 10.1109/FUSION.1993.518415.*

[31] "ABB Asymettric IGCT 5SHY 42L6500", https://search.abb.com/library/Download.aspx?DocumentID=5SYA1245

[32] "ABB Fast recovery diode 5SDF20L4520", https://search.abb.com/library/Download.aspx?DocumentID=5SYA1184

[33] ABB Application note "Applying IGCTs", https://search.abb.com/library/Download.aspx?DocumentID=5SYA2032

[34] Z. Song et al.*, "Prototype Design and Test of ITER PF Converter Unit," in* IEEE Transactions on Plasma Science*, vol. 44, no. 9, pp. 1677-1683, Sept. 2016, doi: 10.1109/TPS.2016.2571322.*

[35] ABB Application note "Voltage ratings of high power semiconductors", https://search.abb.com/library/Download.aspx?DocumentID=5SYA2051

[36] Zanotto L. et al., "Final design of the acceleration grid power supply conversion system of the MITICA Neutral Beam Injector", Fusion Engineering and Design 123, April 2017.

Annex 1

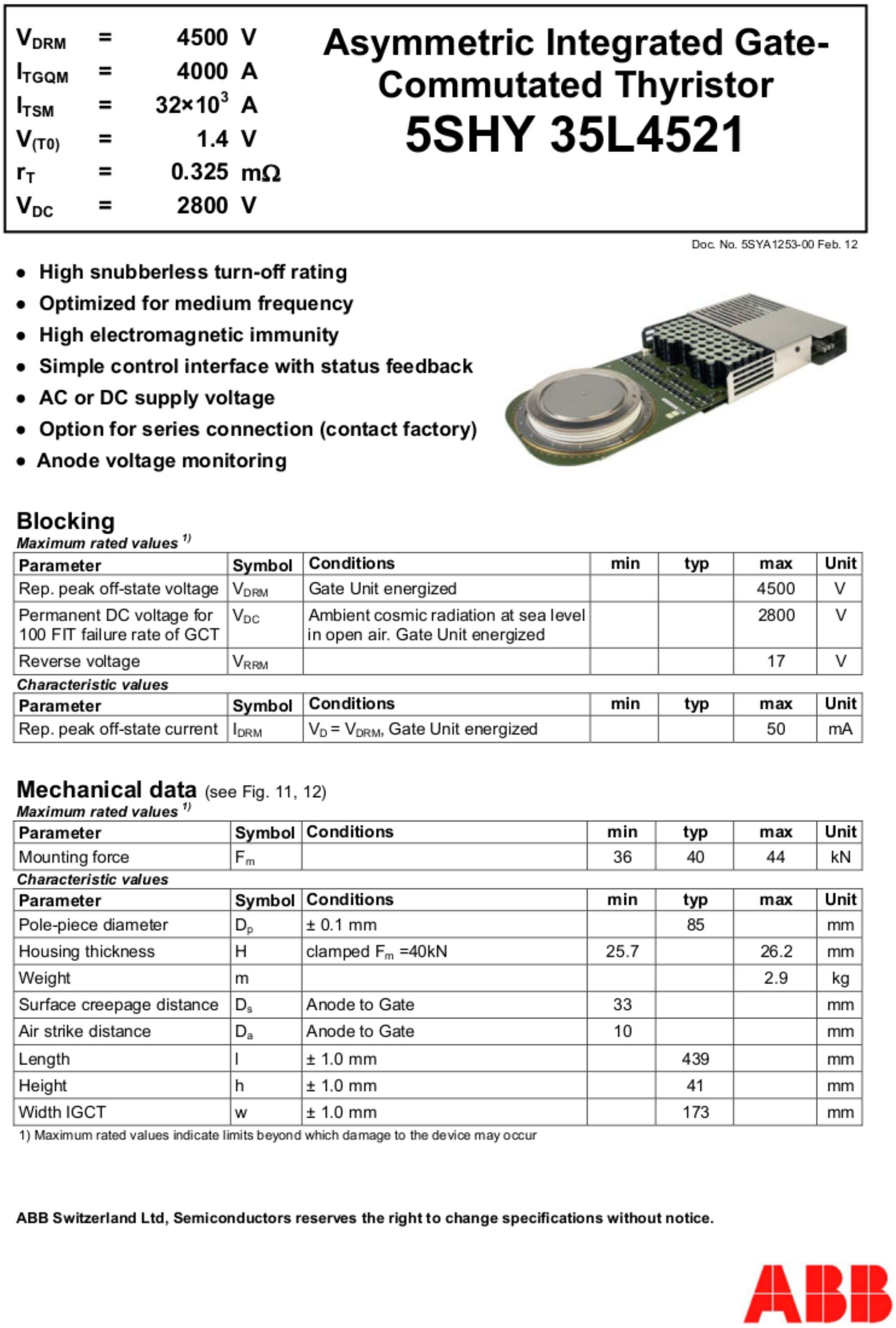

V_{DRM} = 4500 V
I_{TGQM} = 4000 A
I_{TSM} = 32×10^3 A
$V_{(T0)}$ = 1.4 V
r_T = 0.325 mΩ
V_{DC} = 2800 V

Asymmetric Integrated Gate-Commutated Thyristor

5SHY 35L4521

Doc. No. 5SYA1253-00 Feb. 12

- **High snubberless turn-off rating**
- **Optimized for medium frequency**
- **High electromagnetic immunity**
- **Simple control interface with status feedback**
- **AC or DC supply voltage**
- **Option for series connection (contact factory)**
- **Anode voltage monitoring**

Blocking

Maximum rated values [1)]

Parameter	Symbol	Conditions	min	typ	max	Unit
Rep. peak off-state voltage	V_{DRM}	Gate Unit energized			4500	V
Permanent DC voltage for 100 FIT failure rate of GCT	V_{DC}	Ambient cosmic radiation at sea level in open air. Gate Unit energized			2800	V
Reverse voltage	V_{RRM}				17	V

Characteristic values

Parameter	Symbol	Conditions	min	typ	max	Unit
Rep. peak off-state current	I_{DRM}	$V_D = V_{DRM}$, Gate Unit energized			50	mA

Mechanical data (see Fig. 11, 12)

Maximum rated values [1)]

Parameter	Symbol	Conditions	min	typ	max	Unit
Mounting force	F_m		36	40	44	kN

Characteristic values

Parameter	Symbol	Conditions	min	typ	max	Unit
Pole-piece diameter	D_p	± 0.1 mm		85		mm
Housing thickness	H	clamped F_m =40kN	25.7		26.2	mm
Weight	m				2.9	kg
Surface creepage distance	D_s	Anode to Gate	33			mm
Air strike distance	D_a	Anode to Gate	10			mm
Length	l	± 1.0 mm		439		mm
Height	h	± 1.0 mm		41		mm
Width IGCT	w	± 1.0 mm		173		mm

1) Maximum rated values indicate limits beyond which damage to the device may occur

ABB Switzerland Ltd, Semiconductors reserves the right to change specifications without notice.

GCT Data

On-state (see Fig. 3, 4, 5, 6, 14, 15)

Maximum rated values [1)]

Parameter	Symbol	Conditions	min	typ	max	Unit
Max. average on-state current	$I_{T(AV)M}$	Half sine wave, T_C = 85 °C, Double side cooled			1700	A
Max. RMS on-state current	$I_{T(RMS)}$				2670	A
Max. peak non-repetitive surge on-state current	I_{TSM}	t_p = 3 ms, T_j = 125 °C, sine wave after surge: $V_D = V_R$ = 0 V			50×10^3	A
Limiting load integral	I^2t				3.75×10^6	A^2s
Max. peak non-repetitive surge on-state current	I_{TSM}	t_p = 10 ms, T_j = 125 °C, sine wave after surge: $V_D = V_R$ = 0 V			32×10^3	A
Limiting load integral	I^2t				5.12×10^6	A^2s
Max. peak non-repetitive surge on-state current	I_{TSM}	t_p = 30 ms, T_j = 125 °C, sine wave after surge: $V_D = V_R$ = 0 V			20.5×10^3	A
Limiting load integral	I^2t				6.3×10^6	A^2s
Stray inductance between GCT and antiparallel diode	L_D	Only relevant for applications with antiparallel diode to the IGCT			300	nH
Critical rate of rise of on-state current	$di_T/dt_{(cr)}$	For higher di_T/dt and current lower than 100 A an external retrigger puls is required.			200	A/µs

Characteristic values

Parameter	Symbol	Conditions	min	typ	max	Unit
On-state voltage	V_T	I_T = 4000 A, T_j = 125 °C		2.35	2.7	V
Threshold voltage	$V_{(T0)}$	T_j = 125 °C I_T = 1000...4000 A			1.4	V
Slope resistance	r_T				0.325	mΩ

Turn-on switching (see Fig. 14, 15)

Maximum rated values $^{1)}$

Parameter	Symbol	Conditions	min	typ	max	Unit
Critical rate of rise of on-state current	$di_T/dt_{(cr)}$	f = 0..500 Hz, T_j = 125 °C, I_T = 4000 A V_D = 2800 V, $I_{TM} \leq$ 4800 A			1000	A/µs

Characteristic values

Parameter	Symbol	Conditions	min	typ	max	Unit
Turn-on delay time	$t_{d(on)}$	V_D = 2800 V, T_j = 125 °C, I_T = 4000 A, di/dt = V_D / L_i L_i = 5 µH C_{CL} = 10 µF, L_{CL} = 0.3 µH D_{FWD} = D_{CL} = 5SDF 10H4503			3.5	µs
Turn-on delay time status feedback	$t_{d(on)\ SF}$				7	µs
Rise time	t_r				1	µs
Turn-on energy per pulse	E_{on}				1.5	J

Turn-off switching (see Fig. 7, 8, 10, 14, 15)

Maximum rated values $^{1)}$

Parameter	Symbol	Conditions	min	typ	max	Unit
Max. controllable turn-off current	I_{TGQM}	$V_{DM} \leq V_{DRM}$, T_j = 125°C, V_D = 2800 V, R_S = 0.65 Ω, C_{CL} = 10 µF, $L_{CL} \leq$ 0.3 µH D_{FWD} = D_{CL} = 5SDF 10H4503			4000	A

Characteristic values

Parameter	Symbol	Conditions	min	typ	max	Unit
Turn-off delay time	$t_{d(off)}$	V_D = 2800 V, T_j = 125 °C, $V_{DM} \leq V_{DRM}$, R_S = 0.65 Ω I_{TGQ} = 4000 A, L_i = 5 µH C_{CL} = 10 µF, L_{CL} = 0.3 µH D_{FWD} = D_{CL} = 5SDF 10H4503			7	µs
Turn-off delay time status feedback	$t_{d(off)\ SF}$				7	µs
Turn-off energy per pulse	E_{off}			19.5	22	J

Gate Unit Data

Power supply (see Fig. 2, 9, 10, 12, 13)

Maximum rated values 1)

Parameter	Symbol	Conditions	min	typ	max	Unit
Gate Unit voltage (Connector X1)	$V_{Gin\ RMS}$	AC square wave amplitude (15 kHz - 100kHz) or DC voltage. No galvanic isolation to power circuit.	28		40	V
Min. current needed to power up the Gate Unit	$I_{Gin\ Min}$	Rectified average current see application note 5SYA 2031	2			A
Gate Unit power consumption	$P_{Gin\ Max}$				130	W

Characteristic values

Parameter	Symbol	Conditions	min	typ	max	Unit
Internal current limitation	$I_{Gin\ Max}$	Rectified average current limited by the Gate Unit			8	A

Optical control input/output 2)

Maximum rated values 1)

Parameter	Symbol	Conditions	min	typ	max	Unit
Min. on-time	t_{on}		40			μs
Min. off-time	t_{off}		40			μs

Characteristic values

Parameter	Symbol	Conditions	min	typ	max	Unit
Optical input power	$P_{on\ CS}$	CS: Command signal SF: Status feedback Valid for 1mm plastic optical fiber (POF)	-15		-1	dBm
Optical noise power	$P_{off\ CS}$				-45	dBm
Optical output power	$P_{on\ SF}$		-19		-1	dBm
Optical noise power	$P_{off\ SF}$				-50	dBm
Optical output power	$P_{on\ SFA}$		-19		-1	dBm
Optical noise power	$P_{off\ SFA}$				-50	dBm
Pulse width threshold	t_{GLITCH}	Max. pulse width without response			400	ns
External retrigger pulse width	t_{retrig}		700		1100	ns

2) Do not disconnect or connect fiber optic cables while light is on.

Connectors 2) (see Fig. 11, 12, 13)

Parameter	Symbol	Description
Gate Unit power connector	X1	AMP: MTA-156, Part Number 641210-5 3)
Anode voltage monitor connector	J900	AMP: MTA-156, Part Number 3-641210-2 3)
LWL receiver for command signal	CS	Avago, Type HFBR-2521Z 4)
LWL transmitter for status feedback	SF	Avago, Type HFBR-1528Z 4)
LWL transmitter for anode feedback	SFA	Avago, Type HFBR-1528Z 4)

2) Do not disconnect or connect fiber optic cables while light is on.

3) AMP, www.amp.com

4) Avago Technologies, www.avagotech.com

Anode Voltage Monitoring

Maximum rated values [1)]

Parameter	Symbol	Conditions	min	typ	max	Unit
Voltage Feedback low level	$V_{th,\ low}$	R_a = 62 kΩ ± 5% [5)]	910		1100	V
Voltage Feedback high level	$V_{th,\ high}$		4260		5000	V

5) For other voltage levels please see application note 5SYA 2031 or contact factory

Visual feedback (see Fig. 13)

Parameter	Symbol	Description	Color
Gate OFF	LED1	"Light" when GCT is off	(green)
Gate ON	LED2	"Light" when gate-current is flowing	(yellow)
Fault	LED3	"Light" when not ready / Failure	(red)
Power supply voltage OK	LED4	"Light" when power supply is within specified range	(green)

Thermal

Maximum rated values $^{1)}$

Parameter	**Symbol**	**Conditions**	**min**	**typ**	**max**	**Unit**
Junction operating temperature	T_{vj}		0		125	°C
Storage temperature range	T_{stg}		0		60	°C
Ambient operational temperature	T_a		0		50	°C

Characteristic values

Parameter	**Symbol**	**Conditions**	**min**	**typ**	**max**	**Unit**
Thermal resistance junction-to-case of GCT	$R_{th(j-c)}$	Double side cooled			8.5	K/kW
Thermal resistance case-to-heatsink of GCT	$R_{th(c-h)}$	Double side cooled			3	K/kW

Analytical function for transient thermal impedance:

$$Z_{th(j-c)}(t) = \sum_{i=1}^{n} R_i(1 - e^{-t/\tau_i})$$

i	1	2	3	4
R_i(K/kW)	5.562	1.527	0.868	0.545
τ_i(s)	0.5119	0.0896	0.0091	0.0024

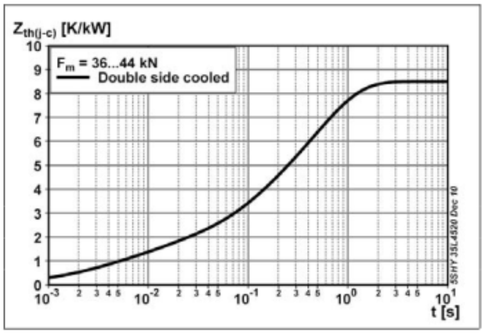

Fig. 1 Transient thermal impedance (junction-to-case) vs. time (max. values)

Max. Turn-off current for Lifetime operation

- calculated lifetime of on-board capacitors 20 years
- with slightly forced air cooling (air velocity > 0.5 m/s)
- strong air cooling allows for increased ambient temperature

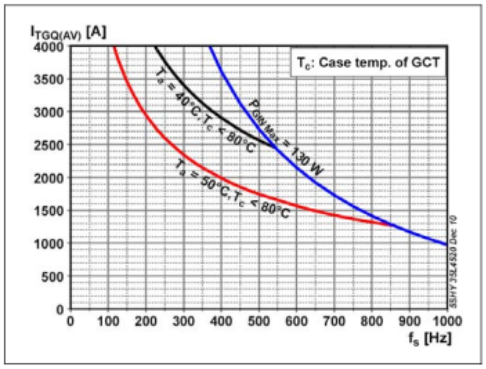

Fig. 2 Max. turn-off current vs. frequency for lifetime operation

Max. on-state characteristic model:

$$V_{T25} = A_{T_{vj}} + B_{T_{vj}} \cdot I_T + C_{T_{vj}} \cdot \ln(I_T + 1) + D_{T_{vj}} \cdot \sqrt{I_T}$$

Valid for i_T = 300 – 30000 A

A_{25}	B_{25}	C_{25}	D_{25}
622.7×10^{-3}	163.4×10^{-6}	141.1×10^{-3}	0.0

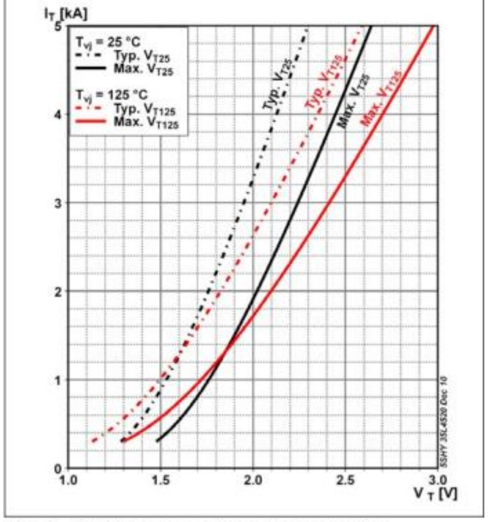

Fig. 3 GCT on-state voltage characteristics

Max. on-state characteristic model:

$$V_{T125} = A_{T_{vj}} + B_{T_{vj}} \cdot I_T + C_{T_{vj}} \cdot \ln(I_T + 1) + D_{T_{vj}} \cdot \sqrt{I_T}$$

Valid for i_T = 300 – 30000 A

A_{125}	B_{125}	C_{125}	D_{125}
-16.0×10^{-3}	226.6×10^{-6}	218.4×10^{-3}	0.0

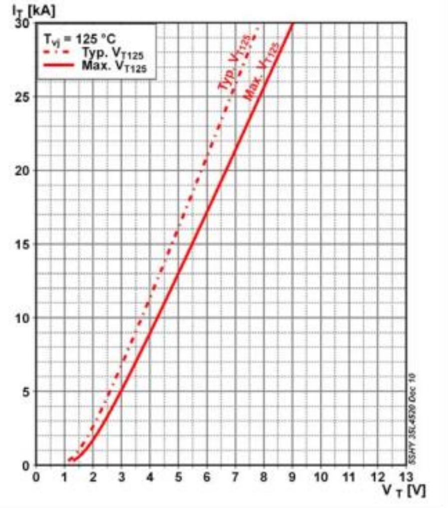

Fig. 4 GCT on-state voltage characteristics

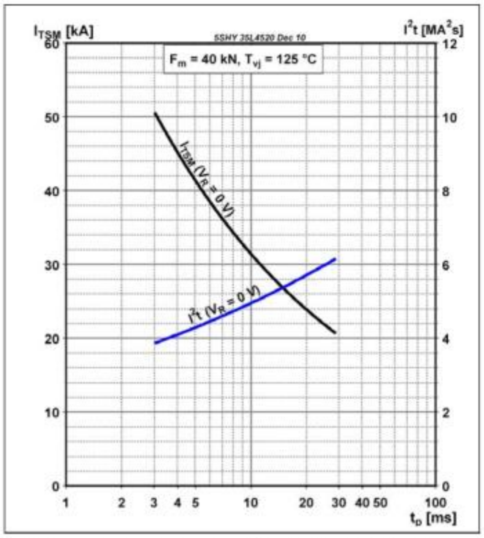

Fig. 5 Surge on-state current vs. pulse length, half-sine wave, no reapplied voltage

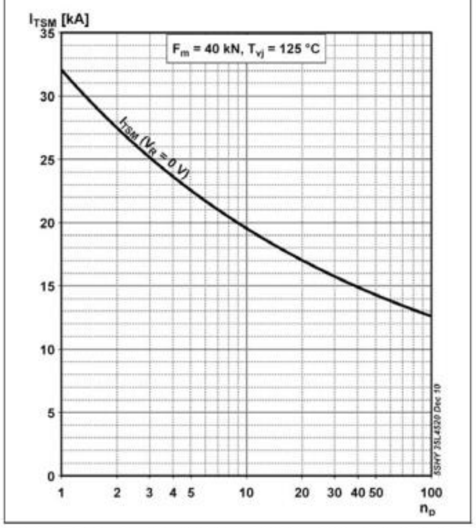

Fig. 6 Surge on-state current vs. number of pulses, half-sine wave, 10 ms, 50Hz, no reapplied voltage

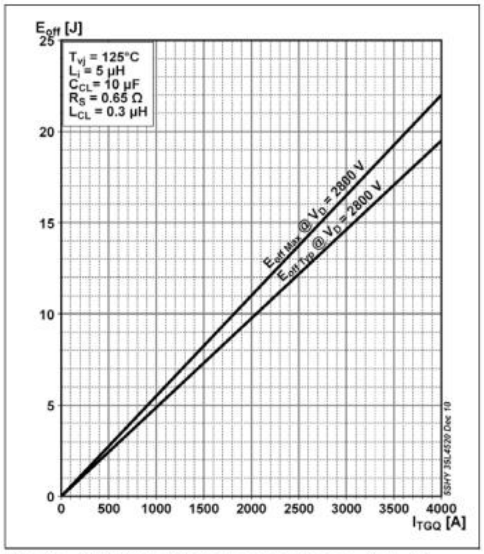

Fig. 7 GCT turn-off energy per pulse vs. turn-off current

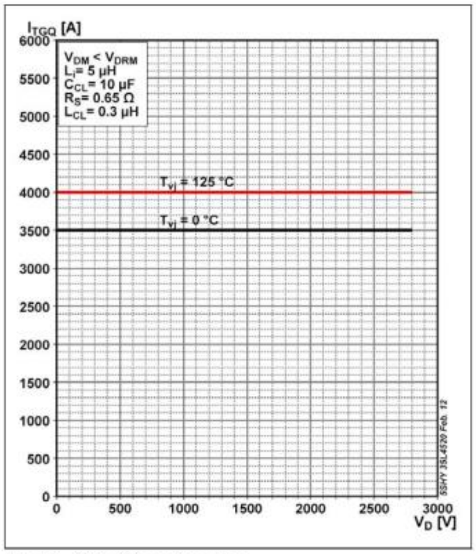

Fig. 8 Safe Operating Area

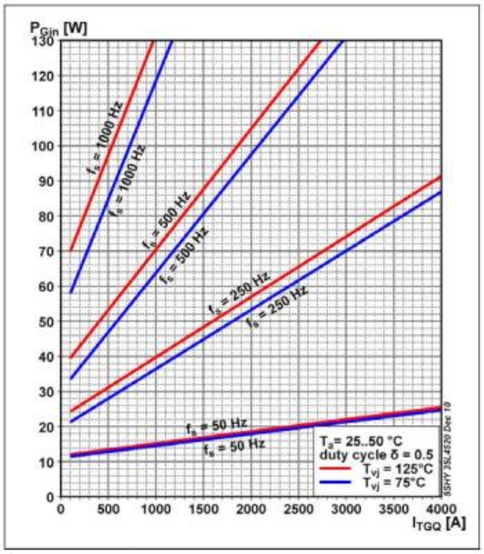

Fig. 9 Max. Gate Unit input power in chopper mode

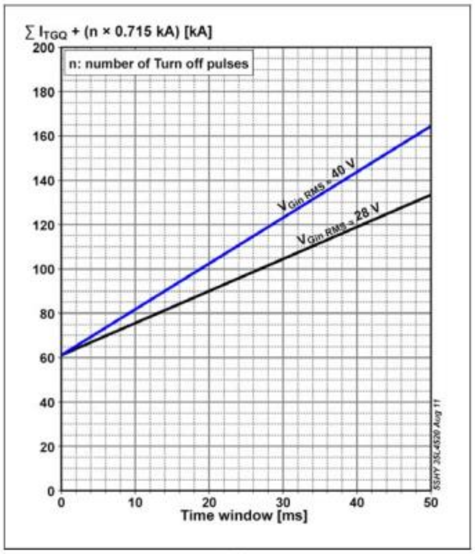

Fig. 10 Burst capability of Gate Unit

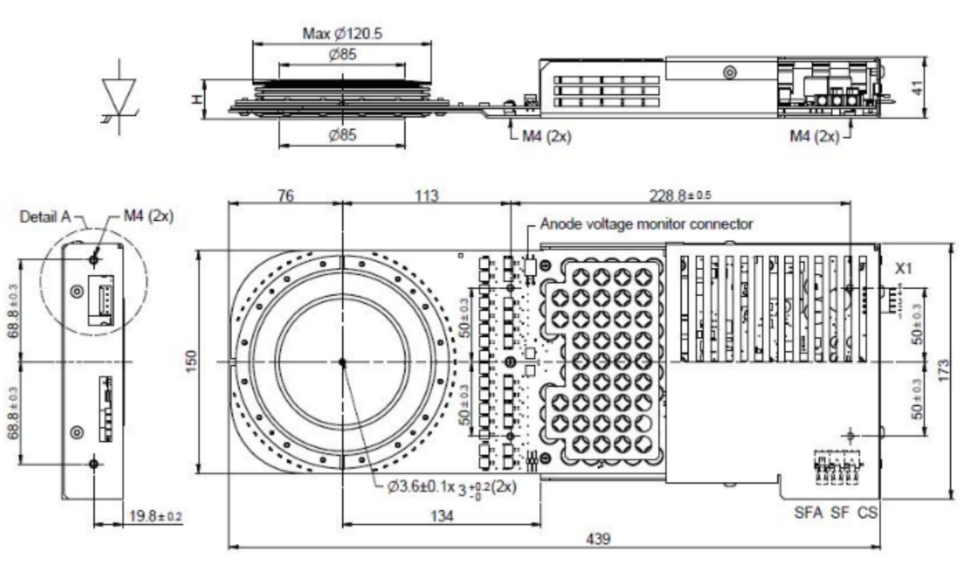

Fig. 11 Outline drawing; all dimensions are in millimeters and represent nominal values unless stated otherwise

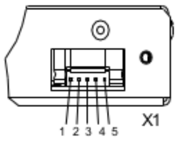

1) V_{Gin} (AC or DC+)
2) V_{Gin} (AC or DC+)
3) Cathode
4) V_{Gin} (AC or DC-)
5) V_{Gin} (AC or DC-)

Fig. 12 Detail A: pin out of supply connector X1

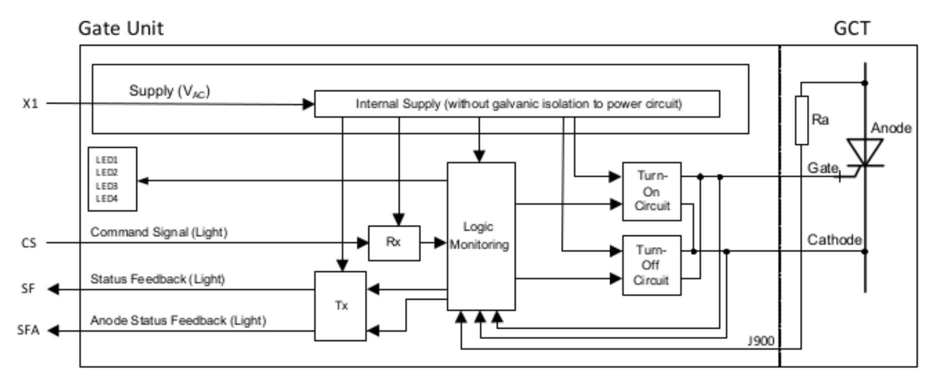

Fig. 13 Block diagram

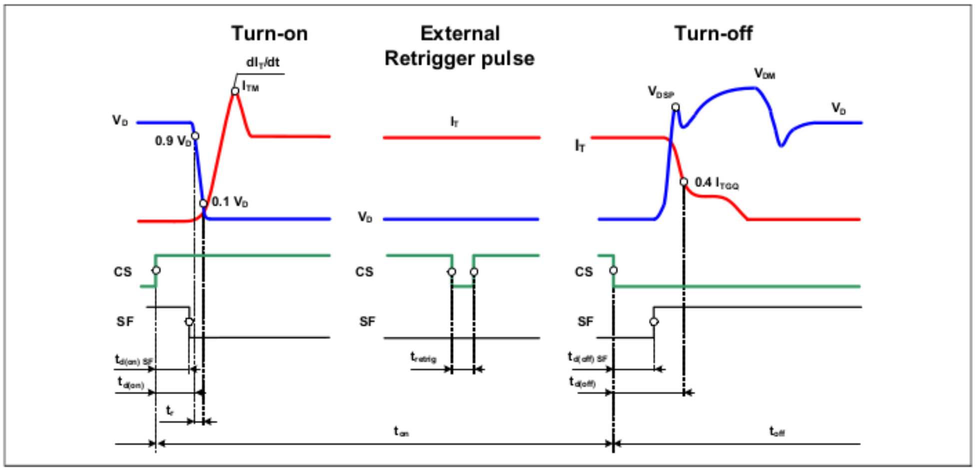

Fig. 14 General current and voltage waveforms with IGCT - specific symbols

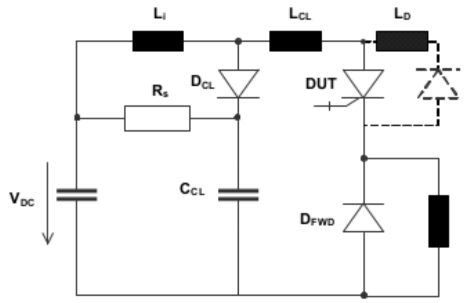

Fig. 15 Test circuit

Related documents:

5SYA 2031	Applying IGCT Gate Units
5SYA 2032	Applying IGCTs
5SYA 2036	Recommendations regarding mechanical clamping of Press Pack High Power Semiconductors
5SYA 2046	Failure rates of IGCTs due to cosmic rays
5SYA 2048	Field measurements on High Power Press Pack Semiconductors
5SYA 2051	Voltage ratings of high power semiconductors
5SZK 9107	Specification of enviromental class for pressure contact IGCTs, OPERATION available on request, please contact factory
5SZK 9109	Specification of enviromental class for pressure contact IGCTs, STORAGE available on request, please contact factory
5SZK 9110	Specification of enviromental class for pressure contact IGCTs, TRANSPORTATION available on request, please contact factory

Please refer to http://www.abb.com/semiconductors for current version of documents.

ABB Switzerland Ltd
Semiconductors
Fabrikstrasse 3
CH-5600 Lenzburg, Switzerland

Telephone +41 (0)58 586 1419
Fax +41 (0)58 586 1306
Email abbsem@ch.abb.com
Internet www.abb.com/semiconductors